INTEGRATING GRAIN-SCALE AND FAULT-SCALE GEOMECHANICAL MODELS: A MULTI-SCALE STUDY OF FAULT TRIGGERING

A Dissertation

by

RYAN MATTHEW PAYNE

Submitted to the Office of Graduate and Professional Studies of
Texas A&M University
in partial fulfillment of the requirements for the degree of

DOCTOR OF PHILOSOPHY

Chair of Committee,	David Sparks
Co-Chair of Committee,	Benchun Duan
Committee Members,	Richard Gibson
	Zenon Medina-Cetina
Head of Department,	Michael Pope

December 2017

Major Subject: Geophysics

ABSTRACT

Observations have shown that minor changes in the stress state of faults can be significant enough to induce seismic slip. One source of these minor stress changes is from naturally occurring earthquakes located several fault dimensions away from the triggered fault. The seismic waves generated can induce a cascade of other earthquakes as they pass through the crust, however, the details of this process are not understood. The current study uses a dynamic rupture model – a powerful tool for simulating physically-realistic earthquakes – to determine the stresses produced in the earth next to active faults. These simulations are paired with separate simulations of the granular material inside a fault zone where that granular material is subjected to dynamic stress perturbations similar to what is produced by the dynamic rupture simulations.

Together, these two methods provide a unique window into earthquake triggering. For the first time we observe off-fault values, particularly stress and strain rate changes, produced by a passing fault rupture. The dynamic stress perturbations consist of sudden stress peaks coincident with rupture passage, often several MPa worth of change, far above what has been seen to cause triggering. When a similar perturbation was put into the granular code as a sudden pulse in the normal stress, several different behaviors were observed depending on the perturbation amplitude and the distance from failure. The work presented in this dissertation should be seen as the groundwork for a future linking of the dynamic rupture and granular codes into a single model that uses the output of one code as the inputs for another.

CONTRIBUTORS AND FUNDING SOURCES

This work was supervised by a dissertation committee consisting of Professors David Sparks and Benchun Duan, as co-advisors, and Professor Richard Gibson of the Geology and Geophysics Department and Professor Zenon Medina-Cetina of the Department of Civil Engineering.

All work for the dissertation was completed by the student, under the advisement of Dr. Benchun Duan and Dr. David Sparks of the Department of Geology & Geophysics. Numerical models created by Dr. Duan and Dr. Sparks were used in the research for sections 3 and 4, and 5, respectively.

Graduate study was supported by a Chevron Fellowship through the Berg-Hughes Center. This work was made possible in part by the National Science Foundation under Grant Numbers EAR-1524743, EAR-1254573, EAR-1049834 and EAR-1114235.

TABLE OF CONTENTS

Page

LIST OF FIGURES

Page

LIST OF TABLES

Page

1. INTRODUCTION

1.1 Background

It is believed that faults in the Earth's crust are perpetually in a state of near-failure. This precarious position means that slight changes or perturbations in stress have the potential to push critically stressed faults over the brink and induce seismic slip. Such seismic triggering can be caused by anthropogenic activities, such as fluid injection or extraction (Segall, 1989; Shapiro and Dinske, 2009), as well as by natural earthquakes (Hill et al., 1993; Freed, 2005; Prejean et al., 2004). Scientists have seen this happen, but the exact mechanisms which lead to slip are still poorly understood. This is due, in part, to the fact that geologically active faults are complex structures, marked by an interaction of many different physical processes at varying time and length scales. Much progress has been made by utilizing advanced computer models as an effective way of studying the different components of such systems (Bizzarri, 2010; Griffa et al., 2013). However, little has been done to link these various models together into a more complete and realistic simulation of the natural world. The current study aims to do this by examining the relationship between two specific facets of faults: 1) the radiated energy generated by an earthquake and 2) the behavior of the granular material inside the fault zone before, during, and after interacting with dynamic stress perturbations.

In nature, this granular material is known as “fault gouge”, essentially an unconsolidated mixture of crushed grains, as well as various fluids, which is found within most geologic fault zones. This is the weakest portion of a fault and is believed to be the most likely

area of future slip. Despite the importance, the basic physics of how intergranular friction in the fault core relates to the fault strength remains poorly understood, particularly in regards to the dynamic stresses such a system would experience via passing seismic waves.

Furthermore, in the case of an actual earthquake, the effects of the propagation direction, duration, and speed of rupture on nearby faults is not well categorized. The off-fault damage and radiation is strongly dependent on material properties of the medium and the fault geometry. Numerical models of fault zones have been used to predict how these details are manifested in the radiated seismic signal and the expected ground motion, however, the presence of granular material inside the fault is often ignored entirely in these fault-scale models, even though it undoubtedly plays a part in the triggering of slip on faults. Both the type of dynamic stress produced during rupture, and the influence those stresses have on granular material in the fault core are open questions that require careful study.

The inherent multi-scale nature of this problem has made linking the effects of the granular material on fault stability to the types of rupture events that can trigger slip on nearby faults quite difficult. Questions such as how pore fluid excitation influences slip nucleation and duration, as well as the rupture conditions capable of producing such excitations have yet to be examined in any meaningful way. Similarly, inquiries into the role fault gouge has in determining fault stability, the evolution of the fault gouge itself

during seismic events, and possible triggering of seismicity due to pore pressure changes in the gouge are all open areas of research.

As a way to begin studying these systems, a methodical examination of how dynamic stress perturbations of the gouge results in seismic slip, as well as the characterization of seismic radiation produced by different seismic rupture speeds in different media, is needed. We propose such a study by utilizing two separate numerical models for each aspect, and linking the results together into a more complete view of earthquake triggering.

1.2 Observations of Triggering

Earthquake prediction has long been a focus of the geophysics community, but one that has shown little progress in recent years. However, for several large earthquakes a causal relationship has been observed between the main shock and subsequent earthquakes occurring at distances greater than several rupture dimensions away (Hill et al., 1993; Gomberg and Davis, 1995; Brodsky and Prejean, 2005). This observational evidence of such naturally "triggered" earthquakes, coupled with our understanding of man-made earthquake triggering through fluid injection and withdrawal, convinced many that earthquakes do interact with each other, and that the occurrence of one earthquake may be used to predict where seismicity is likely in the near future.

Despite these observations, the underlying mechanisms that cause the new events remain unclear. Further complicating matters is the breadth of earthquake phenomena associated

with triggering, from typical aftershock distributions to aseismic afterslip on nearby faults or low-magnitude earthquake swarms (Hill et al., 1993). Triggering is also extremely common in areas of hydrothermal or magmatic activity, such as The Geysers in California (Gomberg and Davis, 1996), indicating that fluids may play an important role in the triggering process.

1.3 Static and Dynamic Triggering

The most successful explanations of fault triggering examine how faults interact through their stress fields, although changes in the strain or displacement field may also be relevant (van der Elst and Brodsky, 2010). Most of the observations addressed via the stress transfer model and are believed to be the result of either static or dynamic stress changes.

Static stress changes refer to instantaneous and permanent changes in the stress state surrounding a fault that has slipped. Stress is transferred along different portions of the slipping fault, with some areas being relieved of stress and others being increased. These deformations are time independent and attenuate rapidly with distance from the fault, typically as the inverse-cube of the distance from the main fault (Hill et al., 1993; Anderson et al., 1994).

These stress changes are incorporated into the well-developed Coulomb failure stress, given by

$$\Delta CFS = \Delta\tau_s - \mu(\Delta\sigma_n - \Delta P) \quad (1.1)$$

, where $\Delta\tau_s$ is the change in shear stress in the slip direction on the potential fault, $\Delta\sigma_n$ is the change in normal stress on the same fault, and ΔP is the change in pore pressure, and μ is the friction coefficient (Scholz, 2002).

Calculating *ΔCFS* depends on knowledge of the fault geometry and slip distribution of the causative earthquake, as well as the magnitude and orientation of the regional stress field and an estimate of μ (Scholz, 2002). In areas where *ΔCFS* > 0, the initial earthquake has increased the chances of slip on nearby faults, while *ΔCFS* < 0 has moved any local faults further from failure. Most aftershock distributions correlate strongly to positive *ΔCFS* regions, while negative regions form a "stress shadow" in which the fault is relaxed and the rate of seismicity has decreased (Stein et al., 1992; Harris, 1998).

In general, the Coulomb Failure Stress explains observations well, particularly the aftershock distribution and other near-field features. It has also shown that static stress changes as low as 0.01 MPa, just a fraction of earthquake stress drops, can trigger seismicity (King et al., 1994; Brodsky and Prejean, 2005), suggesting that many faults are critically stressed and very close to failure (Scholz, 2002). However, significant problems remain, in particular the inability of static stress changes to trigger earthquakes in the far field. The stress enhancement falls rapidly to zero at distances more than a few fault dimensions away, yet earthquakes have been triggered at distances of up to 17 fault dimensions (Hill et al., 1993). Another common feature of triggered earthquakes is a

time delay between the triggering agent, such as a static stress increase or the passage of seismic waves, and the triggered event. These earthquakes happen days, weeks, or even years after the main shock (Gomberg and Bodin, 1994; Gomberg et al., 2004). Static stress change models typically explain this time delay between events via a time-dependent frictional response of the fault to the static stress change, but this does not always match with observed triggering sequences and is highly dependent on the friction law chosen (Harris, 1998).

The first observations of an earthquake triggering events several hundred kilometers away come from the 1992 M_w= 7.2 Landers, CA earthquake (Hill et al., 1993). This earthquake resulted in a sharp increase in seismicity throughout the western United States for a period of hours to weeks after the initial event, including a M_s= 5.4 earthquake at Little Skull Mountain, over 200 km from Landers (Gomberg and Bodin, 1994). Subsequent observations, particularly of the 1999 Hector Mine earthquake, also in California, and the 1999 Izmit earthquake in Turkey, further contributed to the acknowledgement that earthquakes had the potential to interact with distant faults in a way that produced more earthquakes. Finally, the colossal 2002 M_w = 7.9 Denali, Alaska earthquake put the debate to rest by triggering seismicity from British Columbia to Mexico (Gomberg et al., 2004; Freed, 2005).

Since static stress changes diminish rapidly with distance from the fault, earthquakes triggered in the far field, several rupture dimensions away, are thought to be caused by

dynamic stress changes carried by transient seismic waves. Corroborating this, triggered events frequently begin just as surface waves pass the triggered fault (Brodsky and van der Elst, 2014). Dynamic stresses are just as capable of triggering near-field aftershocks, however, there are competing static stress changes that close to the fault, which makes identifying near-field events caused by dynamic stresses difficult (Freed, 2005).

One feature of dynamic triggering is a strong directivity effect, where triggered earthquakes are spatially related to the original rupture direction. Seismic energy is focused in the direction the rupture propagates, which results in the greatest dynamic stresses in this direction. Figure 1.1 shows the results of Gomberg et al. (2004) for the 2002 Denali rupture, where the direction of maximum radiation corresponds well with the regions of notable seismic rate increase (Figure 1.1).

While the occurrence of dynamic triggering is without doubt, the mechanism of failure is still unknown. A major problem with dynamic triggering is the transient nature of the stress perturbation, where the stress state returns to the initial state once the waves have passed. The expected seismicity would have to occur as the waves pass and the stress state is changed. This immediate triggering is seen, however, the bulk of dynamically triggered seismicity occurs after a delay of seconds to weeks following the original event (Freed, 2005). This implies that the dynamic stresses either change the system, and the failure criteria that must be met, or initiate a secondary mechanism that leads to rupture.

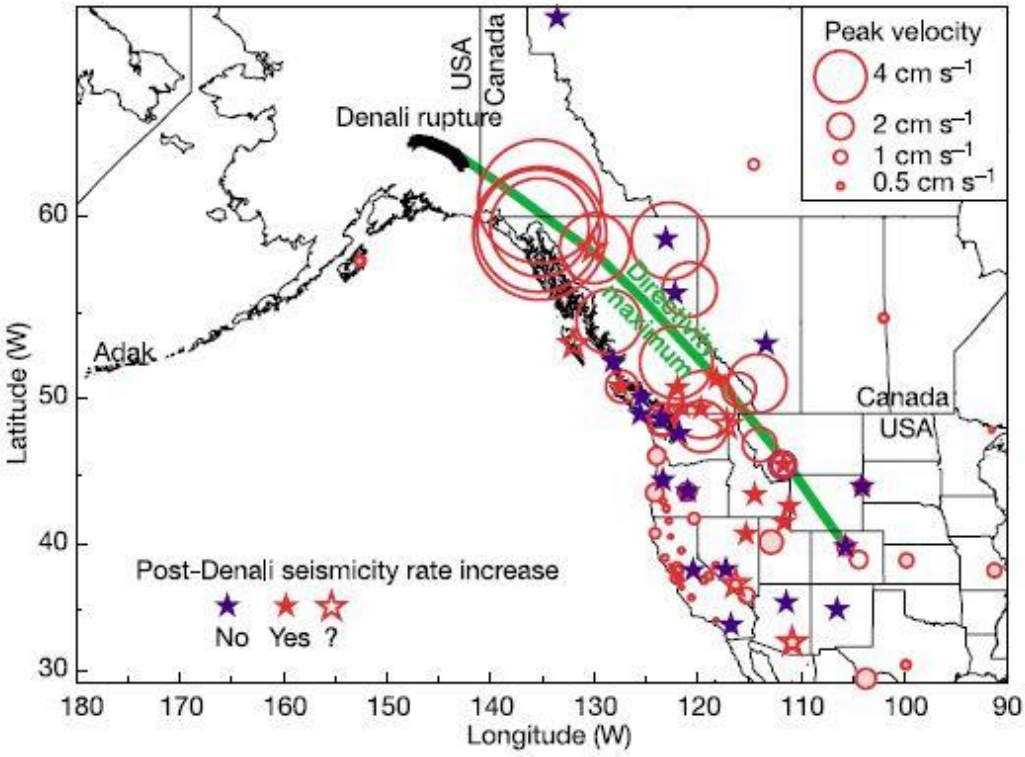

Figure 1.1 Reprinted from Gomberg et al. (2004), their Figure 4. Distribution of seismicity following the 2002 Denali earthquake and peak ground velocity measurements. The green bar indicates the direction of maximum radiation, as expected from a north to south propagating rupture. The sites with triggered rate increases are roughly consistent with the direction of maximum radiation.

At the very least, there seems to be a minimum amplitude threshold for dynamic triggering to occur (Gomberg and Davis, 1996; Prejean et al., 2004; Brodsky and Prejean, 2005; Van der Elst and Brodsky, 2010), but which property that threshold applies to (stress, strain, strain rate) and any exact values vary from study to study and cannot be generalized with confidence. Any understanding of which transients are most likely to trigger a new earthquake on a fault will rely on a more complete understanding of the failure mechanism. Such an understanding can only be found through a microscale

analysis of the stability of the slipping surface. For this, we must look at the granular material found in the fault core.

1.4 Granular Triggering

Recently, several authors have investigated the effect of dynamic perturbations on stressed granular materials. This stems from the current knowledge of fault structure which involves a narrow, highly strained zone termed the fault core where the most shear takes place (Chester et al., 1993). This core is filled with fault gouge, the broken and ground rock debris that forms from the two sides of the fault grinding against each other. The fault core is a zone of weakness and represents the portion of the fault where nucleation takes place.

A common way to study the behavior of fault gouge is through numerical modeling using the Discrete Element Method (Cundall and Strack, 1979). Previous studies have simulated grains in a confined area subject to shear stress, akin to an active fault zone. When the boundary of such a system is vibrated, simulating passing seismic waves, studies have found that slip can be induced in the grains. Such triggering also appears to be amplitude dependent, with a threshold below which no appreciable change in the system is detected. Larger amplitude vibrations have been shown to produce larger amplitude slip events, and vibrations typically result in a clock-advance of the slip event (Griffa et al., 2013; Ferdowsi et al., 2013), in general agreement with observations.

Several physical laboratory experiments on sheared glass beads subject to boundary vibrations have found that, when the system is near failure, the vibrations result in both immediate and delayed events, as well as a departure from the standard recurrence interval expected from the constant loading rate. The amount of departure is correlated with the amplitude and duration of the boundary vibration applied, and is believed to be due to the nonlinear elastic response of the modelled fault gouge (Johnson and Jia, 2005). Lab experiments indicate that seismic waves alter the frictional properties of the gouge, and the triggered events reflect a disruption of the internal fault zone structure (Johnson et al., 2008).

Both numerical and laboratory models have been unable to identify the exact alteration of the fault gouge that takes place when the system is dynamically stressed. To understand the true role fault gouge plays in promoting or inhibiting seismic events under dynamic forcing, a detailed study at the grain-contact scale must take place.

2. METHODOLOGY

This dissertation uses two different approaches, each utilizing a different code and focused on a different scale. Chapters three and four are studies using dynamic simulations of earthquakes in the region around fault zones to study ruptures on active faults, while chapter five uses grain-scale simulations to study perturbations of the granular fault core. Utilizing granular dynamics simulations in conjunction with earthquake rupture simulations has the potential to offer more insight into the mechanisms controlling earthquake triggering.

2.1 Dynamic Rupture Simulations

We performed experiments modeling rupture along entire faults for a variety of earthquake sizes and rupture speeds in order to obtain measurements of the stress, strain, and strain rate off the fault. These perturbations allow us to compare the pulses that stimulated failure in the granular material with the stresses produced by physically realistic ruptures. All rupture simulations were carried out using EQDyna, a 3-D finite element model used to simulate dynamic rupture and wave propagation in a variety of media. EQDyna has been parallelized using a hybrid MPI/OpenMP scheme so that it can run on modern cluster systems (Wu et al., 2011; Duan, 2012), and is adaptable enough so that the code may be altered to output measurements and parameters of interest for a specific problem.

To ease computation, the initial model consisted of a vertical strike-slip fault, 70 km long, extending down to a depth of 15 km. Faults with this geometry are needed to produce supershear ruptures, or ruptures that propagate at speeds faster than the shear wave velocity. Supershear ruptures are believed to cause more off-fault damage at greater distances than subshear ruptures (Madariaga, 1983), and as such may preferentially trigger nearby earthquakes. Our study includes several simulations of supershear and subshear ruptures to ascertain which rupture speed is more likely to result in further triggered events. The long length of the fault is also necessary so that the rupture can reach a steady-state velocity, allowing us to examine the typical seismic radiation produced.

Another major parameter that influences the off-fault stress and strain fields is the bimaterial contrast of the fault. Plenty of natural faults have the same material on both of the fault, but it is not uncommon for two different materials to be juxtaposed. Such bimaterial faults result in interesting rupture characteristics, not the least of which are the highly asymmetric damage generated off the fault and the large differences in peak ground motion caused by this asymmetry (Duan, 2008). In order to fully identify likely stress and strain changes away from the fault that have the potential to trigger new earthquakes, we must investigate the effects of such a material contrast.

As a first attempt to understand the dynamic changes produced by earthquakes, our experiment consisted of four simulations:

1) Uniform, Subshear rupture
2) Uniform, Supershear rupture
3) Bimaterial, Subshear rupture
4) Bimaterial, Supershear rupture

Each simulation had the exact same properties, with the only differences being in the initial shear stress level (to produce subshear or supershear ruptures) and the shear modulus (to produce the bimaterial contrast).

While any earthquake has the potential to trigger more earthquakes, both near and far, it has been observed that large magnitude earthquakes tend to have more pronounced results on future seismicity, that is, large earthquakes can be linked more clearly to subsequent triggered events (Hill et al., 1993; Gomberg et al., 2004). For this reason, we model large magnitude events, approximately M_w = 7 on a vertical strike slip fault. To produce earthquakes of this magnitude, as well as to ensure all the off-fault stresses are captured, simulations are run until the full length of the fault is ruptured.

During each simulation, measurements of the stress, the strain, and the strain rate within each element form the bulk of the model output. Here, we are less interested in the dynamics of rupture and more in the off-fault effects different ruptures can have. To fully capture the dynamic perturbations, these measurements should be recorded every time step (roughly $0.5\,\frac{\Delta x}{V_P}$ seconds) at distances stretching from meters to kilometers off the fault. Since this is a 3-D code, the same recordings should be output at the surface

and at depth. Unfortunately, due to computational limits, our current results only involve outputs to 0.5 km off the fault and 0.5 km from the surface. Even so, this discretization allows us to see how the off-fault stress evolves as the rupture travels along the fault, and how the stress perturbations change with distance from the rupture plane. Analysis of this data allows us to answer questions similar to those outlined below.

- Where is the stress or strain large enough to cause immediate triggering?
- Given the rupture direction, which side of the fault is most likely to see triggered events?
- What is the spatial extent (distance from the fault and depth) of the triggering zone?
- How do changes in physical properties of the earthquake alter the magnitude of stresses and strains?

These experiments, following this methodology, are aimed at identifying and quantifying the dynamic stress and strain fields produced by a variety of earthquake events. This information can be coupled with the granular output to infer which types of earthquakes may lead to future triggered events, and shed light on the underlying physical mechanisms of this increased seismicity.

2.2 Granular Simulations

The second approach used in this project involved a comprehensive suite of granular simulations. In this approach, a small section of fault gouge is simulated as a closely-packed 2-D system of particles that interact through elastic and frictional forces. In contrast to the approach of section 2.1, where an entire rupture along a full length fault was simulated, here the region is very small (several millimeters thick) and two

dimensional, however the initiation of earthquakes still emerges from this simple model, particularly the drop in frictional strength as the system begins to shift (Aharonov and Sparks, 2004).

The granular code initiates these simulations by filling an empty box of specified dimensions with two-dimensional circular uniform grains of various diameters chosen from a clipped Gaussian distribution. The code uses the discrete element method to track the motions of each grain, as well as the stresses they experience. For this reason, two dimensional simulations greatly ease the computational burden. The simpler geometry also makes analysis of the particle motion and frictional strength during and after the pulse more tractable.

Once the grains are created they are compressed under a constant normal force until a predetermined porosity is met (Figure 2.1). Small vibrations of the system are allowed to die out, at which point the system is loaded by a spring attached to the top wall of the box. The top wall consists of cemented half-grains that are not free to roll, but provide some roughness to the system. Loading continues until the frictional strength of the system is reached and the grains deform by frictional sliding and rolling into a new configuration. This simple system mimics a block-slider model where the static friction from the locked grains transitions to a natural drop in frictional resistance (dynamic friction) once the grains begin to shift.

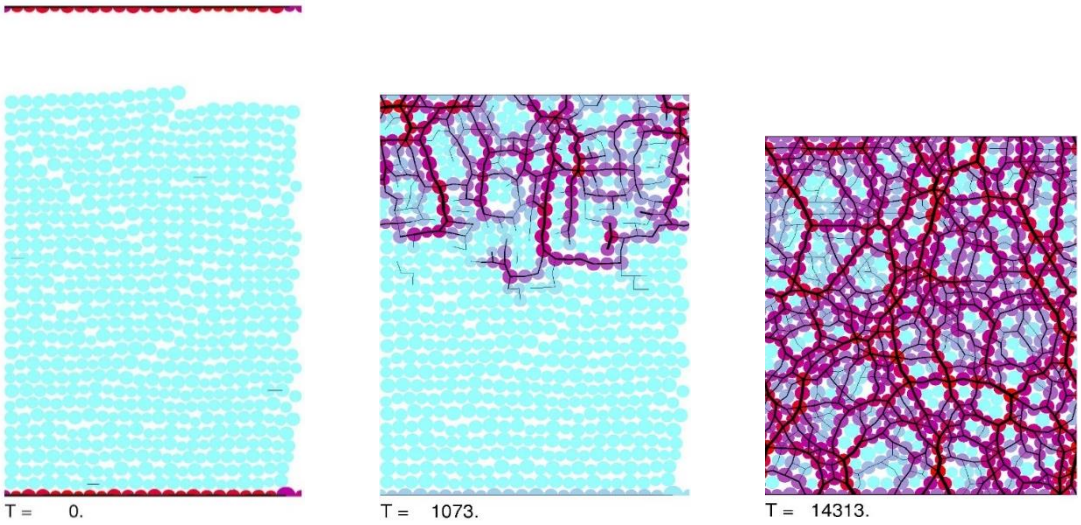

Figure 2.1 Compaction of grains in the GranFrix code. A box of a specified height and width is filled with loose grains. The top wall of the system is lowered under a fixed normal force until the system is as near to the specified porosity as possible. The colors represent forces on the grains with blue being unstressed and red being highly stressed.

For this study on earthquake triggering, the granular system was taken through a failure event just as described above. This allowed for measurement of the peak strength and stress drop of the system to be made for that single event. Taking advantage of the numerical model, the system was then reset to a point before the peak strength was reached and run again, with slight modifications to model parameters.

Since much of the uncertainty surrounding earthquake triggering relates to the dynamic stresses carried by seismic waves, this is what we aim to model. To mimic the effect of passing waves, a slight perturbation of the normal stress was induced in the system before it reached failure. To begin, the pulse was a single sinusoidal wavelet with a fixed frequency. The frequency range of the pulses was chosen to be low enough to ensure perturbations travelled through the granular packing to the bottom of the system. Higher

frequencies tend to damp out within a few grain radii, while lower frequencies shake the entire system in a non-physical way. The frequencies in this study correspond to grains with millimeter diameters, and therefore represent the highest frequencies expected from earthquakes, in the kHz range. A possible avenue for further research is investigating the frequency dependence of any behavior seen (Brodsky and Prejean, 2005), as well as the grain-size dependence. It is also possible to change the functional form of the pulse from a sinusoidal function to a more complicated function, however, the results from the earthquake rupture code show general agreement between off-fault stress perturbations and the shape of our pulses to the granular system.

Initially, the amplitude of the pulse was varied to determine the threshold for immediate failure, while pulsed runs that did not immediately fail were reloaded until the next slip event occurred. The model was pulsed at a series of different stress levels during the loading history to address questions about how far from failure a fault can be, while still being susceptible to dynamic triggering. In this way, a comprehensive suite of experiments detailing all possible responses of the system to pulsing was constructed.

Upon completion of the granular experiments, an entire group of over 100 simulations was available for study, which allowed us to constrain the threshold for immediate triggering as well as study the mechanisms leading to delayed triggering. Such a large data set also made it possible to search for patterns and relations between the stress level,

the pulse amplitude, and the resultant events. Some questions a study like this may answer include:

- Does immediate triggering tend to result in a larger stress drop?
- Are the amplitudes for immediate triggering observed in the real world?
- How does the amplitude for immediate triggering relate to the stress level during the pulse?
- How does the amplitude for immediate triggering vary between grain configurations?
- What control does the normal stress have on the ability to trigger a system?

Along with these questions, the highly detailed runs completed here afforded us the opportunity to study the micromechanics of the system before, after, and even during the slip event. Such precision is needed to determine slight changes in grain position or the stress distribution among the grains that might lead to immediate failure. This detail can also be used to better understand what the pulse changes in the system, and why those changes may result in a different slip event.

The work discussed above was completed in a dry granular system to help develop the most effective analysis tools to understand the evolution of the pulsed systems, as well as to validate the output of the code with previous work. However, the presence of fluid is expected in most fault zones and it is believed that fluid flow and migration may play a large role in dynamic triggering (Gomberg and Davis, 1996). For this reason, a major next step in this research will be to ultimately perform the same comprehensive simulations on a fluid-filled gouge to study the influence of fluid on gouge stability.

The system chosen for this study was a 48 grain x 48 grain ensemble. This provides enough grain contacts and stress chains to fully capture the granular dynamics. Our simulated systems consist of near 3000 grains and around 6650 grain contacts, each of which are tracked at every time step in the Discrete Element method, making larger system computationally difficult. Additionally, the width of the sheared layer is set to be several times the width of the shearing zone in a typical slip event, which tend to localize among three to eight rows of grains. This ensures that the dynamics of slip are not contaminated by the boundaries.

3. INFLUENCE OF INITIAL STRESS AND RUPTURE INITIATION PARAMETERS ON FORBIDDEN ZONE RUPTURE PROPAGATION*

Well established theoretical and numerical results of 2-D ruptures have been accepted for years to limit the speed of mode II cracks to be below the Rayleigh velocity or above the shear wave speed. However, recent work has numerically produced rupture speeds in this so-called "forbidden zone", that is, the region of rupture velocities between the Rayleigh wave speed and the shear wave speed, for 3-D simulations. We verify that finding here and further examine the dependence of that behavior on initial stress and rupture initiation parameters. Using a 3-D finite element model for dynamic rupture propagation, numerical experiments were performed for different initial stress conditions as well as different size initiation patches and forced rupture velocities. It is shown that the initial stress on the fault has a strong influence on the resulting rupture, specifically with regards to the distance at which the rupture transitions to supershear speeds, the maximum rupture velocity attained on the fault, and how rapidly the rupture passes through the forbidden zone. It is also demonstrated that for the same initial stress, increasing the size of the nucleation patch or the speed of forced rupture can artificially increase the gradient of the rupture velocity within the forbidden zone. This suggests that

* Reprinted with permission from Oxford University Press, "Influence of initial stress and rupture initiation parameters on forbidden zone rupture propagation", by R.M. Payne and B. Duan, 2015. *Geophysical Journal International*, 201, 70-77, Copyright 2015 by R.M. Payne and B. Duan.

the rupture is uniquely predetermined by the stress state and material properties of the fault and surrounding medium in these models.

3.1 Introduction

While the theoretical possibility that shear ruptures may propagate faster than the shear wave speed has existed for decades (Burridge, 1973; Andrews, 1976; Burridge, 1979), observations of supershear ruptures in nature (Bouchon, 2001; Bouchon and Vallee, 2003; Dunham and Archuleta, 2004) and in the lab (Rosakis et al., 1999; Xia et al., 2004) around the turn of the century provided the tangible proof needed for mainstream acceptance. Since then it has been believed that, while rupture speeds faster than the shear wave speed were permissible, the velocities between the Rayleigh wave speed and shear wave speed were energetically impossible for Mode II cracks (Broberg, 1996; Broberg, 1999), forming a "forbidden zone" of rupture propagation speeds. Rupture in the purely Mode II mechanism was believed to either propagate at sub-Rayleigh or supershear speeds with a discontinuous transition between the two. However, these conclusions were reached with a 2D analysis. Recently, Bizzarri and Das (2012) have shown that sub-Rayleigh ruptures in the Mode II direction proceed continuously through the forbidden zone during the supershear transition in 3D calculations.

The main goals of this paper are to reproduce the smooth forbidden zone transition found by Bizzarri and Das (2012), as well as investigate the dependence of this transition on the initial stress state and determine any possible influence rupture initiation parameters have on the results. The initiation procedure used here, commonly seen in the

spontaneous rupture community, artificially forces rupture to travel at a fixed velocity inside a predetermined rupture patch. While most simulations of dynamic rupture are more concerned with rupture propagation than initiation, it is possible that this artificial procedure introduces behaviors in the model that would not be expected in natural ruptures. We aim to identify which results stem from the underlying physics and which are due to the artificial nucleation procedure.

In general, it is important to understand the behavior of supershear ruptures because it is believed that supershear ruptures produce higher ground motion at farther distances from the fault compared to subshear ones (Dunham and Archuleta, 2005; Dunham and Bhat, 2008; Bizzarri et al., 2010). Additionally, the rupture speed, and changes to it, control the amount of radiation emitted at wavelengths that can cause the most structural damage (Madariaga, 1983). A deeper understanding of the supershear rupture process and its transition is needed to more successfully mitigate this hazard.

3.2 Method

In order to study questions of forbidden zone penetration and the supershear transition, we use the 3-D finite element code EQDyna (Duan and Oglesby, 2006; Duan and Oglesby, 2007; Duan, 2012) to simulate spontaneous dynamic rupture and wave propagation in a homogeneous medium on multi-core cluster systems. The code numerically solves the elastodynamic equations with the traction-at-split node (TSN) method to characterize the fault boundary, adopting the formation given by Day et al. (2005), which provides a consistent treatment for fault behavior (at a given pair of split

nodes) at all times, including prerupture, initial rupture, arrest of sliding, and possible reactivation and arrest of sliding.

Fault frictional properties in this research obey a linear slip-weakening friction law (Ida, 1972; Andrews, 1976; Day, 1982), expressed as $\mu(\delta) = \mu_s - (\mu_s - \mu_d)\min(\delta, d_o)/d_o$, where μ_s, μ_d, δ, and d_o are the static and dynamic coefficients of friction, the slip on the fault and the critical slip distance, respectively. Rupture is initiated artificially within a nucleation patch with radius I_{nucl} by forcing ruptures to grow at a fixed speed, v_{rupt}. Outside of the nucleation zone, ruptures propagate spontaneously and the rupture speed forms part of the dynamic solution. Uniformly spaced square elements discretize the fault with Δx spacing between nodes. The fault is surrounded by a larger buffer region with gradually increasing element size to prevent contamination via artificial reflections from the model's artificial boundary (except at the free surface). The code has been verified extensively with the Southern California Earthquake Center (SCEC)/ USGS code validation exercises (Harris et al., 2009), and has been parallelized using a hybrid MPI/ OpenMP scheme so that it can run on modern cluster systems (Wu et al., 2011; Duan, 2012).

We consider a planar, vertical fault that separates two isotropic, perfectly elastic media having identical properties. The fault extends to a distance L_f in the x_1 (strike) direction, down a distance W_f in the x_3 (dip) direction, and is sketched in Figure 3.1. The initial shear stress is parallel to the x_1 direction, and subsequent rupture is strike-slip. The

medium is initially in equilibrium with an initial stress that is homogeneous over the whole fault plane. The material properties and fault constitutive parameters used in the present study are summarized in Table 3.1 and are identical to those used by Bizzarri and Das (2012). The spatial discretization, Δx, temporal discretization, Δt, and the initial shear stress, τ_o, all vary from experiment to experiment and are not included in Table 3.1.

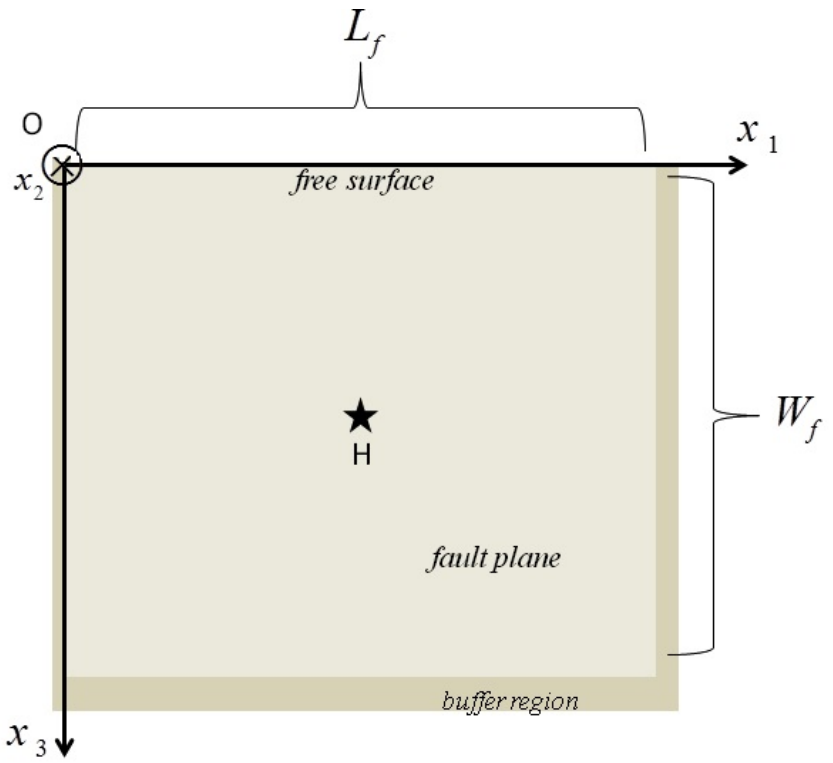

Figure 3.1 Model fault plane. Rupture begins at the hypocenter and spreads out in all directions along the vertical plane. Material properties are listed in Table 3.1.

The bulk of the dynamic simulations presented have a Δx of 25 meters and contain about 195 million elements. Simulations were run until a termination time of 2.1 seconds with

a time step of $6x10^{-5}$ seconds, using 256 cores on a supercomputer system with 2.8 GHz Nehalem quad-core X5550 processors. Each simulation takes approximately 7.5 hours of wall-clock time and outputs 100 MB of data.

Table 3.1 Model discretization and constitutive parameters

Parameter		Value
Medium and Discretization Parameters		
Lame's constants	λ = G	35.9 GPa
S-wave velocity	v_s	3.464 km/s
Rayleigh velocity	v_R	3.184 km/s
P-wave velocity	v_P	6 km/s
Fault length	L_f	16 km
Fault width	W_f	12 km
Final time	t_{end}	2.1s
Hypocenter Location (along strike, down dip)		(8,7) km
Fault Constitutive Parameters		
Magnitude of effective normal stress	σ_n	120 MPa
Static friction coefficient	μ_s	0.677
Dynamic friction coefficient	μ_d	0.46
Characteristic slip-weakening distance	d_o	0.4 m

Material parameters are identical to those used in Bizzarri and Das (2012).

3.2.1 Determination of Spatial and Temporal Discretization

In order to keep the duration of the experiments reasonable, we searched for the largest possible stable time step that still yielded high-resolution results. Typically, the time step chosen corresponds to the spatial discretization (e.g., Duan and Day, 2008) as

$$\Delta t = \alpha \frac{\Delta x}{v_P} \tag{3.1}$$

where v_P is the P wave velocity and α is a coefficient valued between 0 and 1 known as the Courant-Friedrich-Lewy (CFL) number (e.g., Slingerland and Kump, 2011). Essentially, this requires the time step to be small enough to capture changes happening within Δx at the fastest possible speed, v_P. For smaller spatial discretizations, a correspondingly smaller time step is given when using a fixed coefficient.

While values of α= 0.6 are typical (Day et al., 2005), the need to resolve the rapid forbidden zone transition requires a significantly smaller time step. As seen in Bizzarri and Das (2012), an α = 0.144 is suitable, however when paired with the smaller spatial step they used (Δx = 5m), the duration of these simulations becomes prohibitively large, and precludes the possibility of completing multiple experiments.

In order to balance the time demand with the need for high resolution, we utilized a larger spatial step, but a smaller time step than Bizzarri and Das (2012). As shown in Figure 3.2, the same general behavior is seen for all four levels of spatial discretization. Each curve in Figure 3.2 shows the rupture velocity from four different simulations with

the same starting parameters, but a different level of discretization. For each run, Δt was determined with α = 0.0144 in equation 3.1. All runs show a steady increase through the supershear transition. While the 100 m data shows obvious variations with respect to the 12.5 m run, the 25 m curve closely trails the 12.5 m data. Significantly, the finest resolution run at 12.5 m took over 12 hours to complete, while the 25 m run took less than six. Since the two curves yield essentially the same results, a spatial discretization of Δx = 25m is used for the remainder of this paper so as to minimize the resources required per simulation and maximize the total number of simulations possible.

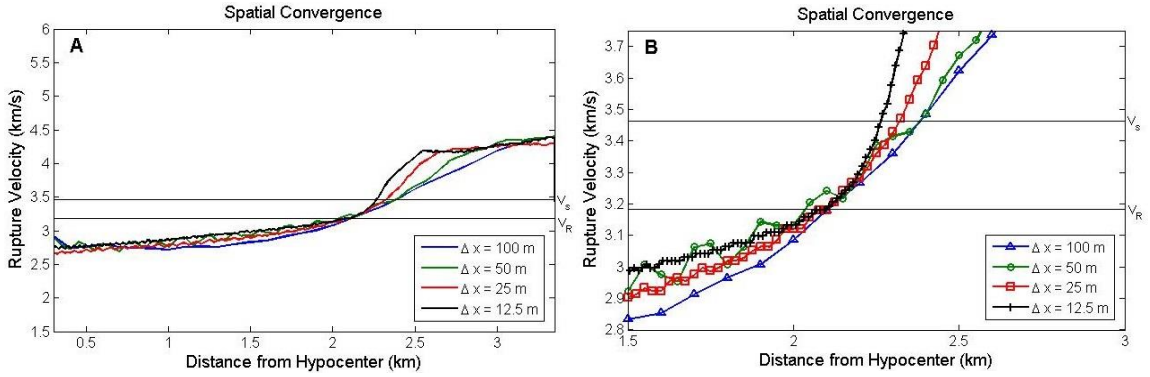

Figure 3.2 Comparison of spatial steps. Each run has $\boldsymbol{I_{nucl}}$ = 1600 m, $\boldsymbol{v_{rupt}}$ = 2750 m/s, and an initial stress of 73.8 MPa, with the only difference being the size of Δx, and the corresponding Δt. (A) Rupture velocity along the fault length. We utilize 25 meters as our Δx for the majority of simulations because of the near-perfect match to the 12.5 m discretization and significantly faster run time. (B) Close-up view of the forbidden zone, with markers indicating the discrete points of computation. Decreasing the spatial step size increases the number of points measured in the forbidden zone.

To validate that the various spatial discretizations are actually converging to the same solution, the root-mean-squared difference is calculated and shown in Figure 3.3. The RMS difference is calculated by taking the difference between the rupture times of the

run with grid size Δx and the reference run, which is the finest resolved case with Δx = 12.5m. The difference is expressed as a percentage of the mean rupture time of the reference solution. It is clear that the 25 m solution is within about 1% of the 12.5 m result, indicating that using the costly higher resolution does not add much new information and thereby justifying our use of the coarser element size.

We also quantify the resolution via the number of spatial elements within the cohesive zone, given by the parameter $N_c = \frac{\lambda}{\Delta x}$, where λ is the width of the cohesive zone. Due to the shrinking of the cohesive zone as rupture progresses, we follow the convention of Day et al. (2005) and report $\overline{N_c}$, the median value of N_c in the Mode II direction in Table 3.2 for the runs in Figure 3.2.

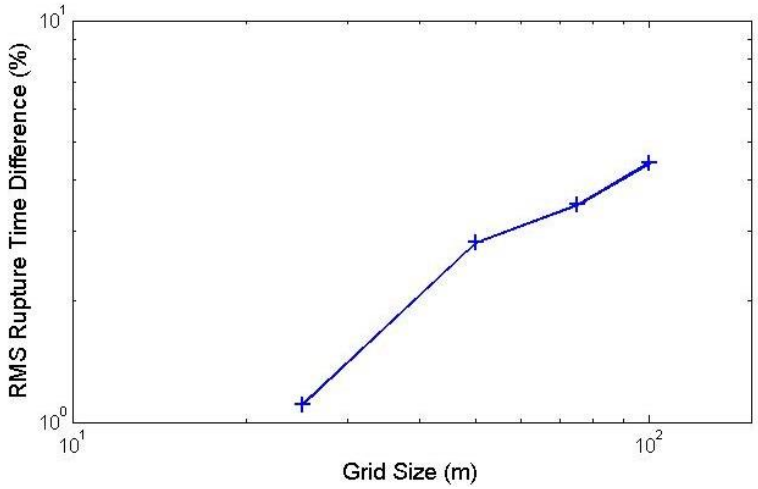

Figure 3.3 The root-mean-squared difference of the rupture times computed for different runs. The reference run is the 12.5m discretized run and the result is expressed as a percentage of the mean rupture time of that reference run. The 25m run has a difference of 1.11% from the 12.5m data, indicating that decreasing the step size is not worth the increase in resources.

While a spatial step of 25 m captures details along the fault and within the cohesive zone as well as a finer spatial step would, to fully resolve the forbidden zone transition a very fine time step (i.e., a very small CFL number) is needed as well. Figure 3.4 shows a sequence of 25 m runs with progressively smaller time steps. The "plateaus" seen in the rupture velocity plot within the forbidden zone for the two larger time step cases indicate that the recorded rupture time is not refined enough to discriminate between differing rupture times. Simply put, the time step is too large. By decreasing the time step (α), for the same Δx, the curve naturally smooths out as the true rupture times are captured. We remark that we use $\alpha = 0.0144$ for the results in the next section to fully resolve forbidden zone penetration without the need for any smoothing or manipulation.

Table 3.2 Cohesive Zone Resolution

Δx (m)	$\overline{N}_c$
100	6
50	11
25	22
12.5	50

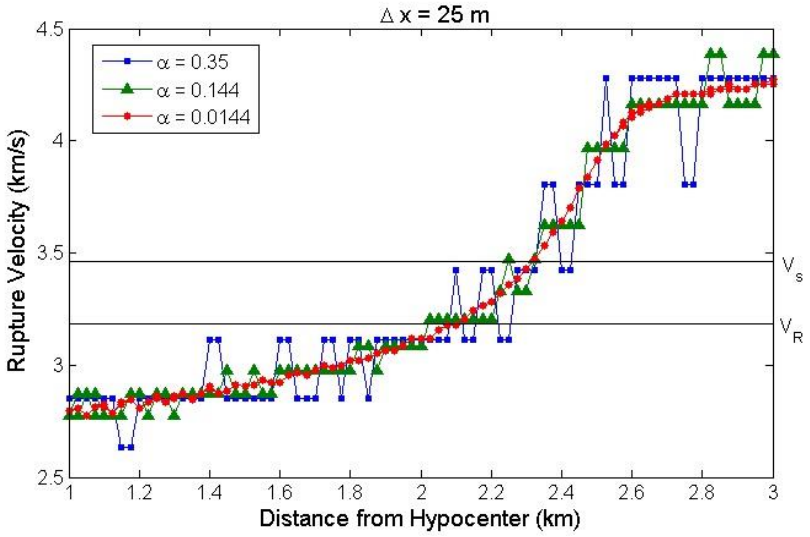

Figure 3.4 Rupture velocity calculated using three separate time discretizations. Again, $\boldsymbol{I_{nucl}}$ = 1600 m, $\boldsymbol{v_{rupt}}$= 2750 m/s, and $\boldsymbol{\tau_o}$= 73.8 MPa. The larger time steps show "plateaus" in the rupture velocity, or series of points at the same velocity. By drastically decreasing the time step, the curves become smooth as more true rupture velocities are resolved and calculated. Utilizing very small time steps in conjunction with larger spatial steps is an effective method for resolving the forbidden zone transition without requiring an overabundance of computing resources.

3.2.2 Data Processing

Throughout this work we will analyze the rupture velocity, however, it is important to note that our simulations actually record the rupture time at each node. The rupture velocity is then calculated from the gradient of the rupture time curves:

$$v_r(x_1, x_3) = \frac{1}{\|\nabla_{x_1,x_3} t_r(x_1,x_3)\|} \tag{3.2}$$

where t_r is the rupture time, defined as the time at which the slip rate at that node exceeds 0.01 m/s, which is chosen to properly capture the sharp rupture velocity increase

prior to the supershear transition, following Bizzarri and Spudich (2008) and Day et al. (2005). For a mode II rupture, this can be written out in terms of the node numbers as

$$v_r(i,j) = \frac{2\Delta x}{t_r(i+1,j) - t_r(i-1,j)} \tag{3.3}$$

where the ordered pair *(i, j)* indicate a node at *iΔx* along strike and *jΔx* down dip, with Δx being the spatial discretization. Equation (3.3) represents a simple centered difference in the along-strike direction, equivalent to measuring the slope of the travel time curve for a mode II rupture at the hypocentral depth. We remark that we mainly examine mode II rupture propagation in this study.

The gradient of the rupture velocity was only calculated within the forbidden zone. In this region, typically containing seven to ten points at the 25m discretization, the rupture velocity is approximated by a straight line and the gradient is calculated by finding the slope of this line. More specifically,

$$\frac{dv_r}{dx} = \frac{1}{n}\sum_1^{n-1} \frac{v_r(i+1) - v_r(i)}{x(i+1) - x(i)} \tag{3.4}$$

where *n* is the number of points within the forbidden zone. Essentially we report the average of the gradient in the forbidden zone.

3.3 Results

Numerical trials were carried out to study the effect of different initial stress conditions and initiation parameters on the resultant rupture, focusing specifically on the changes in

the forbidden zone penetration and supershear transition. Selected experiments are reported in Table 3.3.

Table 3.3 Nucleation parameters and measured quantities for selected trials

Run name	S factor	I_{nucl} (km)	v_{force} (km s^{-1})	dv_r/dx	L_{trans} (km)
Δx = 25m					
A	0.5	1.4	2.75	0.8088	2.775
B	0.5	1.607	2.75	1.0681	2.825
C	0.5	1.863	2.75	1.1042	2.800
D	0.4	1.138	2.75	1.7222	2.25
E	0.4	1.4	2.5	1.4462	2.325
F	0.4	1.4	2.75	1.1086	2.325
G	0.4	1.4	3.0	3.0365	2.350
H	0.4	1.632	2.75	1.1231	2.325
I	0.3	0.984	2.75	6.0731	2.0
J	0.3	1.207	2.75	1.2634	1.75
K	0.3	1.4	2.75	1.2813	1.75

dv_r/dx: Rupture velocity gradient within the forbidden zone,
L_{trans}: transition length measured from hypocenter

3.3.1 Variations in Initial Shear Stress

When changing the initial shear stress on the fault, we are moving the fault either closer to or farther from failure for the same normal stress. By decreasing the initial shear stress, the fault must experience more loading before rupture and hence the fault is stronger. Similarly, increasing the initial shear stress results in the opposite case, where the fault is weaker because it is closer to failure. A common parameter to measure how close a fault is to failure is the strength parameter or S value (Das and Aki, 1977), $S = \frac{\tau_u - \tau_o}{\tau_o - \tau_f}$ where τ_u is the upper yield stress, τ_o is the initial shear stress and τ_f is the final

residual stress. We tested several cases corresponding to S values of 0.3 (τ_o = 75.23 MPa), 0.4 (τ_o= 73.8 MPa) and 0.5 (τ_o = 72.56 MPa), for the same yield and residual stresses computed from the parameters listed in Table 3.1, that is, $\tau_u = \mu_s \sigma_n^{eff}$ = 81.24 MPa and $\tau_f = \mu_d \sigma_n^{eff}$ = 52.2 MPa. While τ_o is a convenient parameter to alter, it is important to note that what we are truly changing is the S parameter, which reflects the relative stress levels on the fault instead of absolute values. Additionally, although supershear ruptures are believed to occur for S values as high as 1.19 (Dunham, 2007), increasing the S value also increases the distance at which the rupture completes the transition to supershear speeds. Since our focus is on studying the supershear transition, our experiments use much lower S values in order to cause transitions within the first few kilometers.

Two separate series of experiments were completed. Initially, the only alteration between runs was the initial shear stress level. This is seen in runs A, F and K where each experiment was nucleated with a forced velocity of 2750 m/s and an initiation zone radius of 1.4 km, while using a spatial discretization of 25 meters and a time step of 6 x 10^{-5} seconds (i.e., α = 0.0144). In all experiments, our results confirm those of Bizzarri and Das (2012), i.e., Mode II rupture transitions smoothly from sub-Rayleigh initiation speeds through the forbidden zone and into the intersonic regime. We also see a shrinking cohesive zone for every run after transitioning to supershear speeds, as will be discussed later.

By looking at the rupture velocity data in Figure 3.5, it is clear that although each run transitions to intersonic speeds, and starts with the same initiation parameters, the evolution of the rupture velocity curve is quite different for the differing stress conditions. First note that even though each run is initiated with the same rupture speed, the actual rupture speed is higher or lower depending on the initial stress condition. The highest initial stress consistently caused the rupture to travel faster than the speed prescribed within the initiation zone. We remark that the prescribed rupture velocity is used to calculate the time at which the fault strength at that point starts to drop, while our recorded rupture time at the point is when the fault point reaches the threshold slip velocity of 0.01 m/s, as used in the previous study by Bizzarri and Das (2012).

Furthermore we can see that the strongest fault, i.e., the one initially furthest from failure with the lowest shear stress, is the last to achieve supershear velocity, while the weakest fault transitions first, in agreement with the assertion by Day (1982) that increasing the strength also increases the distance at which a given rupture velocity is reached. This was also seen in Festa and Vilotte (2006), where increasing the S value resulted in a larger distance of propagation before the supershear transition occurred.

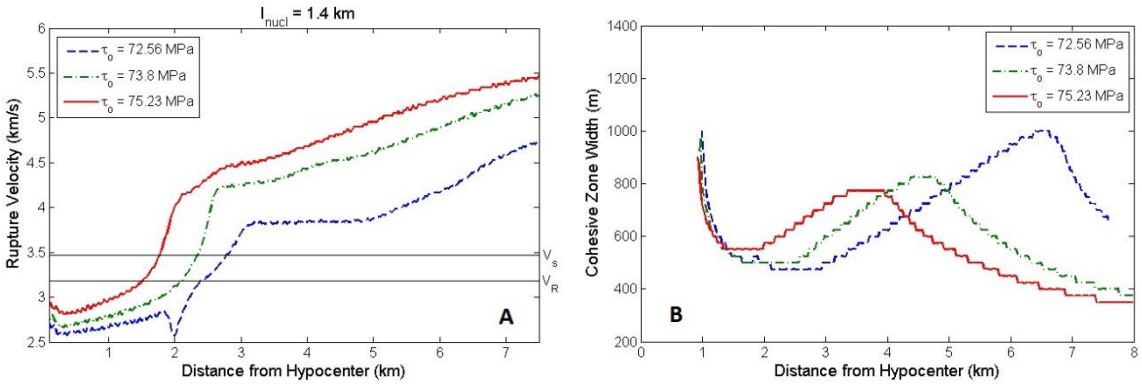

Figure 3.5 Mode II rupture velocity for several experiments (A, F and K in Table 3.3) with various initial stress conditions and the same $\boldsymbol{l_{nucl}}$ (A). Cohesive zone width for the same three experiments (B). The forbidden zone consists of the rupture velocities between the two lines at $\boldsymbol{v_R}$ and $\boldsymbol{v_s}$.

It appears that each rupture also approaches a different final velocity, from 4.75 km/s to 5.5 km/s. However, from fracture mechanics arguments it is likely that all of the rupture speeds are continuously increasing to the P wave velocity (Broberg, 1996; Andrews, 2002), but the length of the fault truncates the velocity curves and this final speed is not readily apparent. In this case, the variations in the initial stress will not affect the final rupture velocity, and instead will control the length of time and the distance needed to reach that ultimate velocity.

Besides the supershear transition point and the final rupture velocity, measurements were also made of the rupture velocity gradient in the forbidden zone directly before transition to supershear speeds. This was done by approximating the rupture velocity increase through the forbidden zone as a straight line as discussed in section 3.2.2. Bizzarri and Das (2012) found rupture propagated through the forbidden zone rapidly for the given initial stress condition they examined (τ_o = 73.8 MPa). Here, we aim to

examine if and how this behavior may depend on the initial stress state. The strongest fault was found to pass through the forbidden zone the slowest with a low gradient of just 0.81 km/s per km. In contrast, the weakest fault passes quickly through the forbidden zone with a measured gradient of 1.28 km/s per km along the fault. The median stress condition also has the median velocity gradient of 1.11 km/s per km. This relationship between fault strength and the velocity gradient through the forbidden zone can be explained as follows. Assuming that each set of initial conditions, i.e., stress and friction values, corresponds to a specific rupture for that medium we can say that for the same nucleation radius, weaker faults (with higher initial stress) would be expected to transition to supershear velocities sooner. As such the velocity gradient must be steeper for the same nucleation radius in order to transition closer to the hypocenter.

A second group of experiments were performed to ascertain if this finding, that the rupture velocity gradient within the forbidden zone depends on the initial stress state, is a robust feature. These experiments, composed of runs B, F and J, were constructed to have initiation zones that were the same ratio with respect to the critical radius, r_c. The critical radius, $r_c = \frac{7\pi}{24} G \frac{\tau_u - \tau_f}{(t_o - t_f)^2} d_o$ as determined by Day (1982), is the radius at which the energy released during crack propagation is equal to the energy required to propagate the crack. Essentially, a crack must be at least as long as the critical radius to propagate spontaneously. In dynamic rupture simulations the critical length is a commonly used fundamental length scale and provides an easy parameter to describe the size of the

initiation patch. However, the critical radius is dependent on the initial stress, meaning that each initial stress condition will correspond to a different critical radius.

The first round of experiments presented set each initiation patch to the same size (1400 m), regardless of the critical radius for that stress condition. This means the initiation patch was a different multiple of the critical radius in each case, that is, the ratio of I_{nucl}/r_c was equal to different value for each stress state. The second round of experiments presented in Figure 3.6 were tailored so that the ratio I_{nucl}/r_c remained constant, even as the initial stress condition changed. For the weakest to strongest faults, the critical radii are 853.99 m, 990.36 m and 1136.89 m, and the nucleation patch is set to $1.414r_c$ for each, allowing us to verify that the rupture velocity gradient depended on the initial stress, and was not an artifact of the initiation procedure.

Figure 3.6 shows the result from this second set of experiments. It is clear that the rupture velocity gradient within the forbidden zone depends on the initial stress state in the same way as the first set of experiments. From these two sets of experiments, we conclude that how fast rupture propagates through the traditional "forbidden zone" depends on the initial stress state. A lower initial shear stress results in a smaller rupture velocity gradient within the forbidden zone, as long as the stress state allows for a supershear transition.

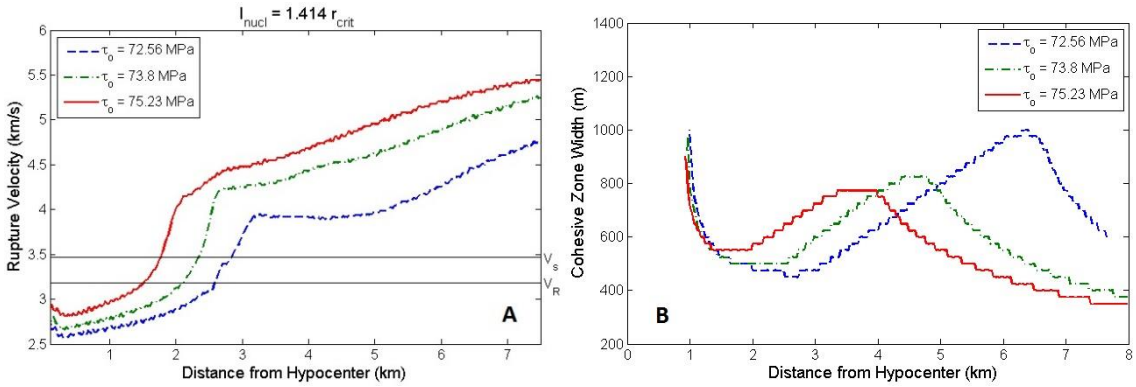

Figure 3.6 Mode II rupture velocity for several experiments (B, F, and J in Table 3.3) with $\boldsymbol{I_{nucl}}$= 1.414$\boldsymbol{r_c}$ meters (A), where $\boldsymbol{r_c}$ = 853.99 m for$\boldsymbol{\tau_o}$ = 75.23 MPa, 990.36 m for$\boldsymbol{\tau_o}$= 73.8 MPa and 1136.89 for $\boldsymbol{\tau_o}$= 72.56 MPa. Cohesive zone width plotted in B.

We also examine how the initial stress state may affect the evolution of the cohesive zone (Figure 3.5 and 3.6, B). The cohesive zone is the area between the leading edge, the locus of points at the yield stress that have just started to slip, and the trailing edge, where all the points have slipped the characteristic slip distance, d_o. As reported in Bizzarri and Das (2012), for a given initial stress state, the width of the cohesive zone in the pure Mode II direction initially decreases as rupture accelerates, then increases as the leading edge approaches and passes through the supershear transition, before finally decreasing to a final width as the trailing edge starts to speed up. While our experiments agree with this evolution, as shown in Figure 3.5B and 3.6B, the distances at which the cohesive zone becomes narrower or wider depends on the initial stress state. The highest initial shear stress begins the final narrowing closest to the hypocenter, whereas the lower shear stress runs begin to narrow further down the fault. In addition, the magnitude of the cohesive zone peak, i.e., the largest width the cohesive zone reaches, after the supershear transition also depends on the initial stress state as evidenced by the

fact that the highest initial stress state shows the smallest peak (least amount of widening), while the lowest stress case has the largest peak.

The observations can be explained by close examination of the rupture velocity. The highest stress case transitions to supershear speeds the earliest, and once supershear, the rupture velocity changes to a shallower and constant gradient that coincides with the onset of the cohesive zone widening, about 2 km from the hypocenter. Once the rupture reaches this apparent steady-state acceleration, the trailing edge begins to catch up to the leading edge and the final narrowing of the cohesive zone width begins. The fact that the cohesive zone begins to shrink after a minimal amount of widening in the high stress case means the trailing edge is never too far behind or much slower than the leading edge. This means the higher stress cases not only have a larger, but also a more rapid stress drop than the lower stress cases, something which may be evident in the high-frequency radiation emitted from the fault. Despite differences in when the narrowing occurs, we expect the cohesive zone to approach the same final width for each stress condition as the rupture velocity approaches v_P. In this situation, the initial stress determines how rapidly the cohesive zone approaches the final width.

3.3.2 Variations in Rupture Initiation Parameters

Several experiments were also completed that varied the rupture initiation parameters used to start a spontaneous rupture. Rupture was forced within a specified "initiation patch" of radius I_{nucl} at a speed v_{rupt}. Choosing from within a suitable range of I_{nucl} and v_{rupt} allows the rupture to propagate spontaneously outside of the initiation patch.

The initiation patch is typically slightly larger than the critical radius for spontaneous crack growth, r_c, and is forced at speeds greater than half the shear wave speed, β/2 (Day, 1982; Bizzarri et al., 2010). While this procedure is highly artificial, for most rupture dynamics simulations the initiation of the rupture is less important than the propagation of rupture and this procedure is commonly used.

The experiments that varied the size of the initiation patch, I_{nucl}, for the same stress level are shown in Figure 3.7A (runs A, B, C), Figure 3.7B (runs I, J, K) and Figure 3.8A (runs D, F, H). Unsurprisingly, the curves all overlay each other inside the nucleation zone and for several hundred meters of spontaneous propagation. However, if the initiation patch is too small, the resultant rupture is quite different. From Figure 3.7, it appears that rupture patches less than about $1.4r_c$ can initiate ruptures with rapidly oscillating propagation speeds, characterized by the sharp dip in v_{rupt} before the supershear transition. In contrast, for a larger I_{nucl}, the curves become virtually indistinguishable.

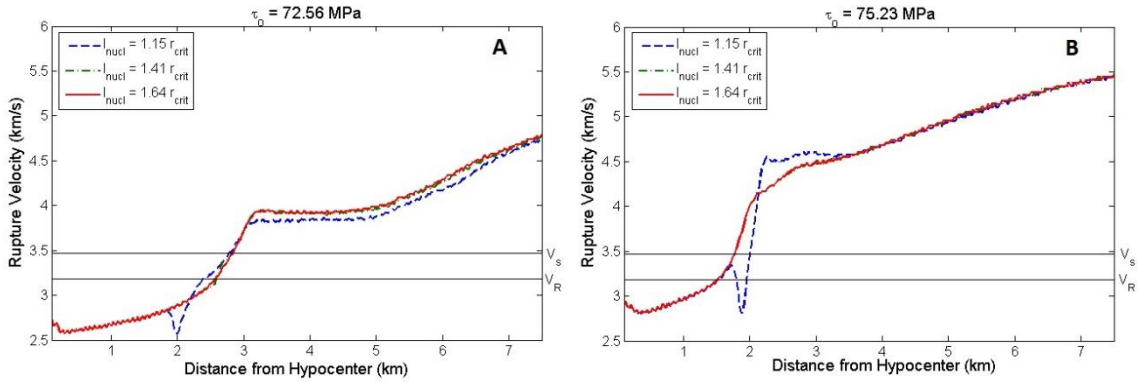

Figure 3.7 Rupture Velocity for experiments with different size initiation patches for an initial stress of $\boldsymbol{\tau_o}$ = 72.56 MPa (A) and $\boldsymbol{\tau_o}$ = 75.23 MPa (B). For an initiation patch larger than 1.414$\boldsymbol{r_c}$, the crack propagates in the same manner regardless of $\boldsymbol{I_{nucl}}$but a patch smaller than this can introduce changes in the rupture velocity.

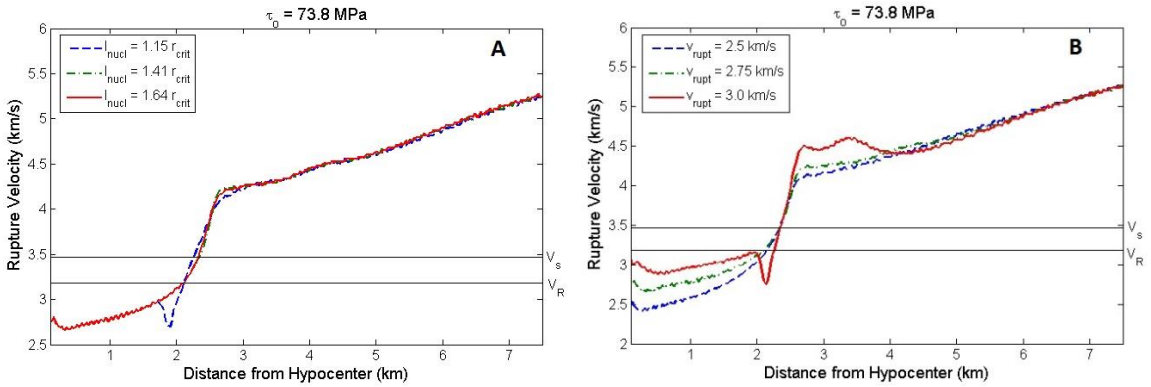

Figure 3.8 Rupture velocity for experiments with different $\boldsymbol{I_{nucl}}$ (A) and $\boldsymbol{v_{rupt}}$ (B). The larger initiation patch has little effect, while forcing the rupture to propagate too fast generated some fluctuations in the rupture evolution.

Similarly, in experiments that varied the speed of the rupture initiation, there were clear differences in the resultant rupture propagation, with the faster v_{rupt} producing the more unsteady propagation with large oscillations in the rupture velocity (Figure 3.8B: runs E, F, G). Since supershear ruptures tend to be insensitive to their origins, the rupture velocities in all experiments with the same initial stress are expected to converge once

they cross the supershear transition (Bizzarri and Das, 2012). Any slight disagreement in rupture velocity towards the end of the fault is likely the result of the shrinking cohesive zone not being adequately captured by the fixed spatial discretization used in our simulations. The variations seen before the rupture has propagated several kilometers down the fault are taken to be the result of the different rupture initiation parameters used.

As shown in Table 3.3 and Figure 3.7 and 3.8, the gradient of the rupture velocity within the forbidden zone is not the same for experiments done with different initiation parameters. Increasing the size of the initiation patch can increase the forbidden zone gradient (e.g. runs A and B), as can increasing the forcing velocity (e.g. runs E, F, and G). What is significant is that these results are generated entirely through an artificial process, yet they mimic the results seen from changing parameters that have definitive physical meaning, such as the initial shear stress. Rupture modelers must be aware that using this procedure can influence the output if the area of study is not far enough down the fault length, or the initiation parameters are too small (I_{nucl}) or too high (v_{rupt}).

3.4 Discussion and Conclusion

Several types of numerical experiments were performed to examine the influence various initial stress levels and rupture initiation states have on the resultant rupture, in particular on rupture behavior within the “forbidden zone”. Experiments done with changing the initial stress on the fault show that faults closer to failure transitioned to supershear speeds sooner and reached a different rupture velocity by the end of the fault.

Specifically, the closer a fault was to failure initially, the sooner it transitioned and the higher the final rupture velocity achieved. Additionally, the stronger faults, i.e., those farthest from failure, had lower velocity gradients within the forbidden zone, while weaker faults had steeper gradients to match the rapidly transitioning velocity.

It was also shown that the common procedure of forcing rupture at a specific velocity within an initiation patch has little effect on the final rupture speed after the rupture becomes supershear, but variations before that transition can be significant, particularly in the forbidden zone of velocities between $[v_r, v_s]$, in agreement with Bizzarri et al., (2010). The size of the nucleation patch can be directly linked to the steepness of the rupture velocity curve through the forbidden zone. The larger the patch, the more rapidly the rupture velocity passes through the forbidden zone and becomes supershear. While the speed at which nucleation is forced has little effect on the final rupture, if it is too high it can also give rise to a steeper rupture velocity gradient within the forbidden zone. It should be recognized that although these changes in rupture initiation are artificial, they can result in the same manifestations in rupture velocity as changing the initial stress.

A possible explanation for both the initial stress and nucleation radius dependencies centers around the supershear transition length, L_{trans} (Andrews, 1976; Das and Aki, 1977; Xia et al., 2004; Dunham, 2007), which is determined physically by the material properties and the stress conditions on the fault and hence is independent of any forced

initiation scheme. Each initial stress value will result in a unique rupture along the fault, i.e., a different supershear transition point, a different velocity gradient and a different final velocity reached on the fault. For the same initial stress condition, a larger initiation patch would force the rupture to travel at an artificial speed for a longer distance and the result is a steeper velocity gradient outside the initiation patch as the rupture acts to preserve the supershear transition point. Similarly, forcing rupture at a too rapid speed, greater than about 2/3rd β, can lead to highly oscillatory propagation as the rupture attempts to reach the transition point at the right time and distance.

One possible result of having a steeper rupture velocity gradient through the forbidden zone for high initial stresses could be an increase in high frequency radiation produced by the fault for those high stress cases. It is well-known that the acceleration of rupture produces radiation (Madariaga, 1983), and while supershear ruptures in general produce more high frequency radiation (Bizzarri and Spudich, 2008; Bizzarri et al., 2010), it is possible that having a difference in the rapid acceleration through the forbidden zone could increase the high frequency content slightly. Our attempts to analyze this in our data have proven inconclusive, likely because the differences in the rupture velocity gradient for our experiments are very slight. If true, measuring the frequency content of a supershear rupture may provide a way to estimate the relative stress on the fault before rupture.

4. INSIGHTS INTO PULVERIZED ROCK FORMATION FROM DYNAMIC RUPTURE MODELS OF EARTHQUAKES*

4.1 Introduction

Recently, pulverized rocks have been found in the damage zones of several large strike-slip faults around the world (Dor et al., 2006; Mitchell et al., 2011; Rempe et al., 2013). Such rocks are extremely friable, incohesive, and marked by severe fracturing down to the micron scale (Mitchell et al., 2011). However, pulverized rocks appear intact and maintain their crystal structure. They usually do not show a preferred fracture orientation and record a low amount of total strain as well as little evidence of shearing or chemical alteration. This suggests that the damage was not achieved by macroscopic compressional shearing, as might be expected inside a fault zone, but instead by a tensional force that "shattered" the rock in place.

Additional observations have found that pulverized rocks form in highly asymmetric distributions. Dor et al. (2008) studied pulverized rock along the Mojave section of the San Andreas fault, finding that 70% of pulverized outcrops were on the side of the fault with faster seismic velocity at depth. Outcrops were found as far as 100 meters away from the fault core. Similarly, Mitchell et al. (2011) found a 200m wide zone of

* Reprinted with permission from Oxford University Press, "Insights into pulverized rock formation from dynamic rupture models of earthquakes" by R.M. Payne and B. Duan, 2017. *Geophysical Journal International,* 208, 517-723, Copyright 2016 by R.M. Payne and B. Duan.

pulverized rock on the stiffer (granitic) side of the Arima-Takazuki Tectonic Line in Japan, and only a 3m wide zone on the opposite (rhyolitic) side.

While it is still not known how pulverized rocks are formed, a couple of mechanisms that may create this damage have been proposed. The first, which we denote as the dynamic unloading mechanism, involves a lessening of the normal stress at the rupture tip as rupture propagates along a bimaterial interface (Brune, 2001; Weertmen, 2002; Ben-Zion and Shi, 2005; Dor et al., 2006). This decrease in confining stress simulates the rapid unloading of stress experienced during mining excavations and produces a tensional wave that fractures the rock in an event similar to a rock-burst.

A second possible mechanism of pulverization involves very rapid strain rates. Laboratory experiments by Yuan et al. (2011) and Doan and d'Hour (2012) using a Split Hopkinson Pressure Bar measured the stresses and strain rates needed to pulverize rock samples. The later paper also proposed a theoretical formulation for pulverization that coincides with their results. Termed “dynamic fragmentation”, the theoretical formulation was initially developed by engineers for failure in ceramics and other brittle solids when impacted at high velocities (Denoual and Hild, 2000,2002; Hild et al., 2003a,b). A similarly rapid deformation is believed to result in pulverized rocks. At such high loading rates multiple fractures can propagate simultaneously before any appreciable stress is relieved. For rapid enough rates, these multiple open fractures will completely break the rock into fragments without shearing, just as is seen in pulverized

rocks. One possible way to generate such high strain rates is from supershear ruptures (Yuan et al., 2011). When a rupture travels faster than the shear wave speed, shock waves form fronts across which there are large changes in strain rate over a very small spatial area. These shock waves also extend away from the fault for a significant distance without attenuation.

Many questions remains about dynamic unloading and dynamic fragmentation. Most importantly, which of the two mechanisms operates during natural earthquakes to produce the pulverized rock observed in the field? The dynamic unloading mechanism seems to make intuitive sense, but how does the reduction in normal stress on the fault affect normal stress changes tens to hundreds meters off the fault? Will all ruptures on bimaterial interfaces be capable of producing pulverized rocks? Can the high strain rates required for pulverization by the dynamic fragmentation be achieved tens to hundreds meters away from the fault? And how well do impact-loading experiments simulate what rock near a fault experiences from a passing rupture?

While little numerical modeling has been done on this problem, simulations offer one way that these questions may be answered. Dynamic rupture simulations are capable of replicating the conditions needed for pulverized rock formation and may reveal unique markers that can be used in the field to indicate the formation mechanism. As the first study to look specifically at pulverized rocks using dynamic rupture modeling, we have determined which types of earthquakes produce damage that is consistent with current

observations of pulverized rock. In light of these new constraints, we evaluate the mechanisms responsible for rock pulverization.

4.2 Method

Pulverized rock has been found along the San Andreas fault, the Northern Anatolian fault, and the Arima-Takazuki Tectonic Line in Japan (Dor et al., 2006,2008; Rockwell et al., 2009; Mitchell et al., 2011; Remp et al., 2013), each of which is a nearly-vertical strike slip fault. The pulverized rock has been predominantly on one side of the fault, the side with the higher seismic velocity and the stiffer material (Dor et al., 2008; Mitchell et al., 2011), and extends out several hundred meters away from the fault. Due to the prevalence of opening-mode fractures and the lack of strain, it is believed that a significant tensional stress was impulsively applied to cause such damage.

Following these observations, we aim to simulate naturally occurring earthquakes on faults similar to those where pulverized rock has been found and compare the likely damage pattern produced to the observations. In order to model these earthquakes, we use the finite element code EQDyna (Duan and Oglesby, 2006; Duan, 2010, 2012) to simulate 3-D spontaneous dynamic rupture and wave propagation in the medium on multi-core cluster systems. The code numerically solves the equation of motion with the traction-at-split node (TSN) method to characterize the fault boundary, adopting the formation given by Day et al. (2005), which provides a consistent treatment for fault behavior (at a given pair of split nodes) at all times, including prerupture, initial rupture, arrest of sliding, and possible reactivation and arrest of sliding.

Fault frictional properties obey a linear slip-weakening friction law (Ida, 1972; Day, 1982), expressed as $\mu(\delta) = \mu_s - (\mu_s - \mu_d)\min(\delta, d_0)/d_0$, where μ_s, μ_d, δ, d_0 are the static and dynamic coefficients of friction, the slip on the fault and the critical slip distance, respectively. Rupture is initiated artificially within a nucleation patch with radius I_{nucl} by forcing the rupture to grow at a fixed speed, v_{force}. Outside of the nucleation zone, ruptures propagate spontaneously and the rupture speed forms part of the dynamic solution. Uniformly spaced square elements discretize the fault with Δx spacing between nodes. The fault is surrounded by a larger buffer region with gradually increasing element size to prevent contamination via boundary reflections. The code has been verified extensively with the Southern California Earthquake Center (SCEC) code validation exercises (Harris et al., 2009), and has been parallelized using a hybrid MPI/ OpenMP scheme so that it can run on modern cluster systems (Wu et al., 2011; Duan, 2012).

We consider a planar, vertical fault that separates two isotropic, linearly elastic media, each having a typical rock density of 2670 kg/m^3. The fault extends to a distance of 70 km in the x_1 (strike) direction and down a distance of 15 km in the x_3 (dip) direction (Figure 4.1). The fault is located at 0 km in the x_2 direction, with numbers increasing to the left.

The focus of this study is on the stress changes off the fault induced by a rupture event. As such, the medium has no initial stress off the fault. An initial shear stress that is

parallel to the x_1 direction is assigned only on the fault plane, ensuring that subsequent rupture is strike-slip. Both the initial normal stress and the initial shear stress on the fault plane are depth-dependent according to

$$\sigma_n = -16 * z \tag{4.1}$$

$$\tau_o = \alpha * |\sigma_n| \tag{4.2}$$

where z is the distance down-dip in km (along x_3 axis), σ_n and τ_o are the normal and shear stress, respectively, in MPa, and α is a constant less than one.

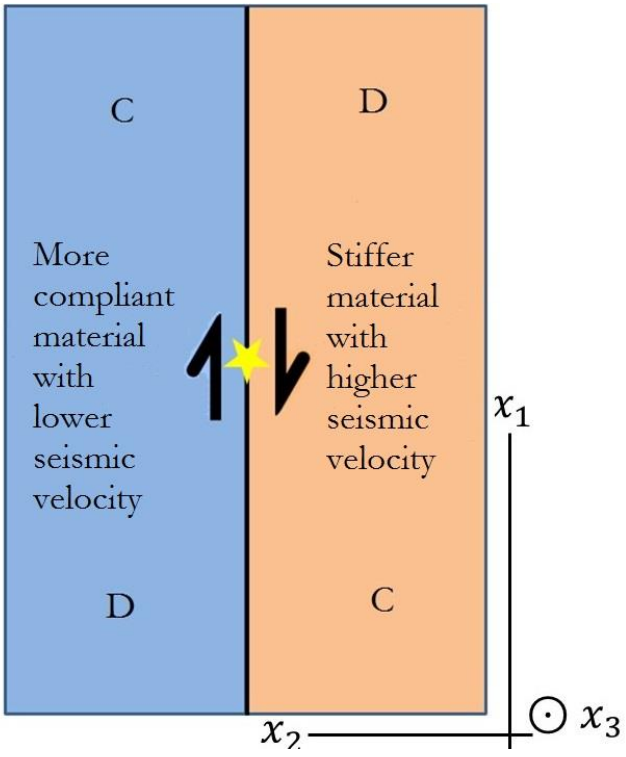

Figure 4.1 Map view of fault geometry. Compressional and Dilatational quadrants marked for a right lateral fault. Rupture begins in the center of the fault and propagates bilaterally.

To produce a slip distribution with significant shallow slip, similar to those determined for the Landers 1992 and Hector Mine 1999 earthquakes (Cohee and Beroza, 1994; Jónsson et al., 2002), albeit grossly simplified, the dynamic friction coefficient is allowed to vary with depth:

If $z \leq 5$ $\quad \mu_d = 0.16 + 0.06 * z$

If $5 < z \leq 7.5$ $\quad \mu_d = 0.46$

If $z > 7.5$ $\quad \mu_d = 0.46 + 0.01 * (z - 7.5)$

where z is the depth in km and μ_d is the dynamic friction coefficient. The static coefficient of friction is held to be 0.677 while the initial shear stress is computed with $\alpha = 0.55$ and $\alpha = 0.605$ for subshear and supershear simulations, respectively.

We report four main simulations. The first is a baseline run along a fault embedded in a uniform medium at subshear rupture speed, followed by a similar simulation along a bimaterial fault separating two different materials. The material contrast for the bimaterial runs is set at 20%, meaning the seismic velocity, v_P and v_s, was decreased by 20% on the left side of the fault, from 6000 m/s to 5000 m/s and from 3464 m/s to 2887 m/s, respectively. Figure 1 shows a map view of this geometry. Another simulation with a uniform material on both sides of the fault was then run, this time with a higher initial stress to prompt a transition to supershear rupture speeds. Finally, a supershear rupture along a bimaterial fault was simulated.

Each of the dynamic simulations presented have a spatial discretization, Δx, of 100 meters and contain about 2 million elements. The time step was $5\ x\ 10^{-3}$ seconds. Simulations were run until the rupture travelled down most of the fault (around 30 km of propagation) and were then halted to avoid any rupture termination or fault edge effects. Specifically this was a termination time of 9.9 seconds for the subshear ruptures and 6.9 seconds for the supershear ruptures.

Unlike most dynamic rupture models, our interests were not focused on the fault plane itself. Instead, to study rock pulverization, output was generated along either side of the fault out to a perpendicular distance of 500 meters, and extending 1 kilometers below the surface. EQDyna tracks the stress evolution of every element along with the strain rate in that element for the entire simulation. Due to memory constraints, these element values were only output every 0.075 seconds during the simulation to generate a time history of stress in the off-fault rock. Concurrently, the normal and shear stress on the fault plane, along with the slip and slip rate on the fault are output to provide a means of comparison between the off-fault stresses and the on-fault behavior.

To determine areas of possible pulverization, a theoretical threshold for pulverization was established. If the mean stress in an element was larger than 10 MPa in tension, the rock body was presumed to have failed. This simple criterion was chosen due to the continued debate over the applicability of other pulverization thresholds, i.e. the

dynamic fragmentation and dynamic unloading theories. The mean stress for each element was calculated at the center of that element according to

$$\sigma_m = (\sigma_{xx} + \sigma_{yy} + \sigma_{zz})/3 \quad (4.3)$$

where σ_{xx}, σ_{yy}, and σ_{zz} are the normal components of stress. Since there is no initial stress off the fault at the start of the simulation, these measurements of mean stress are actually the mean stress variation in the rock body. However since pulverized rocks are generally a near-surface phenomenon, in this study we focus on the dynamic mean stress near the surface where initial stresses are negligible. This is consistent with previously found outcrops on the surface and at shallow depths (Wechsler, 2011). We also note that the mean stress criteria does not capture the shock wave formed by supershear ruptures (the "Mach cone"), which produces large deviatoric stresses and strain rates, not mean stress changes.

Due to the distinct nature of pulverized rock, i.e. the proliferation of opening-mode fractures in them, all major theories of formation agree that pulverized rocks must be formed under microscopic tension. This tension can either be the result of applying macroscopic tension, such as is produced in extensional quadrants during an earthquake, or result from macroscopic compression, as is seen when an impact produces a tensile wave through a material. In either case, the microscopic tensile stress forms the opening mode fractures that are indicative of pulverization. However, we prefer macroscopic tension to macroscopic compression in part because the exact relation between the

macroscopic compressional stress being applied and the microscopic tensile stress being induced is uncertain. In addition, as we show below in our modeling results, the high strain rates and stresses required for pulverization from impact laboratory experiments, i.e. macroscopic compression experiments, are not reached anywhere along the fault at distances where pulverized rocks are observed in the field.

In order to contextualize our results, a threshold of 10 MPa was chosen largely based on tensile strength measurements of rock in the laboratory (Li et al., 2013; Perras and Diederichs, 2014). It is well known that rock is generally much weaker in tension than compression. As shown by Li et al. (2013) and reviewed by Perras and Diederichs (2014), the direct tensile strength of most rocks is about 5-10 MPa. Although the failure mode in these experiments was dominated by a single tensile crack, we assume these threshold values are applicable to pulverization given the lack of experimental constraint on the tensile strength for pulverized rocks. Nevertheless, the 10 MPa threshold should not be considered a rigorous value. Rather, it is a reasonable value that allows us to explore which type of earthquakes will most likely generate pulverized rocks, as shown below.

4.3 Results

Figures 4.2 and 4.3 show the regions off the fault where the mean stress in each element exceeds the tensional stress threshold for earthquakes in a uniform medium and for earthquakes along a fault separating two different materials, respectively. The fault is located at 0 km, right in the center of the horizontal axis, and the plot is in “map view”,

looking down from above. Each plot only shows the stress in the uppermost elements - in this case 50m below the surface- but extends out to 500m on either side of the fault. If exceeding the threshold is taken to indicate that pulverization is likely in that area, then these figures show the spatial distribution of pulverization expected from that particular earthquake simulation.

The results for a uniform medium are shown in Figure 4.2. For the subshear case, the threshold is exceeded near the ends of the fault in the dilatational quadrants up to 150m away from the fault. The damage is symmetric around the fault due to the uniform material. In the case of a supershear rupture, the damage is again symmetric, but now extends out for several hundred meters. There is also a region of high stresses near the center of the fault where the threshold is exceeded. This is likely due to the transition to supershear rupture speeds. In both uniform cases, the majority of damage is expected close to the fault, with a significant reduction in damage only 100m off the fault.

For the bimaterial runs, there are even clearer differences (Figure 4.3). The subshear case meets the threshold easily in the dilatational quadrant on the stiff side of the fault and the damage extends out to 450m, but in a decreasing area. The supershear case inverts the damage distribution, with the majority of damage now in the extensional quadrant of the more compliant material. The damage here extends for several hundred meters away from the fault. Both cases are asymmetric.

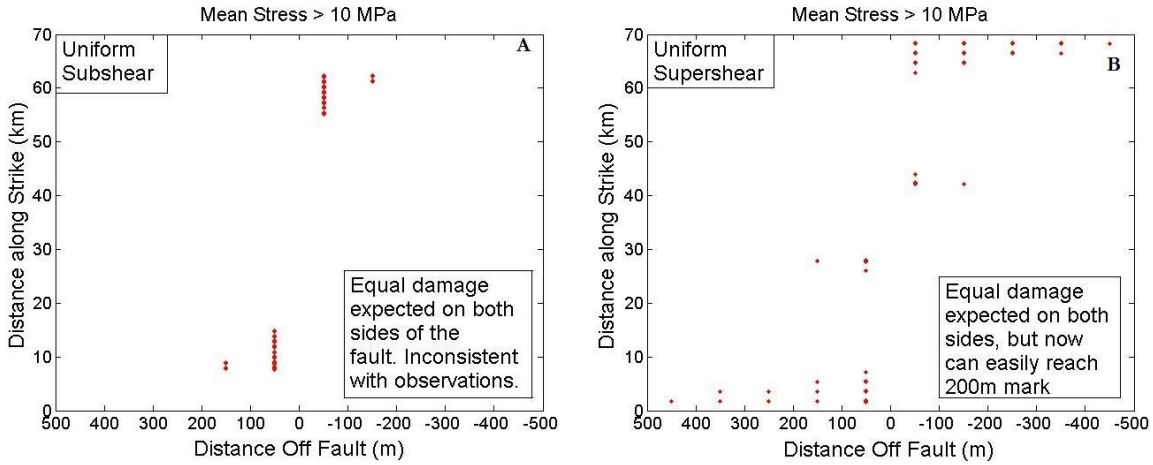

Figure 4.2 Simulations in a uniform medium, with subshear rupture propagation (A) and supershear rupture propagation (B). Off-fault points where the mean stress reached the 10 MPa threshold are marked with red dots.

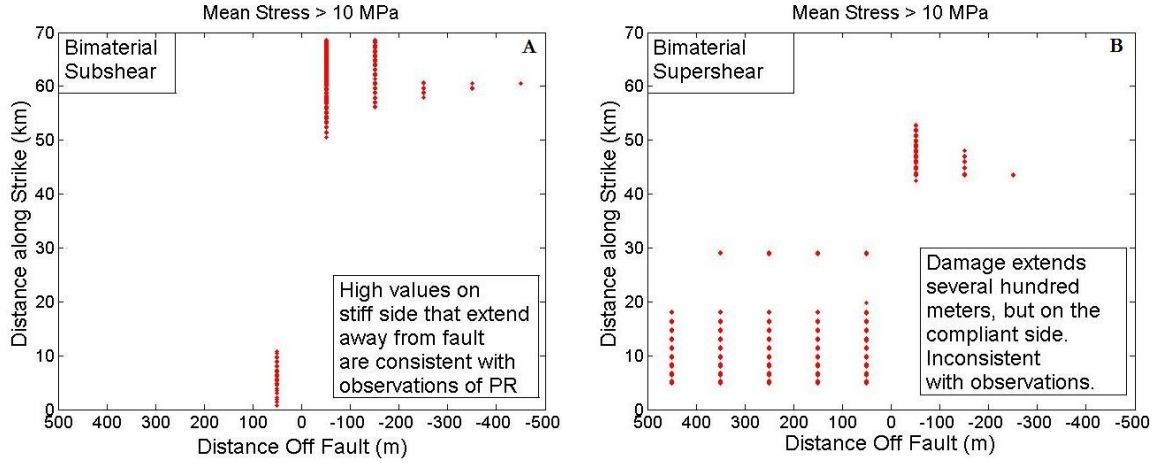

Figure 4.3 Simulations in a bimaterial medium, with 20% contrast in the seismic velocity between each side. Off-fault points where the mean stress reached the 10 MPa threshold are marked with red dots. The subshear rupture propagation (A) is the simulation most consistent with observed pulverized rock distributions.

Another way to compare the two bimaterial simulations is presented in Figure 4.4. This figure shows the maximum mean stress values achieved at every distance along strike for each simulation. Here, the stress is positive in tension and the largest tensile stresses

are naturally in the extensional quadrant. These values are for 50m off the fault and only on the stiffer side, where pulverization is observed in the field. It is clear that both simulations go above the 10 MPa limit, but the subshear simulation remains above the threshold until the end of the fault. The supershear case is only above the threshold along the section of the fault where the rupture transitions to supershear speeds. The stress drops once the rupture transition is complete.

Figure 4.5 is similar to Figure 4.4 except that it shows the maximum mean strain rate at every distance along strike, again on the stiff side and 50m off the fault. The supershear simulation achieves its highest strain rates during the supershear transition, before falling back below $1\ x\ 10^{-1}\ s^{-1}$. The subshear case shows consistently high strain rates as the rupture propagates in the positive direction. Most notable about this figure is the magnitude of the strain rate, which reaches about $2\ x\ 10^{-3}\ \ s^{-1}$ at most for either simulation. While some higher strain rates (around $4\ x\ 10^{-3}\ s^{-1}$) are measured in the supershear simulation, those occur in the more compliant material, opposite where pulverization has been observed.

To understand the stress state in an area that may experience pulverization, a time series of the mean stress in a single off-fault element is shown in Figure 4.6. This particular stress evolution represents the element that had the largest stress pulse in the bimaterial subshear simulation, although the general features are common to all cases. The stress is

initially zero at this location, 50m off the fault and at the surface, but as the rupture approaches the stress becomes compressive before suddenly expanding out rapidly.

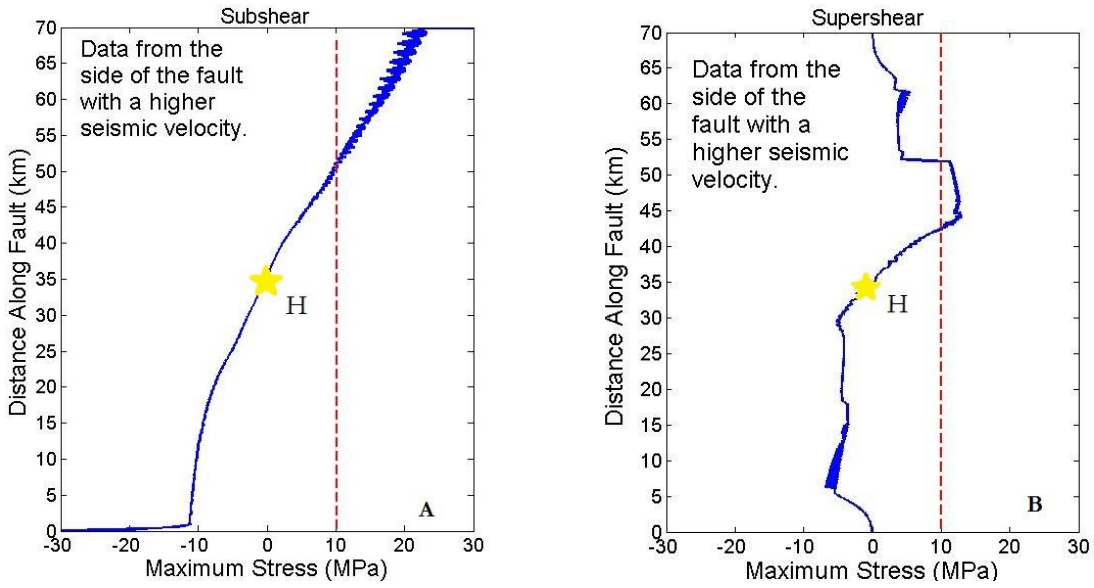

Figure 4.4 Maximum mean stress values measured at every distance along strike, 50 meters from the fault plane, on the stiffer side of the fault. The earthquake begins at 35 km along strike and propagates bilaterally until the end of the fault. Dashed line marks the tensile threshold.

Measurements for this figure were reported every 0.075 s, which means that the mean stress changed at a peak rate of over 150 MPa/s. Every element that exceeded the threshold shows a similar time evolution, with a large stress peak - tensile or compressive depending on the quadrant- that developed over the 0.3-0.6 second window corresponding to the time of rupture passage. However, only the bimaterial runs exhibit the compression-to-tension transition shown in Figure 4.6.

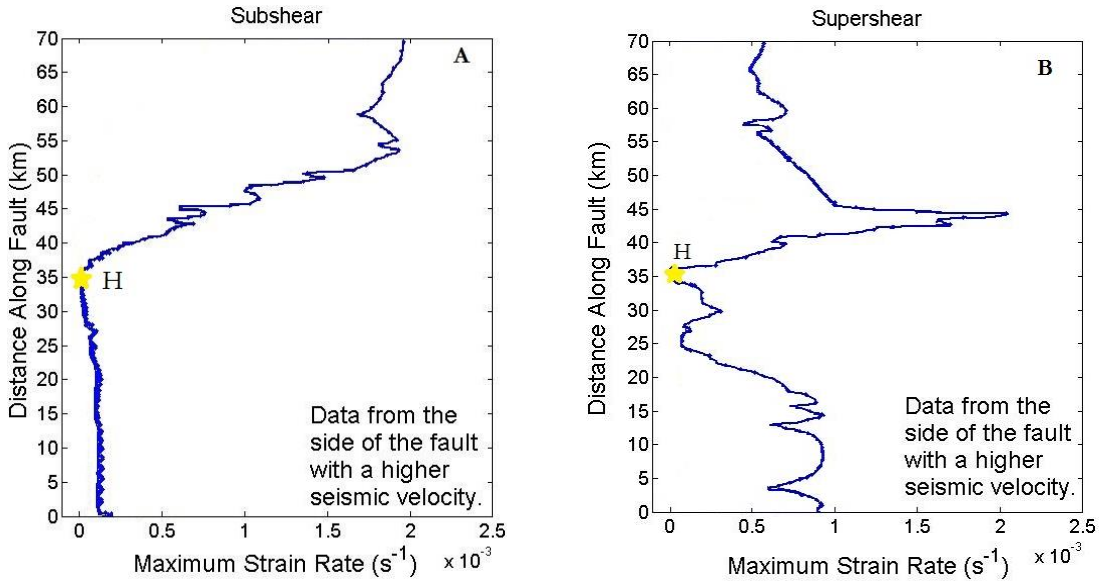

Figure 4.5 Maximum mean strain rate values measured at every distance along strike, 50 meters from the fault plane, on the stiffer side of the fault. The earthquake begins at 35 km along strike and propagates bilaterally until the end of the fault.

Several bimaterial subshear simulations were also run with smaller element sizes (Δx = 500m, 200m, 100m, 50m, and 25m) in order to produce Figure 4.7. This figure includes the maximum mean stress and the maximum mean strain rates measured at different distances from the fault on the stiff side. A trendline indicates how this data is expected to change for closer (sub-meter) distances. Unsurprisingly, both stress and strain rate increase significantly as you move closer to the fault.

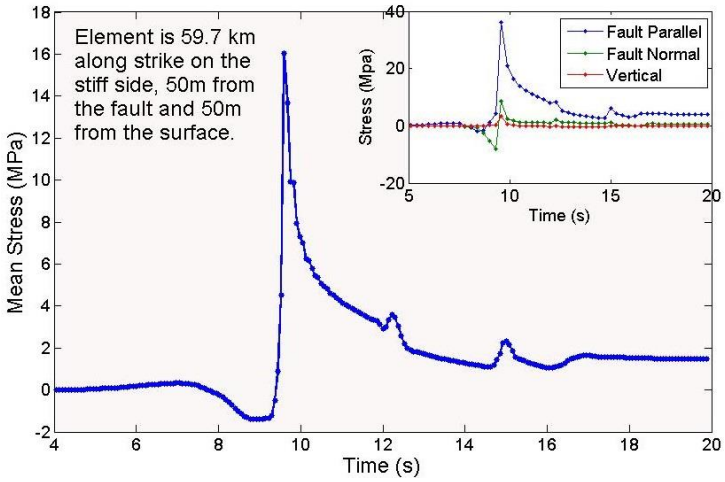

Figure 4.6 Mean stress variation in a single element over the course of the simulation. This is from the bimaterial subshear run, where the mean stress suddenly changes from around 1.5 MPa in compression to over 16 MPa in tension. (Inset) The stress components show the sudden tensile pulse occurs in all three directions. While the fault-parallel direction is the largest, there is also a strong fault-normal change of approximately 16 MPa.

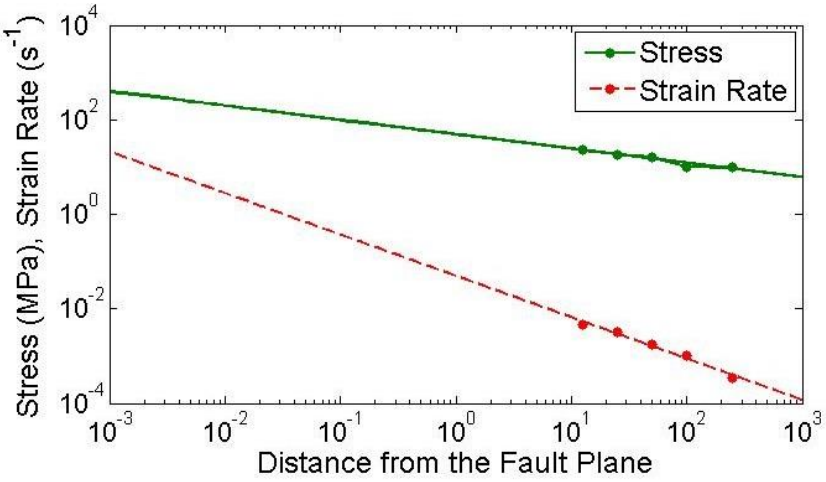

Figure 4. 7 Maximum mean stress and maximum strain rate measured at each distance from the fault. Data is from bimaterial subshear simulations, in the material with a higher seismic velocity. Trendlines extend the data to estimate values in the sub-meter range.

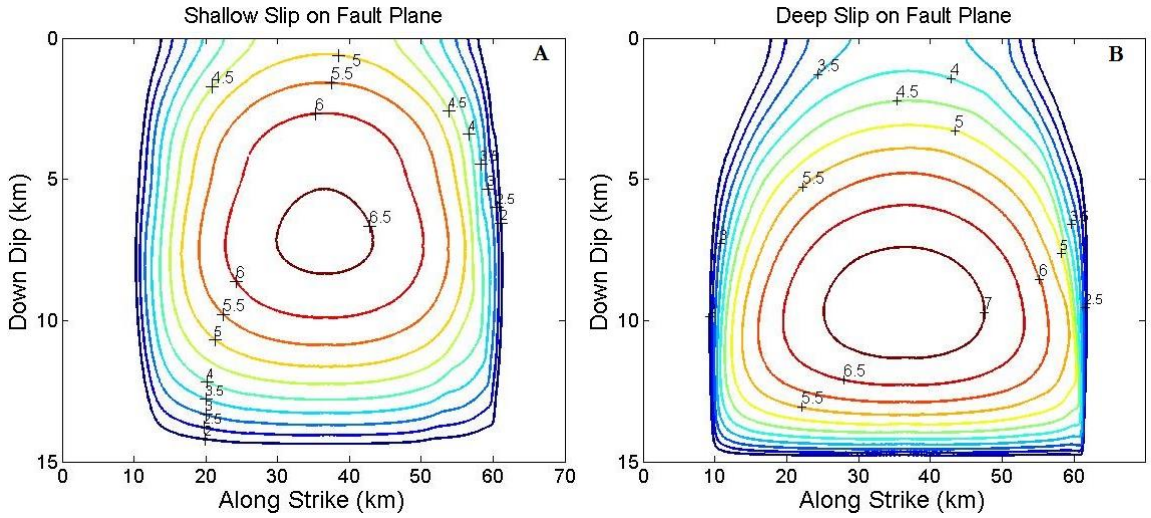

Figure 4.8 Shallow (A) and Deep (B) slip distributions. Large crustal earthquakes produce more complicated slip distributions than these simulations (Cohee and Beroza, 1994; Jónsson et al. 2002), however, the natural events indicate mostly shallow slip. Simulations with more slip near the surface exceeded the pulverization threshold more readily.

A final aspect of this study involved altering the earthquake magnitude and slip distribution to determine the types of events needed to reach the imposed threshold. A magnitude of at least Mw = 7.1 was needed to produce a mean stress variation larger than the pulverization threshold. Smaller earthquakes could not produce a tensile stress larger than 10 MPa anywhere off the fault plane near the surface. Similarly, earthquakes that met the threshold exhibited “shallow slip”, meaning that a significant amount of slip occurred near the surface, generally greater than four meters with the majority of slip concentrated between 6-8 kilometers down dip (Figure 4.8a). A “deep slip” earthquake instead has less than 4 meters of slip at the surface and the majority of slip on the fault occurs around 10km down dip (Figure 4.8b). Intuitively, when more slip is near the surface it is easier to meet the threshold and cause pulverization. Even larger magnitude

earthquakes, above Mw 7.5, were not able to meet the threshold if there was not significant shallow slip. We remark that all the simulated earthquakes were characterized by a compact source dimension and a high stress drop in these simplified models. It remains to be seen if events with low stress drops that have distributed slip near the surface would meet any pulverization threshold.

4.4 Discussion

Based on several features of pulverized rock observations in the field, the results of our simulations indicate that a subshear earthquake along a bimaterial fault is the most likely cause of the observed damage. Even more specifically, it takes a large earthquake of at least Mw 7.1 with significant slip (several meters) at the surface to best match the damage seen in field studies, particularly the highly asymmetric distribution with most damage on the side of the fault with higher seismic velocity.

It is important to clarify that each large shallow earthquake simulated produced a mean stress above 10 MPa in at least some areas (Figures 4.2 and 4.3). Theoretically, this means that every type of earthquake has the potential to produce pulverized rock. However, when you compare the distributions of pulverized rock seen in the field with the distributions produced by our model, only the bimaterial subshear case produces comparable results. We take this as an indication that bimaterial subshear ruptures are the most likely cause of pulverization.

However, this does not clarify the exact mechanism by which pulverization occurs. Fortunately, the stress and strain rate values obtained can be compared with prior theoretical explanations of the pulverization mechanism in the same way that field observations were used to compare the spatial distribution of damage with our model. One of the major mechanisms of pulverization, advanced by Doan and d'Hour (2012), is based on a statistical theory of the brittle strength of materials developed for studying impact damage in ceramics (Denoual and Hild, 2000; Denoual, 2002; Hild, 2003). Essentially, a slowly loaded material will fail along a few major fractures, but if loading is much more rapid, the physics is altered so that multiple fractures can propagate simultaneously. Rapid strain rates result in "dynamic fragmentation" which produces damage similar to a pulverized rock, including very small grain size and no preferred fracture orientation.

Two groups of experiments by Doan and d'Hour (2012) and Yuan et al. (2011) used split Hopkinson pressure bars to produce pulverized rock experimentally in the laboratory and measure the strain rates needed to cause such damage. Both papers agree that strain rates of at least 250 s^{-1} are needed to cause pulverization of intact rock. Doan and d'Hour (2012) also investigated the effect of predamage on this threshold and found that it is lower (near 150 s^{-1}) if the rock is already damaged. They explain their values using the dynamic fragmentation theory, eventually deriving the transition stress rate (simplified from their equation 21),

$$\dot{\sigma_c} = C\Delta\sigma c\, V^{-\frac{1}{n}} \tag{4.4}$$

where C is a constant dependent on the dimension, initial defect distribution, and other physical properties, $\Delta\sigma$ is the ultimate strength, c is the elastic wave speed, n is the dimensionality, and V is the volume of the sample.

Assuming the critical stress rate is directly related to the critical strain rate, both the Doan and d'Hour (2012) and Yuan et al. (2011) results match this relation quite well. This seems to indicate that either those experiments produce tensional damage when they pulverize the rock or that the details of tension/compression are not as important as the very high strain rate. That is, rapid tensile stresses and rapid compressional stresses both drive dynamic fragmentation to the same end state. For this reason, even though the macroscopic tension measured off the fault in our simulations is not an exact analogue of the split Hopkinson pressure bar experiments, we believe a comparison of strain rates produced is useful.

However, to make this comparison we must take into account the volumetric difference between our element size and their sample size. They used cylindrical samples, 2.5cm long and with a 2.5cm diameter, which corresponds to $V^{-\frac{1}{3}} = 43.36\ m^{-1}$. We assume that our element size of 100m delineates a characteristic rock volume below which heterogeneity (i.e. initial flaws) cannot be resolved. The corresponding volume term

would then be $V^{-\frac{1}{3}}$ = 0.0068 m^{-1}, which is 6376 times smaller than the lab experiment. Due to the direct relation between $V^{-\frac{1}{3}}$and $\dot{\sigma}$ in equation 4.4, the strain rate threshold from our simulations should also be smaller by the same amount. This results in a transition strain rate of roughly 0.04 s^{-1} for our simulations. However, the maximum mean strain rate measured 50 meters off the fault was only 0.002 s^{-1}, an order of magnitude lower (Figure 4.5).

Figure 4.5 shows that this level of strain rate is not met by either bimaterial simulation on the stiff side of the fault. However, Figure 4.7 shows that higher strain rates can be produced closer to the fault. By using the trendline in Figure 4.7, we can determine that the threshold strain rate of 0.04 s^{-1} will be met around 1 meter off the fault for a subshear rupture along a bimaterial interface. Closer than 1m, a large earthquake will produce strain rates high enough to cause pulverization via dynamic fragmentation. However, the maximum strain rate values are not large enough to cause pulverization tens to hundreds meters away from the fault, where pulverized rocks are observed in the field.

Experimental studies have also measured the peak strength of pulverized samples, which typically falls somewhere between 150-200 MPa (Yuan et al., 2011; Doan & d'Hour, 2012; Aben et al., 2016). Figure 4.4 shows that nowhere along strike is this high level of stress present, either in tension or compression. Again though, following the trend in

Figure 4.7, the bimaterial subshear simulation should produce this level of stress closer than 2 cm from the fault.

These results suggest that dynamic fragmentation may cause pulverization close to the fault, but more is needed to explain how pulverization reaches distances of 100m off the fault. Additionally, there are some difficulties with the details of the dynamic fragmentation theory. While our 3D dynamic model includes our basic understanding of earthquake source physics, 3D model geometry and the free surface, these are not able to be captured from the laboratory experiments used to validate the dynamic fragmentation theory. Therefore the exact threshold values may not be entirely accurate.

Moreover, the theory relies on the assumption that the stress rate is constant. Our modeling results show that for an earthquake rupture, there are sharp changes in the stress (Fig. 4.6) and strain rate, which indicates that the stress rate changes over time. Most importantly, our results show that there are strong volumetric tensile stresses and lower strain rates and compressional stresses than suggested by the theory. Therefore, it is very likely that impact experiments, with strongly one-dimensional loading, are not a faithful analogue for what occurs in a rock body during an earthquake and that the threshold may not be applicable to pulverized rock formation in natural earthquakes. However, the mechanism of dynamic fragmentation, where rapid loading drives multiple fractures, is still appropriate given the high values obtained (10 MPa and $2\ x\ 10^{-3}\ s^{-1}$).

Another mechanism suggested by Dor et al. (2006) is that the large tensile stresses generated from rupture along a bimaterial interface cause pulverization. This mechanism is qualitatively consistent with our modeling results, as we see large tensile stresses where pulverized rocks are expected for the bimaterial simulations. However, as our results show, not all ruptures on bimaterial interfaces are capable of producing pulverized rocks that are consistent with field observations. Rather, it is only subshear ruptures on bimaterial interfaces that match observations.

Our results show that dynamic unloading produces large tensile stresses hundreds of meters off the fault in the subshear case (Figure 4.3a). These stresses expand the rock in all directions simultaneously (Figure 4.6, inset). This is a rapid volumetric expansion that coincides with the rupture passage. What makes the bimaterial case particularly effective is the fault-normal expansion, where the elements off the fault are first compressed before being stretched. While the fault-normal component is typically what dynamic unloading is concerned with, our results show a tensile stress in the other directions as well. Combined, this produces a stress state that is more than capable of damaging a rock body.

At the same time, stresses and strain rates are expected close to the fault that are comparable to those needed for dynamic fragmentation. A union of these two mechanisms seems to be a natural explanation for PR formation. Rupture along a bimaterial interface causes dynamic unloading which produces rapid strain rates and

high mean stresses which expand the material in every direction simultaneously. Such a tensile stress state is so large and is applied so rapidly that multiple fractures grow in all directions and pulverizes the rock closest to the fault, at the sub-meter scale. Farther away, particularly everywhere our threshold is met, the rock is also damaged by the large tensile stresses, laying the groundwork for future pulverization.

The subshear nature of the rupture indicates that pulverization is a multi-stage or repeated process. Every area that is damaged by the first rupture is then at risk for pulverization by later events. Repeated earthquakes over time work to create and extend the pulverized zone, from a sub-meter scale to tens and eventually hundreds of meters off the fault. This implies a relationship between fault age and PR zone width, where the most mature faults should have the widest pulverized zones. The relative frequency of subshear ruptures along bimaterial interfaces, even those larger than Mw 7.1, also suggests that PR should be more common than has been seen so far, or that the pulverization mechanism is missing important aspects.

The ideas presented here agree with the well-reasoned conceptual model described by Aben et al. (2016), with one important modification. Their general model describes how an earthquake pulverizes the rock nearest the fault first and then expands the pulverized region outward with every successive event. They use laboratory experiments to derive thresholds for pulverization and suggest several rupture scenarios that may produce pulverization, such as subshear ruptures along a uniform fault, supershear ruptures, and

ruptures along a bimaterial interface. Our modification is that instead of the high compressive stress and strain rate, the material is subjected to tensile stresses caused by the rupture passage. As rocks are much weaker in tension, tensile loading is likely to lower the threshold for pulverization. Additionally, this tensile failure is predicated on the dynamic unloading that occurs along a bimaterial interface. We can therefore specify that ruptures along a bimaterial interface are the most likely cause of pulverization.

4.5 Conclusions

A bimaterial subshear earthquake produces damage that is the most consistent with the distributions of pulverized rock found in the field. A supershear earthquake along the same interface did not produce the requisite level of tensile stress, compressive stress, or strain rate during rupture propagation to meet any of these thresholds. The expected distribution of damage from the supershear earthquake also did not match field observations, which suggests that supershear ruptures do not play a significant role in pulverized rock formation.

These results were analysed by applying a very simple 10 MPa threshold on the mean stress. Pulverization was assumed to occur in areas where the mean stress went above 10 MPa in tension. The bimaterial subshear rupture produced the highest stresses and the fastest strain rates off the fault, in the extensional quadrant where pulverized rock has been observed. Our results also show that the high laboratory-derived strain rate and stress required for pulverization is not reached at these distances in realistic earthquakes.

Instead, our results suggest that pulverization is the result of volumetric tensile expansion. These tensile stresses are the result of dynamic unloading, where normal stress is relaxed due to subshear rupture along a bimaterial interface. Very close to the fault, this unloading may cause pulverization via dynamic fragmentation. The stress remains high 50-100 meters away from the fault which almost certainly causes damage. With repeated events, the zone of pulverization extends away from the fault plane, eventually producing the tens to hundreds of meter wide zones of fully pulverized rock seen in the field. Future work is needed to determine how far off the fault pulverization can occur due to a single event and how current laboratory-derived thresholds, under compressional conditions, change when tensile stresses are applied.

5. DYNAMIC TRIGGERING OF STRESSED GRANULAR MATERIALS

5.1 Introduction

There have been many observations that seismic waves propagating outward from an earthquake can trigger activity on nearby faults. The first observations of an earthquake triggering events several hundred kilometers away come from the 1992 M_W = 7.2 Landers, CA earthquake (Hill et al., 1993; Gomberg et al., 2001), which sharply increased seismicity throughout the western United States for a period of hours to weeks after the initial event. Subsequent observations, particularly of the 1999 Hector Mine earthquake, also in California, and the 1999 Izmit earthquake in Turkey, further contributed to the acknowledgement that earthquakes had the potential to interact with distant faults in a way that produced more earthquakes. The 2002 M_W = 7.9 Denali, Alaska earthquake triggered seismicity from British Columbia to Mexico (Gomberg et al., 2004; Freed, 2005).

The motion of a fault during an earthquake is known to alter the long-term (static) stress field around a fault. These diminish rapidly with distance from a fault, therefore observations of earthquakes triggered on faults more than several rupture dimensions away are thought to be caused by dynamic stress changes carried by transient seismic waves. Corroborating this, triggered events frequently begin just as the surface wave train passes the triggered fault (Brodsky and van der Elst, 2014). These stress changes are small, typically less than 1 MPa producing strains on the order of 10^{-6} (Gomberg and Davis, 1996; Brodsky and Prejean, 2005), which suggests that triggered faults must be

highly stressed (Johnson and Jia, 2005). Even with these observations, the mechanism of failure is still unknown. A major problem with dynamic triggering is the transient nature of the stress perturbation, where the stress state returns to the initial state once the waves have passed. The expected seismicity would have to occur as the waves pass and the stress state is changed. This immediate triggering is seen, however, the bulk of dynamically triggered seismicity occurs after a delay of seconds to weeks following the original event (Freed, 2005). This implies that the dynamic stresses either change the system, and the failure criteria that must be met, or initiate a secondary mechanism that leads to rupture.

Any understanding of which transients are most likely to trigger a new earthquake on a fault will rely on a more complete understanding of the failure mechanism. For this, we must look at the stability of the slipping surface. The actual slip surface of a fault consists of a narrow, highly-strained zone where most shear takes place (Chester et al., 1993; Chester and Chester, 1998). This fault core is composed of granular material generated by the grinding and wearing of both sides of the fault as they slide past each other. The core is a zone of weakness and represents the portion of the fault where nucleation takes place. As such, interactions between grains in the fault core control the friction of the surface and the ultimate strength of the fault.

Recently, several authors have investigated the effect of dynamic perturbations on stressed granular materials. A common way to study the behavior of fault gouge is

through numerical models that simulate grains in a confined area subject to shear stress, akin to an active fault zone. When the boundary of such a system is vibrated, simulating passing seismic waves, studies have found that slip can be induced in the grains. Such triggering appears to be amplitude dependent, with a threshold below which no appreciable change in the system is detected. Larger amplitude vibrations have been shown to produce larger amplitude slip events, and vibrations typically result in a clock-advance of the slip event (Griffa et al., 2013; Ferdowski et al., 2013), where the natural event occurs earlier than would it would have in the absence of perturbation, in general agreement with natural observations. Others have found a characteristic frequency of oscillation that the external perturbation generates within the granular material (Giacco et al., 2015). These waves spontaneously emerged at the onset of failure, even without the external vibration. This suggests that the behavior inside the granular pack is just as important to failure as properties of the external perturbation.

Several physical laboratory experiments on sheared glass beads subject to boundary vibrations have found that, when the system is near failure, the vibrations result in both immediate and delayed events, as well as a departure from the standard recurrence interval expected from the constant loading rate. The amount of departure is correlated with the amplitude and duration of the boundary vibration applied, and is believed to be due to the nonlinear elastic response of the modelled fault gouge (Johnson and Jia, 2005). Lab experiments indicate that seismic waves alter the frictional properties of the

gouge, and the triggered events reflect a disruption of the internal fault zone structure (Johnson et al., 2008).

Both numerical and laboratory models have been unable to identify the exact alteration of the fault gouge that takes place when the system is dynamically stressed. However an alteration of the gouge is the obvious explanation for the observed time delay between passing seismic waves and triggered events. This work studies the consequences of such dynamic stress changes in a granular system after a simplified normal stress perturbation is applied. Perturbations are in the form of a single wavelet pulse, not a wave train, input at a single frequency, allowing us to focus on the behavior leading to failure under the simplest dynamic stressing conditions. By studying the nature of the failure, it gives us a deeper understanding of how seismic activity may be triggered.

5.2 Method

5.2.1 Discrete Element Model

We use a two-dimensional Discrete Element Method (DEM) code to track the motions of and the forces on each particle in the simulation over a stick-slip cycle. The DEM code creates a periodic layer of circular grains to fill an area between two rough rigid walls made of glued grains. The grain diameters are generated randomly from a clipped Gaussian distribution around the average grain diameter. In this model, distance, velocity, stresses, and time all scale with the chosen size of the average grain and the elastic properties of the grains. For the purposes of giving dimensional values to the experiments, all values are calculated assuming 1 millimeter quartz grains (Young's

Modulus of 80 GPa). A normal stress to the top wall, N_o, is applied to the system to tightly pack the grains. Here the normal stress is set to 80 MPa, corresponding to several kilometers beneath the surface.

The system is loaded in shear by pulling a spring attached to the top wall of the box at a constant wall-parallel velocity, simulating shear loading via tectonic forces (Figure 5.1). When the shear force, *F*, reaches a critical value, the wall slips, the grains rearrange themselves through a combination of rolling and frictional sliding into a new packing, and the load cycle begins again. The stress ratio, F/N_o, at which failure occurs during slow loading is referred to as the strength of the system, *S*. This can be thought of as a static friction coefficient. The strength is an emergent quantity that depends on the exact packing. The strength of the packings studied here ranges between [0.22 - 0.28], generally averaging 0.24. This means that the packings can withstand shear forces up to a quarter the size of the normal stress before slipping. These values are characteristic of 2-D circular grain models (Morgan, 1999; Mora and Place, 1999)

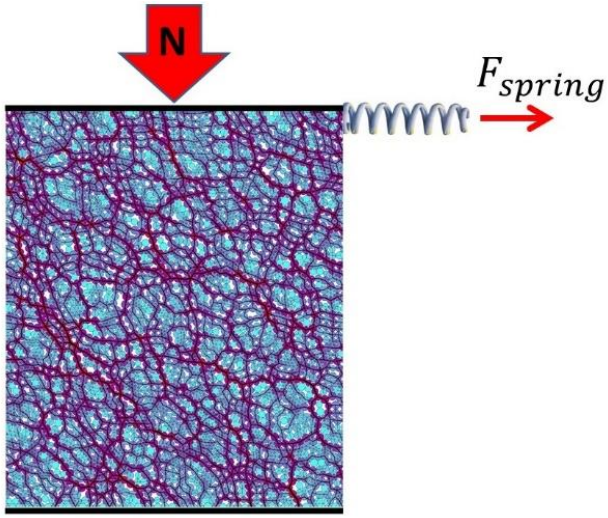

Figure 5.1 Schematic of the granular code. Grains are compressed in a box under an external normal force N, while the top wall of the packing is stressed under the force of a loaded spring, F. Grains are colored according to how much stress they experience, with warm colors indicating higher stresses. Stress chains are also visible through the granular packing at an angle due to the shear force on the top wall.

The code is similar to that used in Aharonov and Sparks (2002), (2004). The model is two dimensional and the force of gravity is ignored. Individual grains are simulated as inelastic spheres, free to rotate and slide, and are incohesive. When two grains overlap, that is, when the distance between the centers of grain *i* and grain *j*, termed r_{ij}, is less than the sum of the radii, $R_i + R_j$, an interaction force is exerted on each grain at the point of contact. The normal interaction force is depends on the very small amount of overlap between grains, $R_i + R_j - r_{ij}$, and is expressed as:

$$F_{ij}^{n}(t) = \left[k_n\left(R_i + R_j - r_{ij}\right) - \gamma m_{ij}(\dot{r_{ij}} \cdot \hat{n})\right]\hat{n} \tag{5.1}$$

where $\hat{n} = \left(\boldsymbol{r_{ij}} \cdot \hat{\boldsymbol{x}}, \boldsymbol{r_{ij}} \cdot \hat{\boldsymbol{y}}\right)/\boldsymbol{r_{ij}}$, the unit vector normal to the surface. The normal force exerted by the contact consists of a linear repulsive force, the first term in equation 5.1,

as well as a damping force that depends on the relative grain velocities, $\dot{r}_{ij}$. Here, k_n is the normal spring stiffness, γ is the damping coefficient and m_{ij} is the harmonic mean of the two grain masses.

The shear force on the contact is determined using an elastic friction law (Cundall and Strack, 1979)

$$F_{ij}^{s}(t) = -[\min(k_s \Delta s, \mu(F \cdot \hat{n})]\hat{s} \quad (5.2)$$

where $\hat{s} = \left(r_{ij} \cdot \hat{\boldsymbol{y}}, - r_{ij} \cdot \hat{\boldsymbol{x}}\right)/\boldsymbol{r_{ij}}$ is the unit vector tangent to the contact, μ is the surface friction coefficient, k_s is the shear stiffness and Δs is the shear displacement since the formation of the contact. According to equation 5.2, shear displacement is resisted by a linear elastic force which increases to a maximum of μF_{ij}^{n}. The spring constants, k_n and k_s are chosen for rigid grains so that overlap deformation and tangential sliding distances are smaller than the grain size. Values of k_n and k_s follow a non-linear elastic Hertz-Mindlin contact law where the stiffness is a function of the contact force.

Because the equations of motion are stepped forward in time, the positions and stresses on each grain are recorded at each time step. This study uses the recorded positions during slow tectonic loading as the initial states under which different perturbations are applied. This ability is important because it allows us to let a system with an identical history and configuration evolve in different ways under different conditions. How the system evolves after it is perturbed can then be compared to the natural evolution of the

system under slow tectonic loading and changes due to the pulse can be clearly identified.

5.2.2 Boundary Pulse Perturbations

The system is initially loaded by slowly pulling the top wall spring at 10^{-3} m/s, much faster than tectonic rates, but slow compared to the velocity of a single slip event (~1 m/s). Once the strength of the system is reached, the spring force can overcome the frictional resistance of the grains and grains begin to roll or slide over one another. This motion relaxes the spring force and therefore drops the stress ratio. The value of *F/N* at failure under slow loading conditions represents the nominal strength of the packing, S_o. Since loading is slow compared to the slip velocity, grain behavior during slip is decoupled from behavior during the loading phase, essentially ensuring that S_o is independent of the loading velocity for slow loading.

After the strength is known, we move back in time to a point just before failure, where *F/N* is 95% or more of S_o. At this stress ratio, the front end of the spring is held fixed (V_{sp} = 0) and a rapid perturbation is added to the normal stress, *N*. A normal stress perturbation was chosen to avoid any resonance effects in the driving spring. Figure 5.2a shows the prescribed normal force oscillation. This method is intended to mimic a seismic wave passing across a stressed fault, where stresses to the system are applied over milliseconds compared to the years-long stress rate of tectonic activity.

The amplitude of the pulse is chosen to increase F/N slightly over the strength, S_o (Figure 5.2a). However, because the pulse is applied at different stress levels, the exact amplitudes that go above S_o also vary with initial stress. The applied pulse amplitudes ranged from 0.04 – 8 MPa (0.05 – 10% of the confining stress), consistent with previous granular triggering studies (Johnson et al., 2016). Higher amplitude pulses (>1 MPa) were needed to ensure that immediate triggering was seen in every grain pack, for every initial stress condition, and every pulse frequency.

In addition to altering the pulse amplitude, A, we also altered the pulse frequency, $\omega=2\pi f$. Frequencies ranged from 4 – 75 kHz, a range determined by the grain size in our model. For millimeter size grains, such high frequencies are necessary for the pulse to travel completely through the granular system. Lower frequencies (<1 kHz) cause the entire granular pack to shift at once because the wavelength of the perturbation is larger than the height of the system. In the example in Figure 5.2, the amplitude and frequency combination of the pulse push the system just slightly above its original strength for a short time. This is enough to cause a small amount of displacement within the granular layer, which causes a reduction in the shear force, F (Figure 5.2b). Finally, four different granular packings, each with a different S_o value, were pulsed.

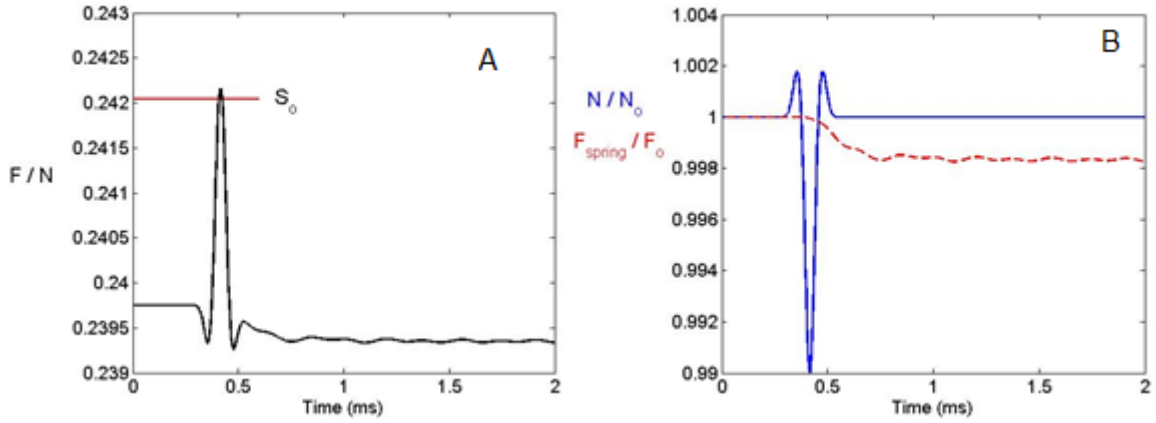

Figure 5.2 A wavelet pulse is input into the top wall of the granular packing while the shear force is held constant. The decrease in normal force increases the stress ratio of $\mathbf{F_{spring}}$/N during the pulse (A). The pulse amplitude is chosen so that it pushes the system above its original strength, S_o. During the pulse, the normal force on to top wall decreases which allows for a slight release of the shear force (B).

5.3 Results

Figure 5.3 shows the main types of behaviors induced by the pulse. When the pulse amplitude is large enough a slip event occurs (Figure 5.3c). A slip event is defined as a horizontal motion of the top wall, caused by grain rearrangement that relieves at least 5% of the stress on the system, although a 20% drop in shear stress is common.

For smaller pulse amplitudes, there is very small inelastic strain to the system, but the system stabilizes as the shear stress is relieved (Figure 5.3a) and a slip event does not occur. These events typically relieve less than 1% of the stress on the system and do not involve major grain rearrangement. The larger pulses that cause immediate slip are referred to as “triggered” simulations, while the smallest amplitudes that are not followed by a slip event are “non-triggered”. For a small range of intermediate amplitudes, slip is triggered by the reverberations of the pulse through the system, not by

the initial pulse itself. These are referred to as “delayed triggering” simulations (Figure 5.3b). We begin by discussing non-triggering smaller amplitude pulses to explore their effect on the strength of the system.

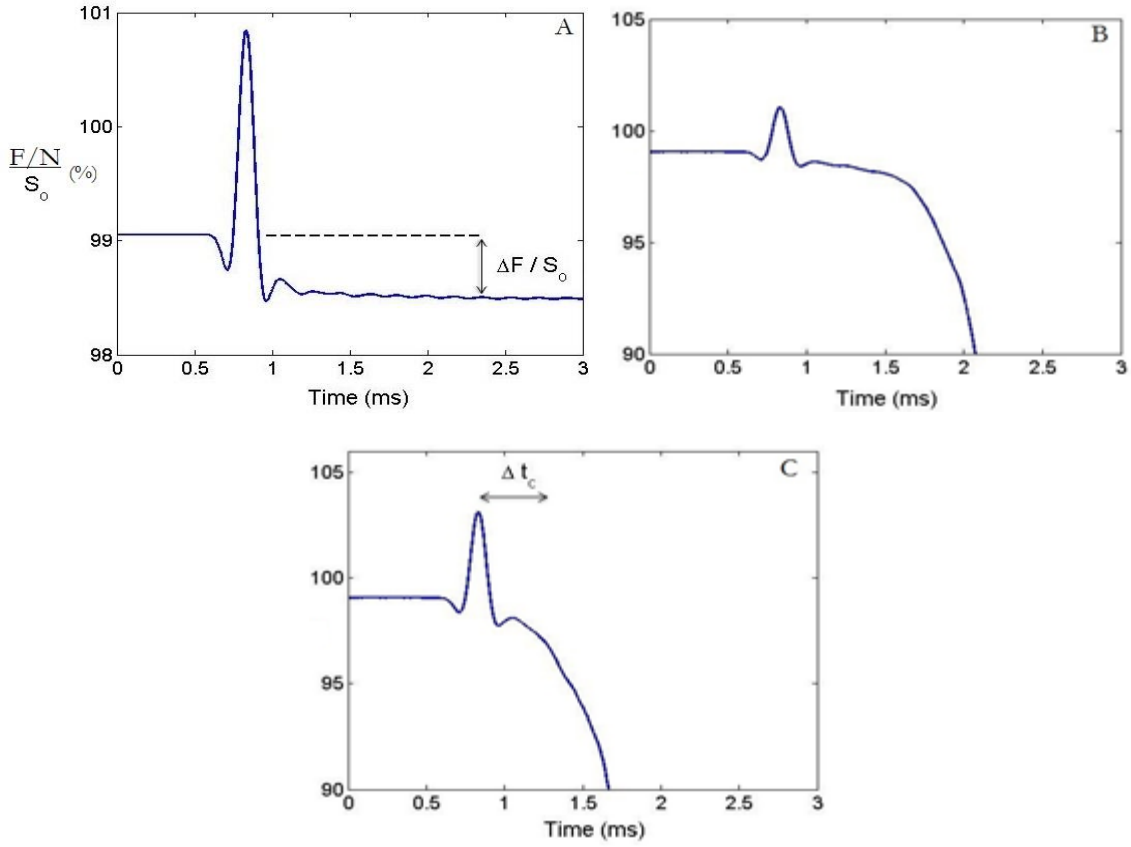

Figure 5.3 Three possible pulse results. In a) the pulse causes a relaxation of the spring force and a slight decrease in the stress ratio, but slip is not triggered. In c) the pulse triggers a slip event, rearranging the grains, relaxing the spring force significantly. There is a large decrease in the stress ratio. This is an example of immediate triggering, where slip begins within $\mathbf{\Delta t_c}$, the time it takes the pulse to pass through the system once. The intermediate state b) shows that for a small range of amplitudes, slip is triggered later than $\mathbf{\Delta t_c}$. These are referred to in the text as “delayed triggering” simulations and are the result of multiple reverberations through the system.

5.3.1 Response to Small Amplitude Pulses

The major change that occurs when a pulse is introduced into the system is a physical displacement of the grains and the corresponding strain that is induced in the system. This slight displacement only begins when the *F/N* value first reaches the original strength, S_o. If *F/N* never exceeds S_o, then any displacement is observed to be elastic and reversible. Once the pulse increases the stress ratio to the strength, two changes happen. First, any non-recoverable displacement works to relieve the shear force, *F*. When *N* returns to the starting value after the pulse, there has been a non-zero reduction in the shear force such that $F' < F_o$, the original shear force. This reduced *F* is given by:

$$F'(x) = F_o - k\,\Delta x \tag{5.3}$$

We observe that this small, non-triggering strain changes the strength of the system. We demonstrate this by reinitiating slow loading after the pulse until failure occurs. Figure 5.4 shows the newly-measured strength of these systems after they have been subjected to various small-amplitude pulses. The post-pulse strength, *S'*, is often different from S_o, the strength of the unpulsed system. At the very low strains caused by smallest amplitude pulses, the system is actually strengthened. This is consistently observed for most initial stress levels and for most pulse frequencies. However, at larger amplitudes the pulses cause enough strain to begin weakening the system. While these pulses still are not large enough to cause failure, by reloading the system and measuring the new strength it is clear that the system has become weaker because of the pulse (Figure 5.4).

Figure 5.5 attempts to quantify this weakening. It takes a certain displacement, X_w, before the system begins to weaken and the exact value varies for every granular system. However, once the critical X_w is reached, successively higher amplitude pulses cause a near-linear decrease in the strength. Figure 5.5 displays this strength reduction for a single granular packing that was pulsed with multiple amplitudes; each data point represents a different simulation from the same starting configuration of grains and stress.

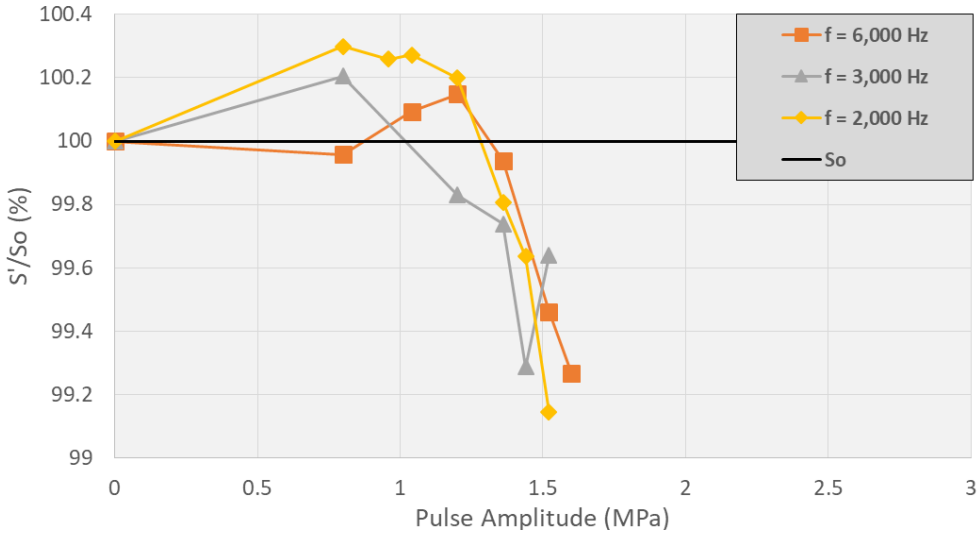

Figure 5.4 Strength measurements of the granular packing subjected to various pulses. All pulses are too low in amplitude to cause triggering, and so, after the pulse dissipates, the system continues to be loading until a slip event occurs. The stress level at which slip occurs is taken to be the new strength, S', for that pack. Each data point on the plot corresponds to the reloaded strength of a granular pack that has been subjected to a pulse of the denoted frequency and amplitude. The smallest amplitude pulses, of all frequencies, tend to strengthen the system slightly, however, above a certain amplitude the system is weakened by the pulses.

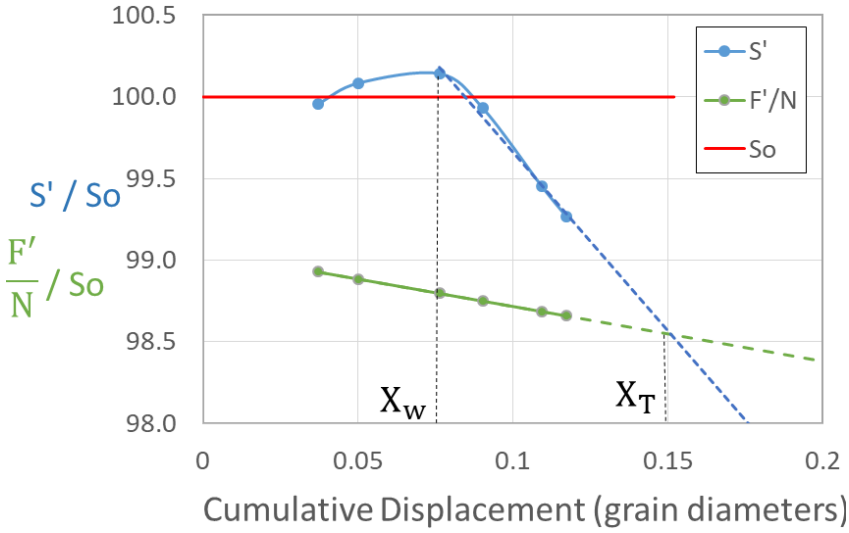

Figure 5.5 The reduction in strength (S') and the reduction in shear force (F') with grain displacement, expressed as a percentage of the nominal strength, So. Data is from the f = 6000 Hz simulation in Figure 5.4. Intersection occurs at 0.15 diameters of displacement. If a pulse causes deformation beyond this point, triggering will occur. Note that the strength is increased for the smallest displacements, but begins to weaken once $\mathbf{F/N_{crit}}$ is reached.

We model only the weakening part of the relationship simply as a linear decrease in strength with strain above X_w.

$$S'(x) = S_o(1 - \beta x) = S_o(1 - \beta[\Delta x - X_W]) \tag{5.4}$$

Where $\Delta x = X_T$ is the full displacement starting from zero and β is a rate of weakening, determined from the fit displayed in Figure 5.5. Like X_w, β is unique to a specific granular packing, but typically ranges from 0.1 to 0.2.

As discussed, the displacement decreases the stored spring force as well as the strength. If the reduced strength of the system falls below the reduced spring force, then a slip event will be triggered. Simply put, the spring would exert more force than the granular

packing could withstand. Figure 5.5 also shows where the strength fit intersects with the weakening spring force, at X_T. After that much total displacement, so much weakening has occurred that the spring force is higher than the strength and slip should be triggered. In this example, X_T occurs at 0.151 grain diameters of displacement, which is x = 0.075 diameters of displacement after the critical X_W. Note that x and X_W can only be measured for simulations of the system that are not triggered, in the event of delayed triggering (discussed later) it is not possible to obtain points closer to X_T.

It is also worth noting that x, X_W, and X_T are all unique to a particular grain configuration. This means that X_W may be larger or smaller for different grain packs and the pulse must cause more displacement for the strength to start decreasing. However, all displacement will work to relieve the spring force. So while the exact intersection of F' and S' will vary depending on when S' begins to decrease, in all cases S' was seen to decrease faster than F'.

The minimum displacement required for triggering, X_T, can be obtained by setting $\frac{F'}{N} = S'$. The resulting expression describes the total displacement necessary:

$$X_T > \frac{S_o - \frac{F_o}{N} - S_o \beta X_W}{S_o \beta - \frac{k}{N}} \tag{5.5}$$

While the exact strain needed will change depending on the granular packing (which causes variations in S_o, F_o, and β), equation 5.5 is consistent with every non-triggered simulation examined.

5.3.2 Immediate Triggering due to Large Amplitude Pulses

The previous section shows that the amount of displacement caused by the pulse is crucial for determining behavior after the pulse is complete. However displacement continues to accumulate after the pulse is applied due to dynamic forces in the system. In this section, we introduce a simplified analysis of those dynamic forces in order to examine the triggering point of the granular system.

If a pulse is large enough, or lasts long enough, there can be enough displacement to instigate failure immediately. To quantify the pulse properties needed to cause immediate failure, we consider a pulse corresponding to half the period of a sinusoid:

$$N = N_o + A \sin(\omega t) \tag{5.6}$$

which is applied from $0 < t < \pi/\omega$.

The set up of our numerical experiments is simpler if a pulse is applied only in the normal force, to avoid interaction with the wall-parallel driving spring. However, the

following analysis is somewhat easier if the pulse is applied in the shear force, *F*. The pulse in the normal force, *N*, is equivalent to a pulse in the shear force, $F=F_o + A\sin(\omega t)$, as long as the pulse is small compared to initial applied forces. Slip begins when the force ratio is equal to the strength. This happens at

$$t_1 = \frac{1}{\omega} sin^{-1}(\frac{S_o - F_o}{A}) \tag{5.7}$$

From this point on, the equation of motion will be

$$m\,\ddot{x} = F - S \tag{5.8}$$

$$m\,\ddot{x} = F_o + A\sin(\omega t) - S \tag{5.9}$$

However, as seen previously, any displacement will alter the strength. Assuming that the system is close enough to failure that *S* decreases linearly with any further displacement, we can substitute Eq. 5.4 for S:

$$\ddot{x} = \frac{A}{m}\sin(\omega t) + \psi + \phi x \tag{5.10}$$

where $\phi = \frac{S_o \beta}{m}$ and $\psi = \frac{\frac{F_O}{N} - S_o}{m}$.

Applying the initial conditions of no displacement or motion until t_1 yields the full solution to this equation (see Appendix A). However, this equation only describes motion during the pulse. We are interested in the motion after the pulse has passed

through the system to see if that post-pulse motion will lead to failure. After the pulse is complete, at t = $\frac{\pi}{\omega}$, the equation of motion simplifies to

$$\ddot{x} = \psi + \phi x \tag{5.11}$$

which has a solution of

$$x = \sqrt{\phi}C_3 e^{\sqrt{\phi}t} + \sqrt{\phi}C_4 e^{-\sqrt{\phi}t} - \frac{\psi}{\phi} \tag{5.12}$$

The coefficients can be determined by applying matching conditions for displacement and velocity solutions to 5.10 and 5.12 at $t = \pi/\omega$. The solution after the pulse is over is then described by:

$$X_{after}(t) = (a+b)e^{\sqrt{\phi}(t-t_1)} + (a-b)e^{-\sqrt{\phi}(t-t_1)} - \frac{\psi}{\phi} \tag{5.13}$$

where $a = \frac{\psi\omega^2}{2\,\phi(\omega+\phi)}$ and $b = \frac{\omega\sqrt{A^2+(F_o/N-S_o)^2}}{2m\sqrt{(\phi)(\omega^2+\phi)}}$.

Slip will be arrested (no triggering) only if a time t_2 exists, at which the velocity goes to zero.

$$0 = \sqrt{\phi}(a+b)e^{\sqrt{\phi}(t_2-t_1)} - \sqrt{\phi}(a-b)e^{-\sqrt{\phi}(t_2-t_1)} \tag{5.14}$$

which can be re-written as

$$0 = a\sinh\left(\sqrt{\phi}(t_2 - t_1)\right) + b\cosh\left(\sqrt{\phi}(t_2 - t_1)\right) \quad (5.15)$$

$$-\frac{b}{a} = \tanh\left(\sqrt{\phi}(t_2 - t_1)\right) \quad (5.16)$$

Since the hyperbolic tangent is limited to ±1, 5.16 is only valid if

$$\frac{b}{a} < |1| \quad (5.17)$$

Therefore, if 5.17 is not true, then no time of zero velocity is possible and the system has been triggered and will generate large slip. Plugging in for *a*, *b*, *φ,* and *ψ*, then rearranging gives:

$$A_{trigger} = (S_o N - F_o)\sqrt{1 + \frac{m\omega^2}{NS_o\beta}} \quad (5.18)$$

the critical amplitude needed to cause runaway slip. For pulse amplitudes above this limit, the velocity will not go to zero after the pulse is complete and slip will continue. The amplitude is a function of the original strength and original force on the system, as well as the frequency of the wave, and the rate at which strength is reduced (β).

To test this relation, we need to determine which pulse amplitudes immediately triggered failure in the granular system. For this we examine the normal stress on the bottom wall of the granular packing (Figure 5.6a). An input pulse passes through the system several times before dying away due to intergranular damping. The pulse is said to cause immediate failure if irreversible slip occurs during the first pass of the pulse through the

system. That is, the pulse should only travel through the system once before causing an irreversible (inelastic) shift leading to failure. The window of time that such a shift must occur in, t_c, can be determined by observing the normal stress on the bottom wall. When the normal stress returns to the original value, one perturbation has completely passed through the system (Figure 5.6a).

Within that time window, the strength and the spring force will both be reduced. The actual values can be calculated using equations 5.2 and 5.3, assuming that the weakening coefficient, β, discovered for the non-triggered simulations is applicable for when a pulse causes slip. If the strength drops below the force within that window, the simulation is considered to be "immediately triggered" as the higher spring force will drive grain slip. Figure 5.6b shows how the strength is more rapidly reduced over $t_c$than force for an immediately triggered run.

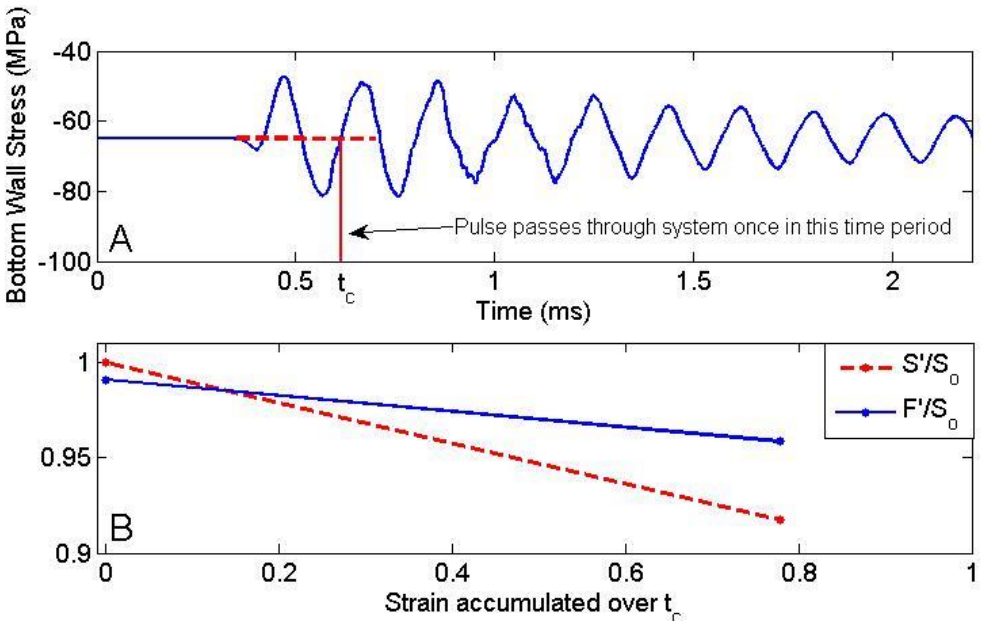

Figure 5.6 Diagram showing the threshold for determining immediate triggering. The time of a single reverberation, $\mathbf{t_c}$, is used to determine if an irreversible deformation has happened in the grains. If the system strength, S / S_0 , falls below the spring force, F_0, within the time window of the first reverberation, then the pulse has caused immediate triggering and slip is inevitable.

For every pulse frequency, this threshold was applied to determine the amplitude that causes immediate failure. Using this frequency-amplitude data, we then applied our fit equation from equation (5.19):

$$A < (S_o N - F_o)\sqrt{1 + b\omega^2} \tag{5.19}$$

where ($S_o N$- F_o) represents the difference between the original strength and the starting stress ratio, ω is the frequency of the pulse, and $b = {}^{m}/_{S_o N \beta}$.

This equation is mostly consistent with the amplitudes that cause triggering in our numerical experiment (Figure 5.7). The pulse applied in the analytic model is simpler

than what occurs in the numerical model because of reverberations in the granular layer, as discussed below. Our definition of immediate triggering is not rigorous and so variability in A is expected. Figure 5.7 shows this with error bars that reach down to the first pulse amplitude that triggers, but does not meet the immediate triggering threshold. Similarly, β is measured from the non-triggering data, which may or may not be applicable for the immediate triggering case. For example, if the system weakens at a faster rate (higher β) as it approaches failure, this will alter our prediction curve, specifically by changing b in Equation 5.19. All things considered, our equation provides a reasonable relationship between features of the pulse - the amplitude and frequency- and the ability to cause immediate triggering.

Table 5.1 Data from a single granular packing pulsed at multiple frequencies until failure. The amplitude value corresponds to the first amplitude were S' falls below F', as explained in Figure 5.6. Data is plotted in Figure 5.7, except for the highest frequency.

Immediate Triggering Amplitudes

Amplitude (MPa)	Frequency (ω) (kHz)
1.04	4.71
1.12	5.39
1.2	6.28
1.28	7.54
1.84	12.57
2.32	18.85
4.0	37.70
4.8	50.27

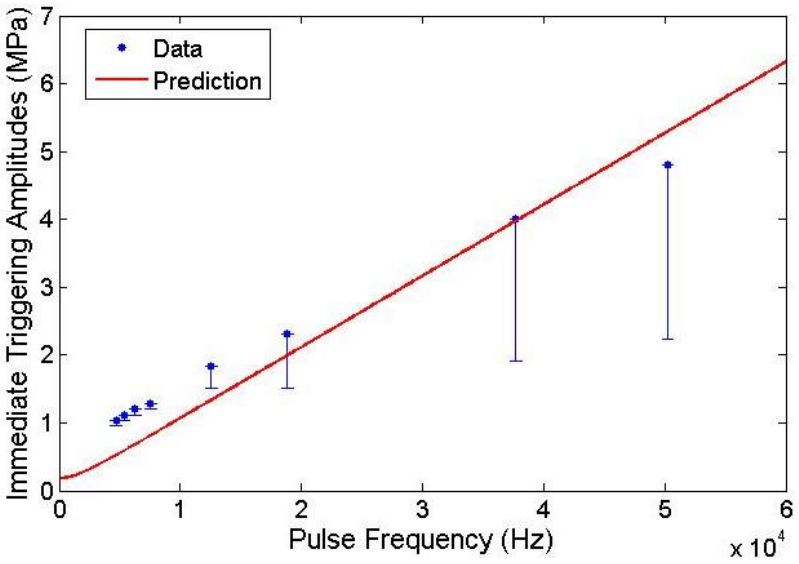

Figure 5.7 The fit of equation 5.19 applied to the immediate triggering data. For each frequency, the lowest amplitude that caused immediate triggering, according to the threshold, was plotted. Error bars show the distance to the first amplitude to cause triggering.

5.3.3 Intermediate Pulse Amplitudes and Delayed Triggering

In a number of our simulations the pulse does not produce enough displacement to cause immediate triggering, but later reverberations continue to reduce the strength until triggering does occur. This "delayed triggering" can be explained by examining the reverberations through the system and how they alter the strength.

Figure 5.8 shows a comparison between the stress on the zero-displacement bottom wall of the granular packing (Fig. 5.8a) and the stress ratio at the top wall (Figure 5.8b). The upper plot shows very clear reverberations through the system after the applied pulse is over. These reverberations are not captured by the stress ratio F/N because N is the external force applied to the top wall and is held fixed after the pulse is complete.

For every pulse, the ringing slowly dies away as energy is dissipated by friction and inelastic damping between the grains. However, when a reverberation passes through the system, the stress ratio may exceed the strength, as it does during the initial pulse. As we have seen before, going above the strength results in accumulating strain and weakening. By using the same relationship between strain and strength that was derived from the non-triggering runs (Equation 5.3), it is possible to estimate the weakening caused by these reverberations.

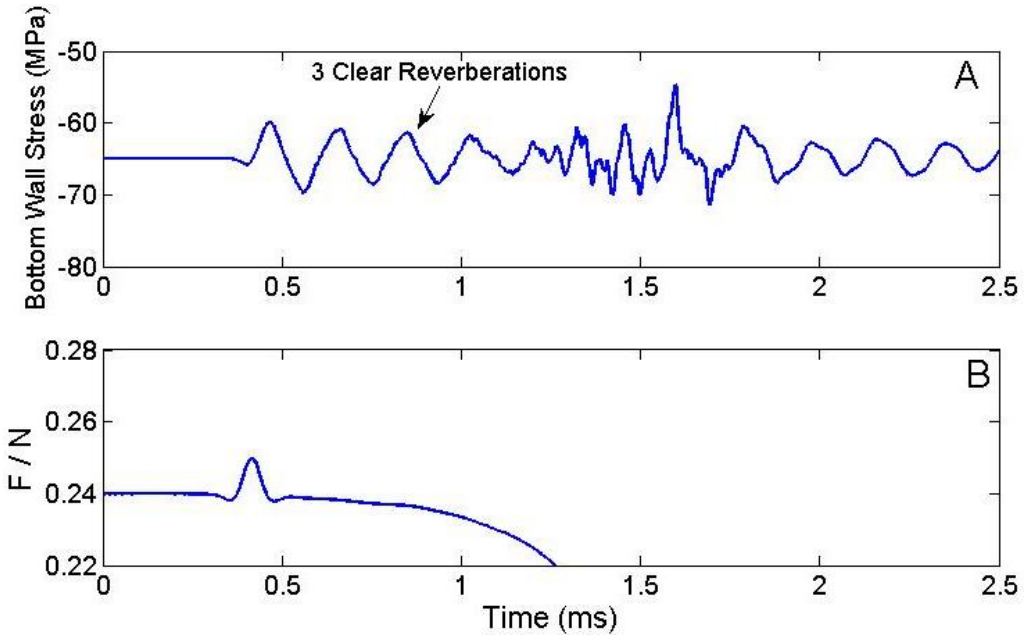

Figure 5.8 Stress on the bottom wall of the granular packing (top). Clear reverberations of the pulse are seen to pass through the system. Stress ratio (F/N) is output for the same simulation, showing a clear slip event which relieves the shear force and decreases the ratio (bottom).

For our example case, Figure 5.9 compares the strength to the shear force on the system. Each data point shows the strength and force after a reverberation is completed, taking

into account the displacement that occurred while the stress ratio was pushed above the strength. Starting at the original strength, the first pulse causes enough strain to lower the strength, but the decrease is not enough to fall below the force. Instead, it is not until the fourth reverberation that the strength falls below the force and slip will occur. This suggests that, for a given amount of strain, the strength falls faster than the shear force.

This is consistent with a β value that is typically larger than k/N, the rate stress is released from the top wall. The large drop in strength between the fourth and fifth reverberations is a clear indication that slip has already begun.

An easier way to visualize the effects of these reverberations is shown in Figure 5.10. Every reverberation continues to lower the strength every time the stress ratio goes above the strength. This continues, as long as the reverberations are large enough, until the strength is below the spring force and slip occurs.

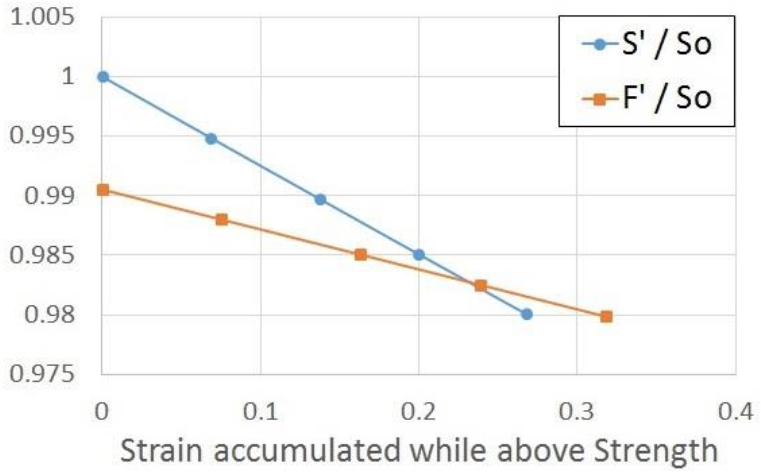

Figure 5.9 A comparison of the spring force on the top wall and the strength of the system, both normalized by the original strength. Note that the spring force on the top wall is also divided by the normal force, as in equation 5.3, so that we are effectively comparing two stress ratios. Strain is accumulated each time the pulse pushes the stress ratio above the strength. This strain works to relieve the spring force and decrease the strength. It is clear that the strength is decreased more rapidly, falling below the spring force during the fourth reverberation of the pulse through the system.

5.4 Discussion

Each of the three behaviors exhibited by the granular system after it has been pulsed – immediate triggering, delayed triggering, and weakening but no triggering – can be explained by the competition between the strength of the system and the force on the system. When the strength is decreased to below the force, failure is inevitable. However, both the strength and the force decrease with strain. The strain must therefore be large enough to allow for a cross-over between strength and force, as seen in Figure 5.5. Higher amplitude pulses and longer period pulses produce more strain and so are more likely to cause failure.

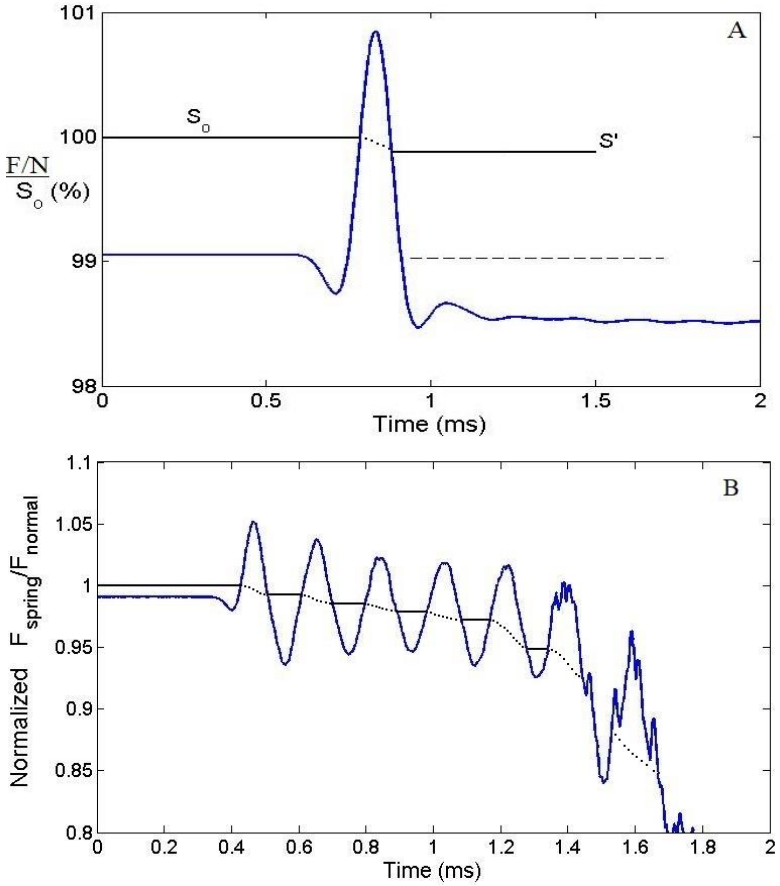

Figure 5.10 Strength weakening due to the pulse. Every time the pulse goes above the strength of the system, that strength is decreased (A). If there are multiple reverberations through the system, then every time the stress ratio F/N goes above the strength S, the system experiences some strain (B). This strain lowers the strength of the system, as shown in the solid black lines. Eventually the strength is decreased enough for the spring force to cause a slip event.

One well-known feature of granular materials is that strain is distributed throughout the granular pack. However, our measurements of strain and displacement have been taken from the top wall. This displacement clearly relates to permanent changes in the strength of the system, as we have shown in Figures 5.4, 5.5 and 5.6, but the details are unclear. To understand exactly what the pulse does to the system, a grain-scale view is needed. Here we will focus on the amount of intergranular slip that occurs on contacts.

Figure 5.11a shows the typical intergranular slip on all contacts during a small increment of strain caused by continuously increasing the shear force at a slow rate. Under this loading situation, the contacts that shift the most (highest Δs) are under a range of normal forces (N), both high and low. The red squares denote contacts that are most favorably oriented for slip: those with contact normal > 60° relative to the shear direction. These high-angle contacts tend to accumulate more slip than low-angle ones.

Figure 5.11b contains the same data for a non-triggered pulsed simulation, in which the displacement of the top wall equaled the same increment as in Figure 5.11a. The contacts in the pulsed simulation slip significantly more. What's more, the slipping contacts are preferentially under low normal force and at a high angle. Clearly the pulse is causing motion on a different set of contacts than the slow loading conditions.

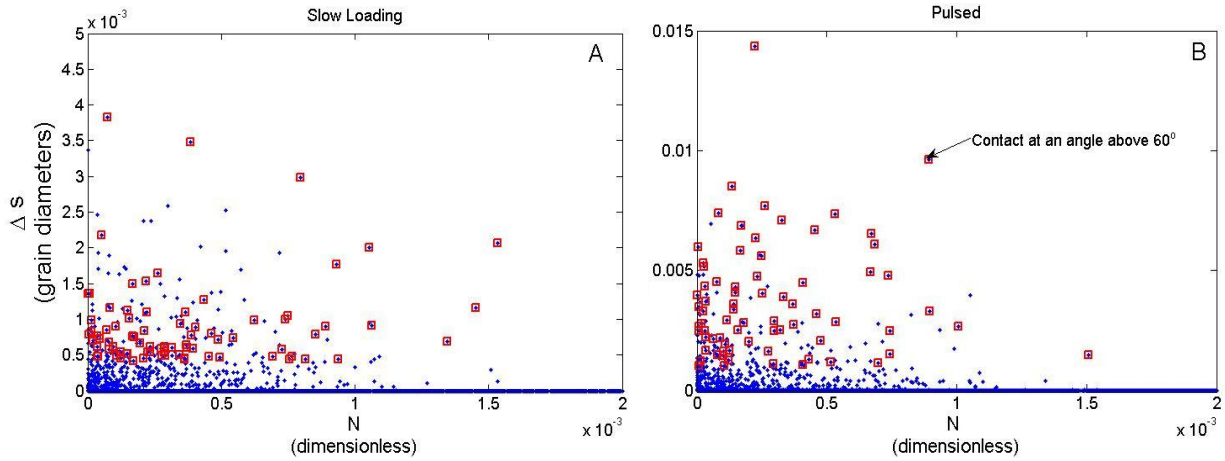

Figure 5.11 Comparison of the contacts that slip when the system is subjected to a constant slow shear loading versus a sudden pulse in confining stress. Only contacts that slip $\Delta s > 0$ are included and plotted against the normal force on the contact. Red boxes mark the contacts that initially, before loading or pulsing, have a contact angle above 60º (only for the contacts within the top 10% of slip magnitude). The comparison is made when the displacement of the top wall is equivalent. Clearly the pulse alters a different set of contacts than typical shear loading. The pulse allows for much higher slip, and that slip is concentrated among the contacts with less normal force. Slow loading allows for more slip along higher stress contacts because the stress has time to distribute throughout the grain pack. The pulse also preferentially shifts contacts at high contact angles. Essentially all of the contacts with the most slip in the pulsed simulation began at a high angle. From this it can be said that the pulse alters a different set of contacts than slow shear loading.

Showing that a different population of grains shift in the pulsed case relative to a more typical loading history is not the same as showing that the pulse weakens the system. For this we turn to a brief discussion of grain dynamics. For a confined granular system that is subject to a shear force, like the system here, the friction between grains resists any sliding or rolling motion. When the shear force is greater than this frictional resistance, the grains will climb over each other to relieve the force (by rolling, sliding, or a combination). This climbing motion naturally increases the contact angle between two grains, and also necessitates local dilation in the layer. Because of the resolution of the

contact forces, the contact in position A exerts a greater overall resistance to the shear motion than a contact in positions B or C.

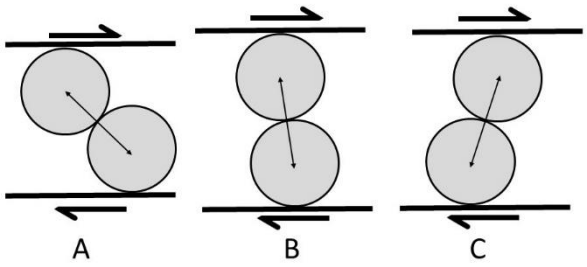

Figure 5.12 Simplified geometry of grains forcing dilation as they climb past each other. When the contact angle between grains is less than 90º, there must be dilation if the grains roll over each other.

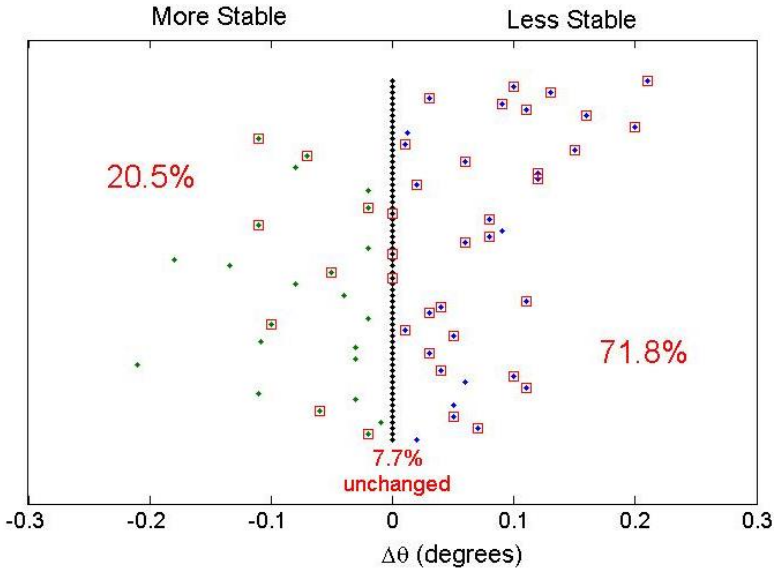

Figure 5.13 Change in contact angle due to the pulse. Points represent contacts that slip the most during the pulse, while the red squares highlight points that are initially at a high contact angle (> 60º). Percentages represent the number of high-angle contacts that become less stable, more stable, or are unchanged due to the pulse.

During the pulse, contacts are free to shift into weaker positions (from A to C). We track this movement and display the results in Figure 5.13 for the highest-slip contacts

previously plotted in Figure 5.11. Contacts are ordered vertically by the amount of slip, from smallest at the bottom to largest at the top, then shifted horizontally according to the change in contact angle. Again, contacts that begin at high angles (> 60º) are marked with a red square. Overwhelmingly, contacts that begin at high angles are made less stable by the pulse, meaning that they shift into a position where they exert less frictional resistance against the shear force. Taken together, this suggests that the pulse preferentially alters high-angle contacts under low normal force by shifting them into a weaker position. This shift ultimately decreases the strength of the entire granular system.

5.5 Conclusion

When a granular system was subjected to small amplitude pulses in the normal stress, three behaviors were observed. Each of these behaviors can be explained by concurrent weakening in the strength of the granular pack and the shear force on the pack. The pulse causes a decrease in normal force, which allows for slight displacements of the grains. For the largest amplitude pulses, this displacement during the pulse is enough for the strength to fall below the shear force. The resulting force imbalance causes a subsequent slip event. Intermediate pulse amplitudes can also cause slip events, but only if the reverberations of the pulse through the system are large enough to continue to decrease the strength. At the smallest amplitudes, the initial pulse and any subsequent reverberations are unable to cause such weakening and no slip event occurs.

This behavior arises because the detailed grain movement can weaken the structure of the granular system with displacement, while only marginally relaxing the loading force. Importantly, this study shows that most of the grain contacts shifted by the pulse are high-angle grain contacts, above 60º, which under low normal force (Figure 5.11). At such high angles, and with less pressure on the contacts, the grain contacts exert less frictional resistance and it is easier to slide or roll without having to climb over the frustrating grain. This particular population of grains are not affected when the system is slowly loaded by increasing the shear force. Therefore, the slip events observed here are unique events, from a different population of contacts, which would not have occurred if the system had not been pulsed.

Micromechanically, we were able to determine that high-angle contacts with low normal force slipped the most due to the pulse. By reloading non-triggering systems, we were also able to show that slip among this contact population results in a weaker system ($S' < S_o$). However, we do not understand the specific mechanics of this link. Future work will focus on how this population of weak contacts, deforming locally within the granular system, can lead to a significant reduction in shear strength.

6. CONCLUSIONS

The study of dynamically triggered earthquakes has just begun. This work highlights one possible path for research on this topic. Since it remains impossible to predict exactly when an earthquake will strike, it is equally impossible to put the correct sensors in the correct positions to measure earthquake outputs – strain rates, displacements, and other parameters alongside the fault- before, during, and after an event. These are precisely the parameters that scientists need to characterize if they are to understand what forces a triggered fault is being subject to. What does one fault produce, and in what quantities and magnitudes, that is triggering activity in a separate fault in the far-field?

Fortunately, dynamic rupture models can and are providing this information. The work presented here is an initial step in this direction, where off-fault outputs from our pulverized rock models show the variety of situations produced off the fault, from the sharp strain rate peaks produced during the supershear transition (Figure 4.5B) or the steady rise in the peak stress produced by a long-propagating subshear rupture (Figure 4.4A). It remains to be seen how these near-fault features change with distance from the fault, and whether observations of triggering correlate well with any specific type of earthquake from any particular direction. Regardless, as long as the physical laws incorporated in dynamic rupture simulations hold true, they provide an exceptional window into this phenomenon.

Coupled with this advance is the continued work on the smallest of scales. Granular materials, with their jumble of fluid and solid-like behaviors, can be very complicated, and yet we know they play a major role in determining fault stability. The fault core is believed to be the weakest zone, and is exactly the area we expect to be most agitated by passing seismic waves. Furthermore, this work shows the range of behaviors that can be induced in granular materials even with simple perturbations. The ability of more realistic time-varying pulses to cause, or even prevent, slip is a further area of research. Tying in features of the fault core with broader knowledge of fault slip and rupture is necessary to reach a full understanding of fault behavior. There remains much work to be done.

REFERENCES

Aben, F.M., Doan, M.-L., Mitchell, T.M., Toussaint, R., Reschla, T., Fondriest, M., Gratier, J.-P., and F. Renard. 2016. "Dynamic fracturing by successive coseismic loadings leads to pulverization in active fault zones." *J. Geophys. Res.* 121: 2338-23360.

Aharonov, E., and D. Sparks. 2002. "Shear profiles and localization in simulations of granular materials." *Phys. Res. E* 65: 051302. doi:10.1103/PhysRevE.65.051302.

Aharonov, E., and D. Sparks. 2004. "Stick-slip motion in simulated granular layers." *J. Geophys. Res.* 109: B09306. doi:10.1029/2003JB002597.

Anderson, J.G, Brune, J.N., Louie, J.N., Zeng, Y., Savage, M., Yu, G., Chen, Q., and D. dePolo. 1994. "Seismicity in the Western Great Basin Apparently Triggered by the Landers, California, Earthquake, 28 June 1992." *Bull. Seism. Soc. Am.* 84 (3): 863-891.

Andrews, D.J. 2002. "Comment on "How fast is rupture during an earthquake? New Insights into the 1999 Turkey earthquakes"." *Geophys. Res. Lett.* 29 (15). doi:10.1029/2001GL014126.

Andrews, D.J. 1976. "Rupture velocity of plane strain shear cracks." *J. Geophys. Res.* 81: 5679-5687.

Ben-Zion, Y. and Z. Shi. 2005. "Dynamic rupture on material interface with spontaneous generation of plastic strain in the bulk." *Earth Planet. Sci. Lett.* 236: 486-496.

Bizzarri, A. and S. Das. 2012. "Mechanics of 3-D shear cracks between Rayleigh and shear wave rupture speeds." *Earth Planet. Sci. Lett.* 357-358: 397-404.

Bizzarri, A. 2010. "How to promote earthquake ruptures: different nucleation strategies in a dynamic model with slip-weakening friction." *Bull. Seism. Soc. Am* 100 (3): 923-940.

Bizzarri, A., Dunham, E.M., and P. Spudich. 2010. "Coherence of Mach fronts during heterogeneous supershear rupture propagation: simulations and comparison with observations." *J. Geophys. Res.* 115: B08301. doi:10.1029/2009JB006819.

Bouchon, M. and M. Vallee. 2003. "Observations of long supershear rupture during the magnitude 8.1 Kunlunshan earthquake." *Science* 301: 824-826.

Bouchon, M., Toksoz, M.N., Karabulut, H., Bouin, M.P., Deitrich, M., and A.J. Rosakis. 2001. "How fast is rupture during an earthquake? New insights from the 1999 Turkey earthquakes." *Geophys. Res. Lett.* 28: 2723-2726.

Broberg, K.B. 1996. "How fast can a crack go?" *Mater. Sci.* 32 (1): 80-86.

Broberg, K.B. 1999. "Intersonic mode II crack acceleration." *Fatigue Fract. Eng. Mater. Struct.* 22: 17-24.

Brodsky, E.E. and S. Prejean. 2005. "New constrains on mechanisms of remotely triggered seismicity at Long Valley Caldera." *J. Geophys. Res.* 110: B04302.

Brodsky, E.E., and N.J. van der Elst. 2014. "The Uses of Dynamic Earthquake Triggering." *Annu. Rev. Earth Planet. Sci.* 42: 317-339. doi:10.1146/annurev-earth-060313-054648.

Brune, J.N. 2001. "Fault-normal dynamic unloading and loading: an explanation for "non-gouge" rock powder and lack of fault-parallel shear bans along the San Andreas Fault." *AGU Fall Meeting Abstracts* S22B-0655.

Burridge, R. 1973. "Admissible speeds for plane-strain self-similar shear cracks with friction but lacking cohesion." *Geophys. J. R. Astr. Soc.* 35: 439-455.

Burridge, R., Conn, G., and L.B. Freund. 1979. "The stability of a rapid Mode II shear crack with finite cohesive traction." *J. Geophys. Res.* 84: 2210-2222.

Chester, F.M. and J.S. Chester. 19998. "Ultracataclasite structure and friction processes of the San Andreas fault." *Tectonophysics* 295: 199-221.

Chester, F.M., Evans, J.P., and R.L. Biegel. 1993. "Internal structure and weakening mechanism of the San Andreas fault." *J. Geophys. Res.* 98: 771-786.

Cohee, B.P. and G.C. Beroza. 1994. "Slip distribution of the 1992 Landers earthquake and its implications for earthquake source mechanics." *Bull. Seism. Soc. Am.* 692-712.

Cundall, P.A. and O.D. Strack. 1979. "A discrete numerical model for granular assemblies." *Geotechnique* 29: 47-65.

Das, S. and K. Aki. 1977. "A numerical study of two-dimensional spontaneous rupture propagation." *Geophys. J. R. Astr. Soc.* 50: 643-668.

Day, S.M. 1982. "Three-dimensional simulation of spontaneous rupture: the effect of nonuniform prestress." *Bull. Seism. Soc. Am.* 72: 1881-1902.

Day, S.M., Dalguer, L.A., Lapusta, N., and Y. Liu. 2005. "Comparison of finite difference and boundary integral solutions to three dimensional spontaneous rupture." *J. Geophys. Res.* 110: B12307. doi:10.1029/2005JB003813.

Denoual, C. and F. Hild. 2000. "A damage model for the dynamic fragmentation of brittle solids." *Comput. Methods Appl. Mech. Eng.* 183 (3-4): 247-258.

Denoual, C. and F. Hild. 2002. "Dynamic fragmentation of brittle solids: a multi-scale model." *Eur. J. Mech. A* 21 (1): 105-120.

Doan, M.-L. and V. d'Hour. 2012. "Effect of initial damage on rock pulverization along faults." *J. Struct. Geol.* 45: 113-124.

Dor, O., and Ben-Zion, Y., and Rockwell, T.K. and J. Brune. 2006. "Pulverized rocks in the Mojave section of the San Andreas Fault Zone." *Earth Planet. Sci. Lett.* 245: 642-654.

Dor, O., Yildirim, C., Rockwell, T.K., Ben-Zion, Y., Emre, O., Sisk, M and T.Y. Duman. 2008. "Geological and geomorphologic asymmetry across the rupture zones of the 1943 and 1944 earthquakes on the North Anatolian Fault: possible signals for preferred earthquake propagation direction." *Geophys. J. Int.* 173: 483-504.

Duan, B. and D.D. Oglesby. 2006. "Heterogeneous fault stress from previous earthquakes and the effect on dynamics of parallel strike-slip faults." *J. Geophys. Res.* 111: B05309. doi:doi:10.1029/2005JB004138.

Duan, B. and D.D. Oglesby. 2007. "Nonuniform prestress from prior earthquakes and the effect on dynamics of branched fault systems." *J. Geophys. Res.* 112: B05308. doi:10.1029/2006JB004443.

Duan, B. and S.M. Day. 2008. "Inelastic strain distribution and seismic radiation from rupture of a fault kink." *J. Geophys. Res.* 113: B12311. doi:10.1029/2008JB005847.

Duan, B. 2010. "Role of initial stress rotations in rupture dynamics and ground motion: a case study with implications for the Wenchuan earthquake." *J. Geophys. Res.* 115: B05301. doi:doi:10.1029/2009JB006750.

Duan, B. 2012. "Dynamic rupture of the 2011 Mw 9.0 Tohoku-Oki earthquake: roles of a possible subducting seamount." *J. Geophys. Res.* 117: B05311. doi:10.1029/2011JB009124.

Dunham, E.M. and H.S. Bhat. 2008. "Attenuation of radiated ground motions and stresses from three-dimensional supershear ruptures." *J. Geophys. Res.* 113: B08319. doi:10.1029/2007/JB005182.

Dunham, E.M. and J.R. Archuleta. 2004. "Evidence for a supershear transient during the 2002 Denali fault earthquake." *Bull. Seism. Soc. Am.* 94: S256-S268.

Dunham, E.M. and J.R. Archuleta. 2005. "Near-source ground motion from steady state dynamic rupture pulses." *Geophys. Res. Lett.* 32: L03302. doi:10.1029/2004GL021793.

Dunham, E.M. 2007. "Conditions governing the occurrence of supershear ruptures under slip-weakening friction." *J. Geophys. Res.* 112: B07302. doi:10.1029/2006JB004717.

Ferdowsi, B., Griffa, M., Guyer, R.A., Johnson, P.A., and J. Carmeliet. 2014. "Effect of boundary vibration on the frictional behavior of a dense sheared granular layer." *Acta Mech* 8: 2227-2237.

Festa, G. and J.-P. Vilotte. 2006. "Influence of the rupture initiation on the intersonic transition: crack-like versus pulse-like modes." *Geophys. Res. Lett.* 33: L15320. doi:10.1029/2006GL026378.

Freed, A.M. 2005. "Earthquake triggering by static, dynamic, and postseismic stress transfer." *Annu. Rev. Earth Planet. Sci.* 33: 335-367.

Giacco, F., et al. 2015. "Dynamic weakening by acoustic fluidization during stick-slip motion." *Phys. Rev. Lett.* 115: 128001. doi:10.1103/PhysRevLett.115.128001.

Gomberg, J. and P. Bodin. 1994. "Triggering of the Ms = 5.4 Little Skull Mountain, Nevada, Earthquake with Dynamic Strains." *Bull. Seims. Soc. Am.* 84 (3): 844-853.

Gomberg, J. and S. Davis. 1996. "Stress/strain changes and triggered seismicity at The Geysers, California." *Geophys. Res.* 101 (B1): 733-749.

Gomberg, J., Bodin, P., Larson, K., and H. Dragert. 2004. "Earthquake nucleation by transient deformations caused by the M=7.9 Denali, Alaska, earthquake." *Nature* 427: 621-624.

Gomberg, J., Reasenberg, P., Bodin, P., and R. Harris. 2001. "Earthquake triggering by seismic waves following the Landers and Hector mine earthquakes." *Nature* 411: 462-466.

Griffa, M., Ferdowsi, B., Daub, E., Guyer, R., Johnson, P., Marone, C., and J. Carmeliet. 2013. "Influence of vibration amplitude on dynamic triggering of slip in sheared granular layers." *Phys. Rev. E* 84: 012205.

Harris, R.A. et al. 2009. "The SCEC/USGS dynamic earthquake rupture code verification exercise." *Seismol. Res. Lett.* 80 (1): 119-126.

Harris, R.A. 1998. "Introduction to special section: Stress triggeres, stress shadows, and implications for seismic hazard." *J. Geophys. Res.* 103 (B10): 24347-24358.

Hild, F., Forquin, P. and A.R. Cordeiro da Silva. 2003. "Single and multiple fragmentation of brittle geomaterials." *Rev. Fr. Genie Giv.* 7 (7-8): 973-1003.

Hill, D.P. 1993. "Seismicity remotely triggered by the magnitude 7.3 Landers, California, earthquake ." *Science* 260: 1617-1623.

Ida, Y. 1972. "Cohesive force across the tip of a longitudinal shear crack and Griffith's specific surface energy." *J. Geophys. Res.* 76: 3796-3805.

Johnson, P.A., and X. Jia. 2005. "Nonlinear dynamics, granular media and dynamic earthquake triggering." *Nature Letters* 437: 871-874. doi:10.1038/nature04015.

Johnson, P.A., Carmeliet, J., Savage, H.M., Scuderi, M., Carpenter, B.M., Guyer, R.A., Daub, E.G., and C. Marone. 2016. "Dynamically triggered slip leading to sustained fault gouge weakening under laboratory shear conditions." *Geophys. Res. Lett.* 43: 1559-1565. doi:10.1002/2015GL067056.

Johnson, P.A., Savage, H., Knuth, M., Gomberg, J., and C. Marone. 2008. "Effects of acoustic waves in stick-slip in granular media and implications for earthquakes." *Nature* 451: 57-60.

Jónsson, S., Zebker, H., Segall, P. and F. Amelung. 2002. "Fault slip distribution of the 1999 Mw 7.1 Hector Mine, California, earthquake, estimated from satellite radar and GPS measurements." *Bull. Seism. Soc. Am.* 92 (4): 1377-1389.

King, G.C.P., Stein, R.S., and J. Lin. 1994. "Static Stress Changes and the Triggering of Earthquakes." *Bull. Seism. Soc. Am.* 84 (3): 935-953.

Li, H., Li, J., Liu, B., Li, J., Li, S. and X. Xia. 2013. "Direct tension test for rock material under different strain rates at quasi-static loads." *Rock Mech. Rock Eng.* 46: 1247-1254.

Madariaga, R. 1983. "High frequency radiation from dynamic earthquake fault models." *Ann. Geophys.* 1: 17-23.

Mitchell, T.M., Ben-Zion, Y. and T. Shimamoto. 2011. "Pulverized fault rocks and damage asymmetry along the Arima-Takatsuki Tectonic Line, Japan." *Earth Planet. Sci. Lett.* 308: 284-297.

Mora, P. and D. Place. 1999. "The weakness of earthquake faults." *Geophys. Res. Lett.* 123-126.

Morgan, J.K. 1999. "Numerical simulations of granular shear zones using the distinct element method 2. Effects of particle size distribution and interparticle friction on mechanical behavior." *J. Geophys. Res.* 104 (B2): 2721-2732.

Payne, R.M. and B. Duan. 2015. "Influence of initial stress and rupture initiation parameters on forbidden zone rupture propagation." *Geophys. J. Int.* 201: 70-77. doi:10.1093/gji/ggv004.

Payne, R.M. and B. Duan. 2017. "Insights into pulverized rock formation from dynamic rupture models of earthquakes." *Geophys. J. Int.* 208: 715-723. doi:10.1093/gji/ggw436.

Perras, M.A. and M.S. Diederichs. 2014. "A review of the tensile strength of rock: concepts and testing." *Geotech. Geol. Eng.* 32: 525-546.

Prejean, E.E. Brodsky and S. 2005. "New constraints on mechanisms of remotely triggered seismicity at Long Valley Caldera." *J. Geophys. Res.* 110: B04302.

Prejean, S.G., Hill, D.P., Brodsky, E.E., Hough, S.E., Johnston, M.J.S., Malone, S.D., Oppenheimer, D.H., Pitt, A.M. and K.B. Richards-Dinger. 2004. "Remotely Triggered Seismicity on the United States West Coast following the Mw 7.9 Denali Fault Earthquake." *Bull. Seism. Soc. Am.* 94 (6B): S348-S359.

Rempe, M.,Mitchell, T., Renner, J., Nippress, S., Ben-Zion, Y. and T. Rockwell. 2013. "Damage and seismic velocity structure of pulverized rocks near the San Andreas Fault." *J. Geophys. Res.* 118: 2813-2831.

Rockwell, T.,Matthews, S., Girty, G., Dor, O.,Wechsler, N. and Y. Ben-Zion. 2009. "Chemical and physical characteristics of Pulverized Tejon Lookout Granite adjacent to the San Andreas and Garlock Faults: implications for earthquake physics." *Pure Appl. Geophys.* 166. doi:doi:10.1007/s00024-009-0514-1.

Rosakis, A.J., Samudrala, O., and D. Coker. 1999. "Cracks faster than the shear wave speed." *Science* 284: 1337-1340.

Scholz, C.H. 2002. *The Mechanics of Earthquakes and Faulting.* 2nd. Cambridge: Cambridge University Press.

Segall, P. 1989. "Earthquakes triggered by fluid extraction." *Geology* 17 (10): 942-946.

Shapiro, S.A. and C. Dinske. 2009. "Fluid-induced seismicity: Pressure diffusion and hydraulic fracturing." *Geophys. Prospecting* 57: 301-310. doi:10.1111/j.1365-2478.2008.00770.x.

Slingerland, R. and L. Kump. 2011. *Mathematical Modeling of Earth's Dynamical Systems.* Princeton University Press.

Spudich, A. Bizzarri and P. n.d. "Effects of supershear rupture speed on the high-frequency content of S waves investigated using spontaneous dynamic rupture models and isochrone theory." *J. Geophys. Res.* 113: B05304. doi:10.1029/2007B005146.

Stein, R.S., King, G.C.P., and J. Lin. 1992. "Change in Failure Stress on the Southern San Andreas Fault System Caused by the 1992 Magnitude = 7.4 Landers Earthquake." *Science* 258: 1328-1332.

van der Elst, N.J. and E.E. Brodsky. 2010. "Connecting near-field and far-field earthquake triggering to dynamic strain." *J. Geophys. Res.* 115: B07311. doi:10.1029/2009JB006681.

Wechsler, N., Allen, E.E., Rockwell, T.K., Girty, G., Chester, J.S. and Y. Ben-Zion. 2011. "Characterization of pulverized granitoids in a shallow core along the San Andreas Fault, Littlerock, CA." *Geophys. J. Int.* 186: 401-417.

Weertman, J. 2002. "Subsonic type earthquake dislocation moving at approximately √2 x shear wave velocity on interface between half spaces of slightly different elastic constants." *Geophys. Res. Lett.* 29 (10): 1470. doi:10.1029/2001GL013916.

Wu. X, Duan. B. and V. Taylor. 2011. "Parallel earthquake simulations on large-scale multicore computers." In *Handbook of Data Intensive Computing*, by B. Furht and A. Escalante, 539-562. Springer.

Xia, K., Rosakis, A.J. and H. Kanamori. 2004. "Laboratory Earthquakes: the sub-Rayleigh-to-Supershear rupture transition." *Science* 303: 1859-1861.

Yuan, F., Prakash, V. and T. Tullis. 2011. "Origin of pulverized rocks during earthquake fault rupture." *J. Geophys. Res.* 116: B06309. doi:10.1029/2010JB007721.

APPENDIX A

Derivation of Immediate Triggering Pulse Amplitudes

During the pulse, the equation of motion is

$$m\ddot{x} = F_o + A\sin(\omega t) - S_o(1 - \beta x)$$

Here Fo and A have been normalized by the Normal Stress, but everything else is dimensional.

$$m\ddot{x} = F_o - S_o + A\sin(\omega t) + S_o\beta x)$$

$$\ddot{x} - \frac{S_o\beta}{m}x = \frac{(F_o - S_o)}{m} + \frac{A}{m}\sin(\omega t)$$

$$\ddot{x} - \phi x = \psi + \frac{A}{m}\sin(\omega t)$$

The solution to this equation, from Mathematica, is

$$x(t) = C1\, e^{\sqrt{\phi}t} + C2\, e^{-\sqrt{\phi}t} - \frac{A}{m(\omega^2 + \phi)}\sin(\omega t) - \frac{\psi\omega^2}{\phi(\omega^2 + \phi)} - \frac{\psi}{\omega^2 + \phi}$$

The velocity is then

$$\dot{x}(t) = \sqrt{\phi}C1\, e^{\sqrt{\phi}t} - \sqrt{\phi}C2\, e^{-\sqrt{\phi}t} - \frac{A\omega}{m(\omega^2 + \phi)}\cos(\omega t)$$

Now our initial conditions are that there is no slip until t1, when the force reaches the strength for the first time. $x(t_1) = 0, \dot{x}(t_1) = 0$

Note: $\sin(\omega t_1) = \frac{S_o - F_o}{A}$ and using a trig identity $\cos(\omega t_1) = \frac{\sqrt{A^2 - (S_o - F_o)^2}}{A}$

Starting with displacement:

$$0 = C1\, e^{\sqrt{\phi}t1} + C2\, e^{-\sqrt{\phi}t1} - \frac{A}{m(\omega^2+\phi)}\sin(\omega t1) - \frac{\psi\omega^2}{\phi(\omega^2+\phi)} - \frac{\psi}{\omega^2+\phi}$$

$$C1\, e^{\sqrt{\phi}t1} + C2\, e^{-\sqrt{\phi}t1} = \frac{A}{m(\omega^2+\phi)}\sin(\omega t1) + \frac{\psi\omega^2}{\phi(\omega^2+\phi)} + \frac{\psi}{\omega^2+\phi}$$

$$C1\, e^{\sqrt{\phi}t1} + C2\, e^{-\sqrt{\phi}t1} = \frac{A}{m(\omega^2+\phi)}\left(\frac{S_o - F_o}{A}\right) + \frac{\psi\omega^2}{\phi(\omega^2+\phi)} + \frac{\psi}{\omega^2+\phi}$$

$$C1\, e^{\sqrt{\phi}t1} + C2\, e^{-\sqrt{\phi}t1} = \frac{S_o - F_o}{m(\omega^2+\phi)} + \frac{\psi\omega^2}{\phi(\omega^2+\phi)} + \frac{\psi}{\omega^2+\phi}$$

$$C1\, e^{\sqrt{\phi}t1} + C2\, e^{-\sqrt{\phi}t1} = \frac{-\psi}{(\omega^2+\phi)} + \frac{\psi\omega^2}{\phi(\omega^2+\phi)} + \frac{\psi}{\omega^2+\phi}$$

$$C1\, e^{\sqrt{\phi}t1} + C2\, e^{-\sqrt{\phi}t1} = \frac{\psi\omega^2}{\phi(\omega^2+\phi)}$$

$$C1\ = \left[\frac{\psi\omega^2}{\phi(\omega^2+\phi)} - C2\, e^{-\sqrt{\phi}t1}\right] e^{-\sqrt{\phi}t1}$$

Ok now let's move to the velocity

$$0 = \sqrt{\phi}C1\, e^{\sqrt{\phi}t1} - \sqrt{\phi}C2\, e^{-\sqrt{\phi}t1} - \frac{A\omega}{m(\omega^2+\phi)}\cos(\omega t1)$$

$$C2\, e^{-\sqrt{\phi}t1} = C1\, e^{\sqrt{\phi}t1} - \frac{A\omega}{m\sqrt{\phi}(\omega^2+\phi)}\left[\frac{\sqrt{A^2-(S_o-F_o)^2}}{A}\right]$$

$$C2\, e^{-\sqrt{\phi}t1} = \left[\frac{\psi\omega^2}{\phi(\omega^2+\phi)}\, e^{-\sqrt{\phi}t1} - C2\, e^{-2\sqrt{\phi}t1}\right] e^{\sqrt{\phi}t1} - \frac{\omega\sqrt{A^2-(S_o-F_o)^2}}{m\sqrt{\phi}(\omega^2+\phi)}$$

$$C2\, e^{-\sqrt{\phi}t1} = \frac{\psi\omega^2}{\phi(\omega^2+\phi)} - C2\, e^{-\sqrt{\phi}t1} - \frac{\omega\sqrt{A^2-(S_o-F_o)^2}}{m\sqrt{\phi}(\omega^2+\phi)}$$

$$2 * C2\, e^{-\sqrt{\phi}t1} = \frac{\psi\omega^2}{\phi(\omega^2+\phi)} - \frac{\omega\sqrt{A^2-(S_o-F_o)^2}}{m\sqrt{\phi}(\omega^2+\phi)}$$

$$\boldsymbol{C2} = \left[\frac{\boldsymbol{\psi\omega^2}}{\boldsymbol{2\phi(\omega^2+\phi)}} - \frac{\boldsymbol{\omega\sqrt{A^2-(S_o-F_o)^2}}}{\boldsymbol{2m\sqrt{\phi}(\omega^2+\phi)}}\right] \boldsymbol{e^{\sqrt{\phi}t1}}$$

Let's simplify this by setting **a**=$\frac{\psi\omega^2}{2\phi(\omega^2+\phi)}$ **b**=$\frac{\omega\sqrt{A^2-(S_o-F_o)^2}}{2m\sqrt{\phi}(\omega^2+\phi)}$ **c**=$\frac{A}{2m(\omega^2+\phi)}$

$$\boldsymbol{C2} = [\boldsymbol{a}-\boldsymbol{b}]\, \boldsymbol{e^{\sqrt{\phi}t1}}$$

Now we need to go back and plug this into our C1 expression

$$C1 = \frac{\psi\omega^2}{\phi(\omega^2+\phi)} e^{-\sqrt{\phi}t1} - C2\, e^{-2\sqrt{\phi}t1} = 2a\, e^{-\sqrt{\phi}t1} - C2\, e^{-2\sqrt{\phi}t1}$$

$$C1 = 2a\, e^{-\sqrt{\phi}t1} - \left[[a-b]\, e^{\sqrt{\phi}t1}\right] e^{-2\sqrt{\phi}t1}$$

$$C1 = 2a\, e^{-\sqrt{\phi}t1} - [a-b]\, e^{-\sqrt{\phi}t1}$$

$$C1 = 2a\, e^{-\sqrt{\phi}t1} - a\, e^{-\sqrt{\phi}t1} + b\, e^{-\sqrt{\phi}t1}$$

$$C1 = a\, e^{-\sqrt{\phi}t1} + b\, e^{-\sqrt{\phi}t1}$$

$$\boldsymbol{C1} = [\boldsymbol{a}+\boldsymbol{b}]\, \boldsymbol{e^{-\sqrt{\phi}t1}}$$

Back to the original equation to plug in

$$x(t) = C1\, e^{\sqrt{\phi}t} + C2\, e^{-\sqrt{\phi}t} - \frac{A}{m(\omega^2+\phi)}\sin(\omega t) - \frac{\psi\omega^2}{\phi(\omega^2+\phi)} - \frac{\psi}{\omega^2+\phi}$$

$$x(t) = C1\, e^{\sqrt{\phi}t} + C2\, e^{-\sqrt{\phi}t} - 2c\sin(\omega t) - 2a - \frac{\psi}{\omega^2+\phi}$$

$$x(t) = [a+b]\, e^{-\sqrt{\phi}t1}\, e^{\sqrt{\phi}t} + [a-b]\, e^{\sqrt{\phi}t1} e^{-\sqrt{\phi}t} - 2c\sin(\omega t) - 2a - \frac{\psi}{\omega^2+\phi}$$

$$x(t) = [a+b]\, e^{\sqrt{\phi}(t-t1)} + [a-b]\, e^{-\sqrt{\phi}(t-t1)} - 2c\sin(\omega t) - 2a - \frac{\psi}{\omega^2+\phi}$$

$$x(t) = a\, e^{\sqrt{\phi}(t-t1)} + a\, e^{-\sqrt{\phi}(t-t1)} + b\, e^{\sqrt{\phi}(t-t1)} - \; b\, e^{-\sqrt{\phi}(t-t1)} - 2c\sin(\omega t) - 2a - \frac{\psi}{\omega^2 + \phi}$$

$$x(t) = a\left[e^{\sqrt{\phi}(t-t1)} + e^{-\sqrt{\phi}(t-t1)}\right] + b\left[e^{\sqrt{\phi}(t-t1)} - e^{-\sqrt{\phi}(t-t1)}\right] - 2c\sin(\omega t) - 2a - \frac{\psi}{\omega^2 + \phi}$$

$$\boldsymbol{x(t) = 2a\cosh(\sqrt{\phi}(t - t1)) + 2b\sinh(\sqrt{\phi}(t - t1)) - 2c\sin(\omega t) - 2a - \frac{\psi}{\omega^2 + \phi}}$$

Velocity

$$\dot{x}(t) = \sqrt{\phi}C1\, e^{\sqrt{\phi}t} - \sqrt{\phi}C2\, e^{-\sqrt{\phi}t} - \frac{A\omega}{m(\omega^2 + \phi)}\cos(\omega t)$$

$$\dot{x}(t) = \sqrt{\phi}C1\, e^{\sqrt{\phi}t} - \sqrt{\phi}C2\, e^{-\sqrt{\phi}t} - 2\omega c\cos(\omega t)$$

$$\dot{x}(t) = \sqrt{\phi}[a + b]\, e^{\sqrt{\phi}(t-t1)} - \sqrt{\phi}[a - b]\, e^{-\sqrt{\phi}(t-t1)} - 2\omega c\cos(\omega t)$$

$$\dot{x}(t) = \sqrt{\phi}a\, e^{\sqrt{\phi}(t-t1)} + \sqrt{\phi}b\, e^{\sqrt{\phi}(t-t1)} - \sqrt{\phi}a\, e^{-\sqrt{\phi}(t-t1)} + \sqrt{\phi}b\, e^{-\sqrt{\phi}(t-t1)} - 2\omega c\cos(\omega t)$$

$$\dot{x}(t) = \sqrt{\phi}a\, e^{\sqrt{\phi}(t-t1)} - \sqrt{\phi}a\, e^{-\sqrt{\phi}(t-t1)} + \sqrt{\phi}b\, e^{\sqrt{\phi}(t-t1)} + \sqrt{\phi}b\, e^{-\sqrt{\phi}(t-t1)} - 2\omega c\cos(\omega t)$$

$$\boldsymbol{\dot{x}(t) = 2\sqrt{\phi}a\sinh\left(\sqrt{\phi}(t - t1)\right) + 2\sqrt{\phi}b\cosh(\sqrt{\phi}(t - t1)) - 2\omega c\cos(\omega t)}$$

When the pulse is completed, the equation of motion changes to

$$\ddot{x} - \phi x = \psi$$

Which has a solution of

$$x_{after}(t) = C3\ e^{\sqrt{\phi}t} + C4\ e^{-\sqrt{\phi}t} - \frac{\psi}{\phi}$$

$$\dot{x}_{after}(t) = \sqrt{\phi}C3\ e^{\sqrt{\phi}t} - \sqrt{\phi}C4\ e^{-\sqrt{\phi}t}$$

Here our boundary condition is more complex. The pulse starts motion of the grains when it first reaches the strength at t1. At time t2=pi, the pulse is completed and the solution should equal the solution after the pulse is finished.

So first, we need to calculate the position and velocity at t2=pi from our current solutions.

$$x(\pi) = 2a\cosh(\sqrt{\phi}(\pi - t1)) + 2b\sinh(\sqrt{\phi}(\pi - t1)) - 2c\sin(\omega\pi) - 2a - \frac{\psi}{\omega^2 + \phi}$$

$$\dot{x}(\pi) = \sqrt{\phi}a\sinh\left(\sqrt{\phi}(\pi - t1)\right) + \sqrt{\phi}\mathrm{b}\cosh(\sqrt{\phi}(\pi - t1)) - 2\omega c\cos(\omega\pi)$$

Then set the solution after the pulse equal to this:

$$x_{after}(\pi) = C3\ e^{\sqrt{\phi}\pi} + C4\ e^{-\sqrt{\phi}\pi} - \frac{\psi}{\phi}$$

$$= 2a\cosh(\sqrt{\phi}(\pi - t1)) + 2b\sinh(\sqrt{\phi}(\pi - t1)) - 2c\sin(\omega\pi) - 2a$$

$$- \frac{\psi}{\omega^2 + \phi}$$

$$C3\ e^{\sqrt{\phi}\pi} + C4\ e^{-\sqrt{\phi}\pi}$$

$$= 2a\cosh\left(\sqrt{\phi}(\pi - t1)\right) + 2b\sinh\left(\sqrt{\phi}(\pi - t1)\right) - 2c\sin(\omega\pi) - 2a$$

$$-\frac{\psi}{\omega^2 + \phi} + \frac{\psi}{\phi}$$

Let's focus on those last few constant terms:

$$-\frac{\psi}{(\omega^2 + \phi)} + \frac{\psi}{\phi}$$

$$-\frac{\psi\phi}{\phi(\omega^2 + \phi)} + \frac{\psi(\omega^2 + \phi)}{\phi(\omega^2 + \phi)}$$

$-\frac{\psi\phi}{\phi(\omega^2+\phi)} + \frac{\psi\omega^2}{\phi(\omega^2+\phi)} + \frac{\psi\phi}{\phi(\omega^2+\phi)} = +2a$ so the constants cancel out

At the end of the pulse, the sine term is also zero (at the half-period point):

$$C3\ e^{\sqrt{\phi}\pi} + C4\ e^{-\sqrt{\phi}\pi} = 2a\cosh\left(\sqrt{\phi}(\pi - t1)\right) + 2b\sinh\left(\sqrt{\phi}(\pi - t1)\right)$$

$$C3\ e^{\sqrt{\phi}\pi} + C4\ e^{-\sqrt{\phi}\pi} = a(e^{\sqrt{\phi}(\pi - t1)} + e^{-\sqrt{\phi}(\pi - t1)}) + b(e^{\sqrt{\phi}(\pi - t1)} - e^{-\sqrt{\phi}(\pi - t1)})$$

$$C3\ e^{\sqrt{\phi}\pi} + C4\ e^{-\sqrt{\phi}\pi} = a(e^{\sqrt{\phi}(\pi - t1)} + e^{-\sqrt{\phi}(\pi - t1)}) + b(e^{\sqrt{\phi}(\pi - t1)} - e^{-\sqrt{\phi}(\pi - t1)})$$

$$C3\ e^{\sqrt{\phi}\pi} + C4\ e^{-\sqrt{\phi}\pi}$$

$$= a(e^{\sqrt{\phi}\pi}e^{-\sqrt{\phi}t1} + e^{-\sqrt{\phi}\pi}e^{\sqrt{\phi}t1}) + b(e^{\sqrt{\phi}\pi}e^{-\sqrt{\phi}t1} - e^{-\sqrt{\phi}\pi}e^{\sqrt{\phi}t1})$$

$$C3\ e^{\sqrt{\phi}\pi} + C4\ e^{-\sqrt{\phi}\pi} = (\mathrm{a}e^{-\sqrt{\phi}t1} + \mathrm{b}e^{-\sqrt{\phi}t1})e^{\sqrt{\phi}\pi} + (\mathrm{a}e^{\sqrt{\phi}t1} - be^{\sqrt{\phi}t1})e^{-\sqrt{\phi}\pi}$$

$$C3\ e^{\sqrt{\phi}\pi} + C4\ e^{-\sqrt{\phi}\pi} = \left[(\mathrm{a} + \mathrm{b})e^{-\sqrt{\phi}t1}\right]e^{\sqrt{\phi}\pi} + \left[(\mathrm{a} - b)e^{\sqrt{\phi}t1}\right]e^{-\sqrt{\phi}\pi}$$

$$C3\ = \left[(\mathrm{a} + \mathrm{b})e^{-\sqrt{\phi}t1}\right]$$

$$C4\ = \left[(\mathrm{a} - b)e^{\sqrt{\phi}t1}\right]$$

$$x_{after}(t) = (a+b)\, e^{\sqrt{\phi}(t-t1)} + (a-b)\, e^{-\sqrt{\phi}(t-t1)} - \frac{\psi}{\phi}$$

$$x_{after}(t) = a\cosh(\sqrt{\phi}(t-t1)) + b\sinh(\sqrt{\phi}(t-t1)) - \frac{\psi}{\phi}$$

$$x_{after}(t) = \frac{\psi\omega^2}{2\phi(\omega^2+\phi)}\cosh(\sqrt{\phi}(t-t1)) + \frac{\omega\sqrt{A^2-(S_o-F_o)^2}}{2m\sqrt{\phi}(\omega^2+\phi)}\sinh(\sqrt{\phi}(t-t1)) - \frac{\psi}{\phi}$$

Moving to the velocity part:

$$\dot{x}_{after}(\pi) = \sqrt{\phi}C3\, e^{\sqrt{\phi}\pi} - \sqrt{\phi}C4\, e^{-\sqrt{\phi}\pi}$$

$$= \sqrt{\phi}\text{asin h}\left(\sqrt{\phi}(\pi-t1)\right) + \sqrt{\phi}\text{b}\cosh(\sqrt{\phi}(\pi-t1)) - 2\omega c\cos(\omega\pi)$$

$$\sqrt{\phi}C3\, e^{\sqrt{\phi}\pi} - \sqrt{\phi}C4\, e^{-\sqrt{\phi}\pi}$$

$$= \sqrt{\phi}\text{a}\,(e^{\sqrt{\phi}(\pi-t1)} - e^{-\sqrt{\phi}(\pi-t1)}) + \sqrt{\phi}\text{b}(e^{\sqrt{\phi}(\pi-t1)} + e^{-\sqrt{\phi}(\pi-t1)})$$

$$- 2\omega c\cos(\omega\pi)$$

$$C3\, e^{\sqrt{\phi}\pi} - C4\, e^{-\sqrt{\phi}\pi}$$

$$= \text{a}\,(e^{\sqrt{\phi}(\pi-t1)} - e^{-\sqrt{\phi}(\pi-t1)}) + \text{b}(e^{\sqrt{\phi}(\pi-t1)} + e^{-\sqrt{\phi}(\pi-t1)})$$

$$- 2\omega c\cos(\omega\pi)$$

The cosine term is near 1 at this time. This term will be a constant on the end, which we ignore.

$$C3\, e^{\sqrt{\phi}\pi} - C4\, e^{-\sqrt{\phi}\pi}$$

$$= \text{a}\,(e^{\sqrt{\phi}\pi}e^{-\sqrt{\phi}t1} - e^{-\sqrt{\phi}\pi}e^{\sqrt{\phi}t1}) + \text{b}(e^{\sqrt{\phi}\pi}e^{-\sqrt{\phi}t1} + e^{-\sqrt{\phi}\pi}e^{\sqrt{\phi}t1})$$

$$C3\ e^{\sqrt{\phi}\pi} - C4\ e^{-\sqrt{\phi}\pi} = (\mathrm{a} + \mathrm{b})e^{-\sqrt{\phi}t1}\ e^{\sqrt{\phi}\pi} - (a - \mathrm{b})e^{\sqrt{\phi}t1}\ e^{-\sqrt{\phi}\pi}$$

$$C3\ = \left[(\mathrm{a} + \mathrm{b})e^{-\sqrt{\phi}t1}\right]$$

$$C4\ = \left[(\mathrm{a} - b)e^{\sqrt{\phi}t1}\right]$$

The pulse dies when the velocity goes to zero. This will occur at t2:

$$\dot{x}_{after}(t2) = \sqrt{\phi}C3\ e^{\sqrt{\phi}t2} - \sqrt{\phi}C4\ e^{-\sqrt{\phi}t2} = 0$$

$$\left[(\mathrm{a} + \mathrm{b})e^{-\sqrt{\phi}t1}\right]\ e^{\sqrt{\phi}t2} - \left[(\mathrm{a} - b)e^{\sqrt{\phi}t1}\right]e^{-\sqrt{\phi}t2} = 0$$

$$[(\mathrm{a} + \mathrm{b})]\ e^{\sqrt{\phi}(t2-t1)} - [(\mathrm{a} - b)]e^{-\sqrt{\phi}(t2-t1)} = 0$$

$$a\ e^{\sqrt{\phi}(t2-t1)} + b\ e^{\sqrt{\phi}(t2-t1)} - \mathrm{a}e^{-\sqrt{\phi}(t2-t1)} + b\ e^{-\sqrt{\phi}(t2-t1)} = 0$$

$$a\ e^{\sqrt{\phi}(t2-t1)} - \mathrm{a}e^{-\sqrt{\phi}(t2-t1)} + b\ e^{\sqrt{\phi}(t2-t1)} + b\ e^{-\sqrt{\phi}(t2-t1)} = 0$$

$$a\ \sinh(\sqrt{\phi}(t2 - t1)) + b\ \cosh(\sqrt{\phi}(t2 - t1)) = 0$$

$$a\ \sinh(\sqrt{\phi}(t2 - t1)) + b\ \cosh(\sqrt{\phi}(t2 - t1)) = 0$$

$$a\ \tanh(\sqrt{\phi}(t2 - t1)) + b\ = 0$$

$$\tanh\left(\sqrt{\phi}(t2 - t1)\right)\ = -b/a$$

The hyperbolic tangent is never larger than 1, so

$$1 \geq -b/a$$

Now plug in our variables:

a=$\frac{\psi\omega^2}{2\phi(\omega^2+\phi)}$ b=$\frac{\omega\sqrt{A^2-(S_o-F_o)^2}}{2m\sqrt{\phi}(\omega^2+\phi)}$

$$-b/a \leq 1$$

$$b/a \geq 1$$

$$\frac{\omega\sqrt{A^2-(S_o-F_o)^2}}{2m\sqrt{\phi}(\omega^2+\phi)} * \frac{2\phi(\omega^2+\phi)}{\psi\omega^2} \geq 1$$

$$\frac{\sqrt{A^2-(S_o-F_o)^2}}{m} * \frac{\sqrt{\phi}}{\psi\omega} \geq 1$$

What we want is an amplitude above which triggering will be induced. So we solve for A.

$$\sqrt{A^2-(S_o-F_o)^2} \geq \frac{m\psi\omega}{\sqrt{\phi}}$$

Recall $\phi = \frac{S_o\beta}{m}$, $\psi = \frac{F_o-S_o}{m}$

$$\sqrt{A^2-(S_o-F_o)^2} \geq \frac{m\omega}{\sqrt{\frac{S_o\beta}{m}}}\frac{F_o-S_o}{m}$$

$$A^2-(S_o-F_o)^2 \geq \frac{\omega^2 m}{S_o\beta}(F_o-S_o)^2$$

$$A^2 \geq \frac{\omega^2 m}{S_o\beta}(F_o-S_o)^2+(S_o-F_o)^2$$

$$A \geq \sqrt{\frac{\omega^2 m}{S_o\beta}(F_o-S_o)^2+(S_o-F_o)^2}$$

$$A \geq (S_o-F_o)\sqrt{1+\frac{\omega^2 m}{S_o\beta}}$$

This is equation 5.18 and says that pulse amplitudes larger than this will prevent the slip velocity from going to zero and trigger a slip event. Note: A and F_o are normalized by *N*.